

Abstract

Horiba, Hironobu. 3-D Computed Tomography Using Diffraction Enhanced Imaging Modality. (Under the Direction of Professor Kuruvilla Verghese and Professor Dale E. Sayers.)

Atomic and nuclear radiation has been used to develop a large variety of medical imaging modalities for the benefit of humankind over the past fifty years. Diffraction Enhanced Imaging (DEI) is a new x-ray radiographic imaging modality using monochromatic x-rays to produce very clear digital radiographs of objects by virtually eliminating the detection of scattered photons and exploiting the refraction properties of the object. Being free of scatter DEI images have shown dramatically improved contrast over standard radiographs of the same object. The main objective of this work was to apply DEI to computed tomography (CT) and obtain three-dimensional tomographic images.

Two sets of experiments on Lucite phantoms were performed at the X15A beamline of National Synchrotron Light Source. The first experiment was performed to evaluate previous work related to this work. The second experiment was performed to obtain three-dimensional CT data. Three-dimensional images were successfully obtained and the apparent absorption and refraction images obtained from DEI showed information unavailable in conventional radiograph in computed tomography. There are two interesting findings in this research. One is that subtraction method for calculating refraction images which we suggested is found to be relatively free from contamination from the absorption component. The other is that the procedural orders of manipulation of taking logarithm and subtraction/addition seriously affect the quality of image. If one mixes this order, the result shows a hump-like artifact in both the absorption and refraction images.

For further improvements, an experimental method for preventing drifting of the rocking curve during the data acquisition and for fully separating the absorption and refraction components of the DEI data need further study. Also, it is recommended that an algorithm for automatically correcting for the off-axis rotation should be developed.

**3-D COMPUTED TOMOGRAPHY
USING DIFFRACTION ENHANCED IMAGING MODALITY**

By

Hironobu Horiba

A thesis submitted to the Graduate Faculty of
North Carolina State University
In partial fulfillment of the
Requirements for the Degree of
Master of Science

Department of Nuclear Engineering
North Carolina State University
Raleigh, North Carolina

2003

Approved by:

Dr. Kuruvilla Verghese, Co-Chair

Dr. Dale E. Sayers, Co-Chair

Dr. Sarah A. Rajala

Biography

Hironobu Horiba was born August 22, 1978 in Nagoya, Japan. He grew up primarily in Nagoya, Japan with his parents, Kenji and Hideko, as well as his brother and sister, Koji and Tomomi. He had his primary school education at Ohnogi in Nagoya and secondary education in Nanzan private school. Hironobu graduated in March of 1997. The following spring, he began college at Nagoya University as a nuclear engineering student. After obtaining his B.S. in Nuclear Engineering in March 2001, he began his graduate study in Nuclear Engineering at Nagoya University. Hironobu came to study at North Carolina State University in fall 2001 as an exchange student. He transferred to North Carolina State University in fall 2002.

Acknowledgements

I would like to show my appreciation to everybody who has helped me with my research. Dr. Zhong Zhong helped me with my experiments at NSLS and provided financial support for an experiment at BNL. He also allowed me to use his IDL libraries and gave me advice on IDL coding. I would like to thank Dr. Sarah Rajala for teaching me the course related to this research through an independent study. Without her help, I would not understand digital filtering nearly as well as I do today. I must also acknowledge the Nuclear Engineering department, for without this department's financial support I could not have performed this research at North Carolina State University. Finally, I would like to thank my advisors for giving me the chances necessary to do this research and for guiding me with my work.

Table of Contents

	Page
List of Figures.....	vi
1. Introduction.....	1
2. Background information	4
2.1. General Concepts and Synchrotron X-rays for Medical Imaging.....	4
2.2. Computed Tomography (CT) and CT Image Reconstruction	5
2.3. Diffraction Enhanced Imaging (DEI)	6
2.4. Diffraction Enhanced Computed Tomography (DECT)	10
3. Experimental Methods	12
3.1. The DEI system at the X15A Beamline.....	12
3.2. Data acquisition.....	14
4. Image Analysis and Reconstruction.....	17
4.1. General Procedures for Image Analysis and CT Reconstruction.....	17
4.2. Separation of the Absorption and Refraction Components.....	18
4.3. IDL Code for CT Reconstruction.....	19
5. Result and Discussion.....	23
5.1. Two-dimensional Slice Reconstruction Using Option 3.....	23
5.2. Two-dimensional Slice Reconstruction Using Option 1.....	28
5.3. Three-Dimensional Reconstruction of Phantom C.....	31
6. Conclusion and Recommendation.....	35
7. References.....	38
8. Appendices.....	40

9. Figures..... 59

List of Figures

	Page
Figure B.1 Image system.....	59
Figure E.1 Set up at the NSLS X15A beamline.....	60
Figure E.2 The silicon [333] rocking curves of the analyzer crystal at 40 keV.....	60
Figure E.3 The design of phantom A.....	61
Figure E.4 The design of phantom B.....	62
Figure E.5 The design of phantom C.....	62
Figure I.1.1 The block diagram of image processing procedure	63
Figure I.1.2 The example of Higher and lower side images	63
Figure I.1.3 Schematics of back projection	64
Figure I.1.4 Filters in frequency domain. Green line is Shepp Logan Filter.....	65
Figure I.1.5 Filters in spatial domain.....	66
Figure R.1.1 A slice of raw data of Lucite B at lower side of rocking curve.....	67
Figure R.1.2 Raw tomography data of Lucite B at lower side of rocking curve.....	67
Figure R.1.3 Sinogram of Lucite B at lower side of Rocking curve.....	68
Figure R.1.4 Sinogram with Shepp Logan Filter at lower side of Rocking curve.....	68
Figure R.1.5 Reconstructed image with Shepp Logan Filter at lower side of Rocking curve.....	69
Figure R.1.6 Reconstructed image without Filter at lower side of Rocking curve	70
Figure R.1.7 Line profiles of raw tomography data at y=169 at lower side of Rocking curve.....	71
Figure R.1.8 Line profiles of sinogram at y=169 at lower side of Rocking curve.....	71

Figure R.1.9 Line profiles of sinogram at $y=169$ with Shepp Logan filter at lower side of Rocking curve.....	72
Figure R.1.10 Line profiles of raw tomography data at $y=255$ at lower side of Rocking curve.....	73
Figure R.1.11 Line profiles of sinogram at $y=255$ at lower side of Rocking curve.....	74
Figure R.1.12 Line profiles of sinogram at $y=255$ with Shepp Logan filter.....	75
Figure R.1.13 Line profiles of reconstructed data at $y=255$ with Shepp Logan filter at lower side of Rocking curve.....	76
Figure R.1.14 Line profiles of reconstructed data at $y=255$ without filter at lower side of Rocking curve.....	77
Figure R.1.15 A slice of raw data obtained from the detector	78
Figure R.1.16 The normal image for image adjustment	78
Figure R.1.17 sinogram of Lucite B at higher side of rocking curve	78
Figure R.1.18 Sinogram of Lucite B at higher side of rocking curve with Shepp Logan filter	78
Figure R.1.19 Reconstructed image with Shepp Logan filter	79
Figure R.1.20 A line profile of raw tomography data at $y=94$	80
Figure R.1.21 A line profile of sinogram at $y=94$	81
Figure R.1.22 The apparent absorption image of the phantom B using option 3.....	82
Figure R.1.23 The refraction image of the Lucite B using option 3	83
Figure R.1.24 A line profile of absorption image of the phantom B using option 3	84
Figure R.1.25 A line profile of refraction image of the phantom B using option 3	85
Figure R.1.26 The apparent absorption image of the phantom B using option 1	86

Figure R.1.27 The refraction image of the Lucite B using option 1	87
Figure R.1.28 A line profile of absorption image of the phantom B using option 1	88
Figure R.1.29 A line profile of refraction image of the phantom B using option 1	89
Figure R.1.30 The comparison of line profiles Higher, Lower and simulation images of phantom B filled with water without any digital filters	90
Figure R.2.1 Absorption raw tomography data of phantom B filled with water	90
Figure R.2.2 Refraction raw tomography data of phantom B filled with water	91
Figure R.2.3 Absorption sinogram of phantom B filled with water	91
Figure R.2.4 Refraction sinogram of phantom B filled with water	91
Figure R.2.5 Filtered absorption sinogram of phantom B filled with water	92
Figure R.2.6 Filtered refraction sinogram of phantom B filled with water	92
Figure R.2.7 Reconstructed absorption image of phantom B filled with water	93
Figure R.2.8 Reconstructed refraction image of phantom B filled with water	94
Figure R.2.9 A line profile of reconstructed absorption image of phantom B filled with water	95
Figure R.2.10 A line profile of reconstructed refraction image of phantom B filled with water	96
Figure R.3.1 The refraction image $z=0$ x-y plane	97
Figure R.3.2 The apparent absorption image of $z=0$ slice in the radial(x-y) plane	98
Figure R.3.3 Transversel slices of the refraction image; where (a),(b) and (c) are images of from the channel 1,2, and 3 respectively	99

Figure R.3.4 Transversel slices of the apparent absorption image; where (a),(b) and (c) are images of from the channel 1,2, and 3 respectively. The lower number means higher y position.	100
Figure R.3.5 The line profile of the refraction image at $y=241, z=1$ showing the refraction signal from channel 2	100
Figure R.3.6 The line profile of the absorption image at $y=246, z=1$ showing the absorption signal from channel 2	101
Figure R.3.7 The three-dimensional voxel projection of refraction image.	102
Figure R.3.8 The three-dimensional voxel projection of absorption image.	103

1. Introduction

Atomic and nuclear radiation has been used to develop a large variety of medical imaging modalities for the benefit of humankind over the past fifty years. These modalities include digital radiography (DR), Computer Tomography (CT), Positron Emission Tomography (PET) and Single Photon Emission Computed Tomography (SPECT). Other imaging modalities such as Magnetic Resonance Imaging (MRI) and Ultrasound systems compliment the nuclear imaging modalities. Each imaging modality has its own advantages and disadvantages. MRI can obtain high resolution images, but it takes a long time to obtain images. On the other hand, CT can obtain images in short period. However, CT exposes patients to x-rays. Also, CT can measure only one physical parameter, the mass attenuation coefficient.

Research has shown that x-ray refraction can be another parameter for radiography and CT. Chapman, et al [1] have invented and reported on such a modality called Diffraction Enhanced Imaging (DEI). DEI is a new x-ray radiographic imaging modality using monochromatic x-rays to produce very clear digital radiographs of objects. DEI data are completely free of scatter and contain only the contributions from photons that are affected by absorption, extinction and refraction through very small angular deflections of the order of microradians (5.73×10^{-5} degree/microradian). Therefore, the images show dramatically improved contrast over standard radiographic imaging applied to the same object since those images will contain some contribution from scattered photons. The contrast is based not only on attenuation of x-rays but also the refraction properties of the sample. In fact, it is possible to essentially separate the absorption component of the image from the refraction component and construct images of both components. The refraction

component image will contain quite different types of information from that of the absorption image. DEI imaging shows promise of greatly improving image quality for medical applications such as mammography[1] and industrial applications for non-destructive testing. The differences of density between tumor lesions and normal breast tissue is small($\sim 2\%$) in mammography. So, it is difficult to detect small lesions in mammograms particularly in the presence of other heterogeneities in the breast. However, it should be possible to detect such lesions much better with DEI, because of the enhanced contrast. DEI consists of two physical parameters, mass attenuation coefficient and refractive index. Theoretically, the apparent absorption shows mass attenuation coefficient. However, this image is different from standard radiography in that this image is scatter free. The refraction image shows the gradient profile of refractive index which enhances the boundaries of regions with different refractive indices.

Dilmanian, et al [2] reported that DEI can be applied to CT imaging. However, the results obtained from Diffraction Enhanced Computer Tomography (DECT) shows that there is still considerable room for further sophistication for this modality. First, there are problems related to the use of hardware, mainly which, DECT requires adjustment of the angle of an analyzer crystal around its Bragg angle with microradian accuracy. Thermal and other effects can cause difficulty in maintaining the crystal angle with the degree of accuracy required. Secondly, there are problems related to the software, primarily understanding, the most effective filter for CT reconstruction of the DEI images by the back projection method. Thirdly, methods for determining the center of image for correcting for any off-axis rotation of the object are not fully developed and automated.

There are two main objectives for this research:

1. To clarify the problems of combining DEI and CT and solve such problems in order to enable DECT to be applied to medical diagnosis.
2. To demonstrate the potential for three-dimensional reconstruction of DEI images by stacking a large number of two-dimensional tomographic images.

Development of proper methods for reconstructing 3-D tomographic images obtained from DEI, should enable visualization of the wealth of information contained in DEI images with much greater clarity than currently possible with X-ray CT.

2. Background Information

The research reported here falls in the general area of imaging using synchrotron radiation and its potential for medical diagnosis. Therefore, we briefly wish to introduce the reader to some of the literature on general concepts of medical imaging first and then focus on a review of literature dealing with the specific subject of this thesis, namely, Computed Tomography (CT) and Diffraction Enhanced Imaging (DEI). Finally, one previous work on combining DEI and CT is introduced.

2.1 General Concepts and Synchrotron X-rays for Medical Imaging:

Synchrotron x-ray radiography has been applied, primarily at a research level, to various types of medical imaging problems and its potential use has been demonstrated in such areas as intravenous coronary angiography to look for blockages in coronary blood vessels, in-vitro monochromatic computed tomography and in-vitro imaging of tissue samples of human breast. The book, Medical Applications of Synchrotron Radiation [L.1] edited by Ando and Uyama is a collection of papers and a very good reference for medical applications of synchrotron radiation. There are three main sections in this book; these are Clinical Application in Practice or in Approach, Imaging, and Sources and Instruments. The Imaging section is particularly relevant to the topic of this thesis. In this section, papers related to phase contrast imaging techniques are introduced. They describe phase contrast imaging as becoming “a new x-ray eye in the 21st century” in the medical imaging area. DEI is, of course a phase contrast technique. Also, a paper related to DEI is introduced. All of the papers give fairly good information for understanding the basis of synchrotron radiation sciences related to medical imaging.

Secondary, general topics in medical imaging are briefly mentioned. An excellent reference for understanding the science of medical imaging is the textbook, The Essential Physics of Medical Imaging by Bushberg, Seibert, Leidholdt, Jr., and Boone [L.2]. The second edition of this book is now available. For understanding the basis of this research, section II, Diagnostic Radiology (except chapter 11 to 13) is well worth reading. This textbook has good discussions of fundamental concepts such as output intensity spectra of x-rays source, image quality degradation and related quantities such as Modulation Transfer Function (MTF) and Signal-to-Noise-Ratio (SNR).

2.2 Computed Tomography (CT) and CT Image Reconstruction:

The chapter on Computed Tomography in reference [L.2] provides an easily understandable non-mathematical introduction to the basic aspects of computer tomography and image reconstruction. However, further reading is essential for understanding the mathematical theory of tomographic reconstruction. The books, Principles of Computerized Tomographic Imaging [L.3] and Medical Imaging Systems [L.4] are good references for acquiring more information about the mathematics of tomographic reconstruction. Chapter 1 to 5 of [L.3] explains basics of signal processing, image processing and algorithms for reconstruction. Medical Imaging Systems [L.4] is mainly about radiography. Chapter 7, tomography, explains the mathematics of tomography. It is possible to get a good background about tomography from studying these two books.

Filtered back projection (FBP) Algorithm is used for reconstruction in this research, since the filtered back projection or convolution back projection algorithm is the most popular and most frequently used reconstruction method and is used in transmission CT.

The basic idea of back projection is to take the projection at each angle of rotation of the object and smear the intensities uniformly back into the object. With enough projection angles (typically 180 projections, each taken at every one degree of rotation), in principle, this should produce a cross sectional image of the object except for certain characteristic artifacts. The most significant artifact is the $1/r$ effect which makes the intensity of the image decrease from the center of the object to its sides. The $1/r$ artifact can be minimized using suitable digital filters. Important digital filters such as Shepp Logan which are commonly used in conjunction with tomographic reconstruction are explained in chapter 3 of the book, Foundation of Medical Imaging [L.5]. Other artifacts can result from the axis of rotation not coinciding with the axis of the object and from having insufficient number of projections in the reconstruction set.

2.3 Diffraction Enhanced Imaging (DEI):

The papers that were referred to in the first Chapter of this thesis (Introduction) are good for gaining an understanding of the concepts of DEI and DECT. The paper by Chapman, et al [1] is the best paper for understanding the physical principles and concepts of DEI.

At this point, it is important for the reader to understand the theoretical foundation for diffraction enhanced imaging. Figure B.1 shows a schematic diagram of the data acquisition system for DEI. The plane polarized white beam of synchrotron radiation from an electron storage ring is Bragg reflected by a pair of monochromator crystals of silicon. The Bragg angle of the monochromator determines the wavelength (or the energy) of the reflected photons and thus the wavelength is tunable. Because of the nature of the synchrotron radiation, the tuned beam is vertically collimated and parallel. A lead slit

selects about a 1mm high beam to pass horizontally through the object to be imaged. The beam transmitted through the object contains contributions from photons that were not absorbed in the object, but also those which were diffracted, scattered or refracted by the object. The latter three contributions typically will degrade the image quality in a conventional radiograph. For DEI, another Bragg crystal tuned to the wavelength of the incident beam is placed between the object and the detector. This crystal eliminates virtually all of the scattered (coherent and incoherent) and diffracted photons from the detected image. Because of the small but finite width of the rocking curve (reflectivity of the crystal as a function of the Bragg reflection angle) of the analyzer crystal, and the fact that refraction angles for x-ray photons are extremely small and fall within the width of the rocking curve, the detected photons will contain contribution from refraction in addition to x rays that are transmitted straight through the object. Refraction effects occur primarily at the boundaries of embedded structures which have different indices of refraction. Thus, if refraction contribution could be separated from the straight through contribution, the former could display the valuable information that will delineate the boundaries of even minute structures in the object.

The DEI methodology developed by Chapman, et al [1] does such separation of the detected signals into an ‘apparent absorption image’ (actually the image from direct transmission) and a ‘refraction image’ which correlates to the gradient of the refractive index along the path of the x rays through the object. To facilitate this, two images of the object are recorded on the digital recorder: one at an analyzer angle that is slightly greater than the peak angle of the rocking curve (hereafter called ‘the higher side image’) and one at a corresponding angle just less than the peak angle (hereafter called ‘the lower side

image'). According to Chapman, et al [1], the intensity diffracted by the analyzer set at a relative angle θ_i from the Bragg angle θ_B where $\theta_B + \theta_i$ is the angle between the incident beam and diffraction planes and is given by

$$I_i = I_R R(\theta_B \pm \theta_i)$$

where I_i is the intensity at relative angle θ_i from Bragg angle θ_B , I_R is defined as the portion of the incident beam which has only been affected by refraction and attenuation by absorption and extinction, and $R(\theta)$ is the analyzer reflectivity function at angle θ . $R(\theta)$ is the function that describes the rocking curve.

By Taylor expansion, the intensity of the images taken on the lower side (θ_L) and the higher side (θ_H) of the rocking curve are approximately

$$I_L = I_R \left(R(\theta_L) + \frac{dR(\theta_L)}{d\theta} \Delta\theta_z \right)$$

$$I_H = I_R \left(R(\theta_H) + \frac{dR(\theta_H)}{d\theta} \Delta\theta_z \right)$$

where I_L and I_H denotes beam intensity at the lower and higher sides of rocking curve. Note that $R(\theta)$ is written in a two-term Taylor expansion for the expressions above.

These two equations are solved for the intensity composed of apparent absorption, I_R , and for the refraction image angle, $\Delta\theta_z$, the angle through which x rays are refracted in the z-direction in traversing the object. These solutions are

$$I_R = \frac{I_L \left(\frac{dR(\theta_H)}{d\theta} \right) - I_H \left(\frac{dR(\theta_L)}{d\theta} \right)}{R(\theta_L) \left(\frac{dR(\theta_H)}{d\theta} \right) - R(\theta_H) \left(\frac{dR(\theta_L)}{d\theta} \right)}$$

$$\Delta\theta_z = \frac{I_H R(\theta_L) - I_L R(\theta_H)}{I_L \left(\frac{dR(\theta_H)}{d\theta} \right) - I_H \left(\frac{dR(\theta_L)}{d\theta} \right)}$$

Typically, the lower and higher side images are taken at the half-widths of the rocking curve which makes $R(\theta_L) = R(\theta_H) = 0.5$ with the peak reflectivity normalized to 1.0 and

because of the symmetry of the rocking curve around the peak, $\frac{dR(\theta_H)}{d\theta} = -\frac{dR(\theta_L)}{d\theta}$.

$$\text{Thus, } I_R = (I_L + I_H) \text{ and } \Delta\theta_z = \frac{0.5 [I_H - I_L]}{dR/d\theta [I_H + I_L]}$$

$\Delta\theta_z$ provides the distribution of angles of refraction in the z-direction and it is not the signal intensity due to refraction. The refraction signal intensity, I_r , is expressed by $I_R(dR/d\theta) \Delta\theta_z$ and hence proportional to $(I_L - I_H)$ assuming that $dR/d\theta$, the slope of the rocking curve, is a constant at the high side and low side angles at which the two images are measured. Note that simple addition and subtraction of the lower side and higher side images can yield I_R and $I_R\Delta\theta_z$ images. We refer to the I_R image as the “apparent absorption image” and I_r image as the “refraction image”. Chapman, et al have always used I_R and $\Delta\theta_z$ images in all of their work. Although $\Delta\theta_z$ contains refraction information, we will be using $I_R\Delta\theta_z$ for the refraction images in this work because of reasons discussed later in Chapter 4.

It is possible to perform a further survey of the DEI modality by reviewing the references quoted in the paper by Chapman, et al. Next, some of the important papers that showed that DEI can reveal considerably more details in biological specimens than conventional radiography are introduced. The papers, “Human breast cancer specimens: diffraction-enhanced imaging with histologic correlation - improved conspicuity of lesion detail compared with digital radiography” [L.6] and “Diffraction enhanced imaging

contrast mechanisms in breast cancer specimens” [L.7] show that DEI can reveal considerably more medically relevant details of breast tissue samples when compared with standard radiography.

In addition to the research at the U.S. synchrotron laboratories, investigation of phase contrast imaging are being carried out also at all of the major synchrotron light centers in Europe using synchrotron x-rays, for example, [L.8] and in Russia [L.9]. The Russian work originated independently of the studies elsewhere using standard x-ray tubes and therefore took prohibitively long times for data accumulation. Although these studies have produced interesting results, the method of separating the absorption effects from the refraction effects originated in the U.S. with the extensive work at the National Synchrotron Light Source (NSLS) at Brookhaven National Laboratory and this method is now used around the world.

2.4 Diffraction Enhanced Computed Tomography (DECT):

The first publication and so far, the only formal journal paper reporting on generating tomographic reconstructions from DEI images is the paper by Chapman, et al [2]. This work was carried out at NSLS using cylindrical acrylic phantoms with vertical and oblique holes filled with oil. In this paper, the following four conclusions are derived. Firstly, DECT projections are complete sets and thus can be reconstructed conventionally. Secondly, the separation of the refraction image from the other image components is complete for material with little small-angle scattering, such as oil and acrylic. Thirdly, the refraction image contrast is proportional to the gradient of the refractive index. Finally, there is a remarkable agreement between the linearity trends of the experimental findings

and the theoretical refractive index results. The absolute values agree within 20%. This thesis is a follow-up of the work reported in [2].

Preliminary work on a more exhaustive and versatile approach to DECT, known as Multiple Image Reconstruction (MIR) is progressing at the laboratories of Chapman and colleagues at the Illinois Institute of Technology [D. Chapman, Private communication, (2002)]. MIR CT is capable of providing images of four x-ray parameters instead of two (apparent absorption and refraction) in standard DECT. However, for clinical uses, MIR CT images may turn out to be too difficult to interpret and use at least until the radiology community gets attuned to viewing such data. Also, many images have to be acquired along the rocking curve in doing MIR CT and radiation dose accumulation could become a serious issue.

3. Experimental Methods

All of the data for this thesis were acquired at NSLS, Brookhaven National Laboratory (BNL), using the X15A beamline. The first experiment was in December 2002. The main objective of this experiment was to obtain two-dimensional DECT image of Lucite phantoms and examine the characteristics of DECT images and the choice of the most appropriate filter for backprojection. The second experiment was performed in the X15A beam in February 2003. The aim of his experiment was to obtain three-dimensional images of another Lucite phantom.

3.1 The DEI system at the X15A Beamline:

Figure E.1 shows schematically the experimental setup for DEI data acquisition at beamline X15A. The Bragg angle of the monochromator selects the wavelength of the x-rays to be used from the white synchrotron radiation beam. The monochromator and analyzer crystals are both positioned on a large granite block, 0.375 m wide, 0.3 m tall and 2.1 m long. The block is isolated from vibrations of the floor by rubber pads and vibration-insulating composite plates placed under the legs of the steel frame that supports the block [e1]. The monochromator is positioned inside a steel tank, sitting on the granite block and mechanically isolated from the beamline pipe by an air gap of 2cm. To reduce the rate of ozone production, the lower part of the x-ray spectrum is essentially eliminated using a 1 mm thick aluminum filter positioned downstream of the beamline's beryllium window. The sample scanning stage and shutter are placed on a platform positioned on a second steel frame which is directly supported by the floor. Thus, the stage and the shutter are isolated from the granite block.

. The X-ray energy was set to 40 keV and the maximum ring current was 178 mA. X15A is a standard NSLS bending –magnet beamline. The fan beam is 130 mm wide at the entrance to the experimental hutch, which is 16.3 m from the source. The useful height of the fan beam is about 2 mm where the intensity falls 20 % below the flat top. The aperture of the fan beam used for the experiment was 1.7 mm high and 128 mm wide. The x-ray storage ring operated at 2.80 GeV energy.

Thomlinson, et al developed the monochromator and analyzer system for DEI in the planar mode [e2], [e3], [e4]. It employed a two-crystal Bragg-Bragg monochromator using a silicon [1 1 1] reflection for both crystals. The monochromator was placed inside the stainless steel tank with helium at atmospheric pressure to prevent corrosion of its components by ozone. Each crystal was 10mm thick and 150mm wide, with strain relief cuts at 10mm from the ends of the crystal. Thus, the useful width of the crystal was 128 mm. The first crystal was 60 mm long along the beam's direction, and the second one was 90 mm. The larger length of the second crystal allowed a long range of energy change without requiring adjustment of the distance between the two crystals.

The monochromator is a box type design with a vertical offset of 1 cm between the two crystals [e4]. The first and second crystals are mounted on the bottom and top plates of the box respectively. Each crystal is mounted on kinematic mounts for adjusting the Bragg and analyzer angles, and is supported on the back side by three balls placed under the strain relief region, and secured on the front side by clamps. The box is mounted on a cradle, so that the middle of the first crystal surface is at the center of rotation. Because of its simplicity, the box type design is especially resistant to vibration. The instability of the beam's horizontal profile was 0.2 % /min, after the monochromator crystals reached

thermal equilibrium. This instability was assumed to be mainly caused by thermal drifts. The thermal equilibrium was reached in about 5min after the white beam was first put on the monochromator crystals. The analyzer crystal is of the same kind as the second crystal of the monochromator but used the [3 3 3] reflections of silicon. The Bragg angle of crystal is controlled by a tangent arm of 1m length, driven by a linear translator of resolution 0.1 μm . This arrangement provides an angular resolution of 0.1 μradian , which allows the analyzer to be tuned at a precision angle equal to $1/30^{\text{th}}$ of the full width at half-maximum of the rocking curve. The tangent arm is supported by the same granite block that supports the monochromator. Figure E2 shows the silicon [333] rocking curves of the analyzer crystal at 40 keV.

3.2 Data acquisition:

The digital detector was a Shad-o-box x-ray camera (Rad-icon Imaging Co. Ltd.) and the data acquisition system (DAS) was interfaced with a Dell computer. The x-rays detected by the digital detector in each pixel was transferred to the DAS and the data size was reduced with IDL computer software by cutting out redundant pixels which did not include any important information for data analysis. The raw data had a dimension of 2048×1024 pixels and it was reduced to the data size 2048×50 . Since the height of x-ray beam is 2.5 mm, there was no important information seen by the detector except over this range. The detector resolution was 50 μm . Therefore, 1mm is equal to 20 pixels.

Two Lucite phantoms were used for the first experiment. One was prepared at North Carolina State University (phantom A) and the other was prepared at BNL (phantom B). Both of them were Lucite cylinders. Phantom A has three paraxial cylindrical channels and

the Phantom B was a lucite rod placed obliquely inside a hollow Lucite cylinder. Figure E.3 shows the design of phantom A and Figure E.4 shows the design of the other phantom B. The diameters of the channels for the phantom A were the following: 1/8 inch, 1/4 inch and 1/4 inch. All of these channels were parallel to the phantom axis. The embedded Lucite rod inside phantom B is 12.74 mm in diameter and placed at a tilt angle 21.5 degrees with respect to the phantom axis. The reason that only phantom B was used in this thesis is that to produce diffraction enhancement, the channels must not be parallel to the z-direction. The channels in Phantom A are all vertical and hence no DEI could be done on it.

In the second experiment in February 2003, phantom C was prepared for obtaining three-dimensional reconstruction data. The design of phantom C is shown in Figure E.5. This phantom has three slanted channels with 1/8 inches diameter. These three channels have angle of 40, 55 and 75 degree measured from top surface of the phantom. The diameter of phantom is 2 inch.

Two sets of DEI scans were performed for each phantom by fixing the analyzer at a specific angle and rotating the sample stepwise through 360° at 1° increment. In one set, the phantom was filled with water and the other set, the phantom was empty. There are two reasons for preparing these sets. First, the phantom, which was empty, was used to check experimental set up accuracy, digital filter kernel size and other parameter adjustments. This phantom should produce images which can be reconstructed with two parameters, mass attenuation coefficient and diffraction enhanced signal. Second, the phantom, which was filled with water, was used to see pure diffraction enhancement signal. Due to the nearly equal values of mass attenuation coefficients of water and Lucite, the reconstructed images will not show apparent absorption differences in this case. Two sets of 180

projections were acquired from the same sample with the analyzer angle tuned to $-0.8 \mu\text{rad}$ and $0.8 \mu\text{rad}$ from the peak and the sample rotated through 180 one-degree steps. The FWHM of rocking curve at 40 keV x-ray energy is shown in Fig. E.2.

In each set of scans, three types of data were collected; these were background, air and actual image. The background image was for obtaining information about detector artifacts. Therefore, x-rays were not projected. The air image was for obtaining information about attenuation from air. Therefore, x-rays are projected to the detector without phantom in the beam. 20 sets of the background and air images were taken. Averaged values for these were used to analyze data as described in the next section. The actual image is for obtaining information about the phantoms. 360 images at 1 degree intervals were taken. While performing experiments, the electron ring current of the synchrotron was in the range between 215.3 and 184.8 mA.

All scans were controlled by a DEC Alpha computer with a program modified for the CT experiment. The program obtains from the user data such as the type of scan and the analyzer positions. Then, it performed the scan by controlling the stepping motors that rotated. The program also acquired readings from the ion chamber current throughout the scan to measure the dose.

4. Image Analysis and Reconstruction

In this chapter, the way we combined DEI and CT will be described. The manipulation of order of these two can affect image quality. Therefore, it should be performed in the appropriate order.

4.1. General Procedures for Image Analysis and CT Reconstruction:

As discussed earlier the experimental data for reconstruction of the two 2-D CT images of apparent absorption and refraction consist of the 180 projections taken at the lower and higher sides of the rocking curve and corrected for beam non-uniformities and air scattering. The block diagram in Fig. I.1 shows the general procedure for construction a CT image of the lower side or higher side data. The data sets are corrected for any non-axial rotation of the object. They are then filtered and back projected.

Fig. I.2 shows the higher side and lower side CT images of Phantom B. Note that absorption and refraction components are present in both images. The refraction effects are visible at the boundary of the Lucite rod embedded within the water. However, the black and white regions at the boundary of the rod are reversed in the two images. This is due to the reversal of the polarity of the refraction signals in the high and low side images as seen from the line scan profiles. The boundary between the water and the outer cylindrical container shows almost no refraction since that boundary is vertical and the there is no z-component of the refraction signal from that boundary.

4.2 Separation of the Absorption and Refraction Components:

The objective of DECT is to do tomographic reconstructions of the apparent absorption image and the refraction image. Since this separation of components is peculiar to DECT and unlike the case for conventional CT, question arises as to when this separation by the addition/subtraction procedure (discussed in Section 2.3) should be performed during the data analysis. There are three possible options (see Fig. I.1 also):

1. Separate the two components immediately after the raw projection data taken on the higher and lower sides have been corrected for air scattering, beam non-uniformity and non-axial center of rotation and then reconstruct the CT images of these components using filtered back projection procedure. The absorption image is to be reconstructed after a logarithmic transformation but the refraction image is to be back projected without the transformation.
2. Prepare the filtered sinograms of the higher and lower sides after logarithmic transformation of the corrected data as in the original program of Mark Rivers for conventional CT and then perform the addition/subtraction step. The added and subtracted data sets are then reconstructed by back projection.
3. Reconstruct the higher and lower side CT images after logarithmic transformation to produce images like the figures associated with section 4.1, then perform the addition/subtraction procedure on these two CT images on a pixel-by-pixel basis.

The three options described above are indicated by their corresponding numbers in Fig. I.1. Of these, Option 2 is a clearly invalid procedure since the addition/subtraction procedure is done on logarithmically transformed intensities of the signals and there is no theoretical basis for this. Considerable time was spent on implementing this procedure and

all of the absorption and refraction CT images from Phantoms B and C displayed a general halo artifact which led to the recognition of the invalidity and abandonment of this procedure for subsequent analyses. We will not discuss this procedure any further and we will focus on Options 1 and 3.

Results of options 1 and 3 will be presented in Section 5. Now we wish to proceed to the details of constructing sinograms and determining the center of rotation of the phantom from the projection data.

4.3 IDL Code for CT Reconstruction:

In this section, the mathematical basis about Computed Tomography is briefly mentioned and actual calculation using IDL is discussed. For CT reconstruction, backprojection algorithm was used. Fig. I.3 shows the schematics of simple back projection. X ray is projected to the object from a certain direction and an intensity profile is recorded at the other side. The l -axis denotes width of beam or detector pixel position. $G_{\theta}(l)$ denotes intensity profile or back projection data. This $G_{\theta}(l)$ can be mathematically expressed as equation below;

$$G_{\theta}(l) = \iint f(x,y)\delta(x \cos \theta + y \sin \theta - R) dx dy$$

This equation says that line profile $G_{\theta}(l)$ at position l can be obtained by summing up the mass attenuation effect by function f on the line R . Where R is any line parallel to the x ray direction. By taking this data from 0 to 180 degrees, sinogram can be obtained. Simple back projection has intrinsic artifact, called $1/r$ artifact. Therefore, removal of this artifact is important. To perform this, Shepp Logan filter was used for this research. The mathematical form of Shepp Logan Filter is shown below;

$$H_{SL}(\omega) = \begin{cases} |\omega| \sin\left(\frac{\omega}{4B}\right), & |\omega| < 2\pi B \\ 0 & , otherwise \end{cases}$$

$$h_{SL}(k) = \frac{-8B^2}{\pi(4k^2 - 1)}$$

H_{SL} denotes Frequency domain and h_{SL} donates mathematical form in the spatial domain.

Lam Rak filter has mathematical form of $H_{LR}=|\omega|$. Lam Rak is a high pass filter and causes oscillations in the frequency domain. This causes ringing artifacts in an image. Please note the difference between, H_{SL} and H_{LR} . Fig I.4 and Fig I.5 shows plots of these filters and of Gen Hamming window. The mitigation of oscillation in spatial domain with Shepp Logan and Gen Hamming windows can be seen.

Interactive Data Language (IDL) software was used to perform all of the image analysis, CT reconstructions and graphic visualization. IDL version 5.5 is a specialized fourth-generation language providing a framework that includes functions and tools for scientific computing and visualization. Transforms such as Riemann sum or Radon transform, as well as digital filtering are performed easily using IDL. Practical IDL programming [I.1] and IDL Programming Techniques [I.2] are good books to understand basic procedure to write IDL codes. The IDL code that was used to prepare sinograms and reconstruct tomographic images from the raw data files is attached in Appendix. The basic summaries of what the code does are given below. There are three types of raw data for each set of images; background, air and actual projections. Twenty sets of background and air images were averaged and used to produce the normalizing image for calculating the actual image that is free of beam non-uniformities and air scattering. Here, the normal image is defined as the background image subtracted from the air image. The background

image was subtracted from the detector image of the object, and then divided pixel by pixel by this normalizing image. These were stored as raw tomography images. The detector had a pixel size of 50 μm and there are 2048 pixels along each row. Since this data set was too large for data analysis, the image size is reduced by factor of four using the Expand command of IDL. The expand procedure shrinks or expands a two-dimensional array using bilinear interpolation. Therefore, there were a total of 512 pixels and each pixel corresponded to 200 μm . The raw tomography projections were transformed to sinogram using Sinogram.pro procedure, which was written by Mark Rivers [1.3]. This procedure mainly does the following. Please note that this procedure was skipped for generating the refraction image of option 1. First, it averages the air values on the left and right hand sides of the input. These averaged values were used to adjust horizontal intensity distribution of the beam. The beam intensity is adjusted linearly. Second, it takes the logarithm of input/air ratio; the output = $-\log(\text{input}/\text{air})$. Please note that air images correspond to initial intensity of the x rays and the input corresponds to actual images, which contains information about the object. Therefore, the output corresponds to line integral of the object. Finally, it calculates the center of gravity of the image and shifts the actual image center to match the center of image by using the center of gravity. The center of gravity of image at each row was calculated by the equation below.

$$COG(i) = \frac{\sum_{j=0}^m I(i, j) \times j}{\sum_{j=0}^m I(i, j)}, \quad i = 1, 2, \dots, n$$

Here, COG is center of gravity, $I(i, j)$ is the intensity of the pixel (i, j) , (m, n) is dimension of sinogram; n corresponds to rotation angle and m corresponds to image width. Therefore, the value of n should be 179 or 359 generally.

The numerator is the moment of each row of the image and the denominator is the sum of intensity of at each rotation angle, i . The COG of image draws a sine curve. By taking the average of the max and minimum value of COG, the actual rotation axis is estimated. To fit this sinusoidal curve, and estimate the center of gravity of image, the Curve-fit procedure is used. The shifting of raw images to match with the center was done using a routine called Poly_2D which can shift the image by fractional pixels. Since DEI is a phase contrast method and enhances the edge contrast, the Shepp Logan filter was chosen as the digital filter. The raw sinogram was filtered with Shepp Logan filter by calling `tomo_filter.pro` procedure. This procedure contains a choice of three major types of high pass filters; Ram-Lak, Shepp Logan and Gen Hamming window. From this filtered sinogram, tomography images were reconstructed by using Riemann sum routine, which is one of the back projection methods of IDL. What the Riemann sum routine does is to smear the 180 sets of back projections from each angle. Therefore, the manipulation of image with filters is important for removing halo artifacts or $1/r$ artifacts that arise from simple back projection. For example, the Shepp Logan filter enhances high frequency information while reducing low frequency information in Fourier domain. Please note that high frequency corresponding to sharp transition of image or edge and low frequency correspond to smoother transitions in image. This characteristic of the Shepp Logan filter is clear from Fig. R.1.13 and Fig. R.1.14 which are line profiles of an image with and without the filter. More details of filters are discussed in the Results and Discussion section follows.

5. Results and Discussion

In this Chapter, we start with the results of a 2-D reconstruction of DEI images and then proceed to present the results of the three-dimensional visualization of images that were generated from the 2-D slices. All of the results used projection data for Lucite phantoms B and C.

5.1 Two-dimensional Slice Reconstruction Using Option 3:

Figure R.1.1 to R.1.6 demonstrates how images are reconstructed from raw data. Figure R.1 shows a slice of the raw projection data which was detected by the digital detector. Several scratches can be seen everywhere in the projection. These detector artifacts were removed by dividing the raw image by the normal image. This raw projection data covered a height of 2.5 mm or 50 pixels. The middle row of pixels from this slice was chosen from the raw projection data slice for each angle of rotation of the object. Figure R.1.2 shows raw tomography data of Lucite B at lower side of rocking curve. All images discussed below were obtained at the lower side of rocking curve, unless mentioned otherwise. Here, each row of arrays stands for a projection angle (0 degree to 360 degree from top to bottom) or y-direction and column of arrays stands for intensity or x-direction. In this figure, the Lucite phantom shows strong refraction signals due to the sharp gradient of the refractive index between Lucite and air. The stripes in the y-direction are because of beam intensity fluctuations. Figure R.1.3 shows the sinogram of Lucite B, where the raw tomography data is modified to a sinogram by calling the sinogram routine. Therefore, the center of gravity of this image is matched to the middle of column array and “padding” can be seen the left hand side of image because of this adjustment. Here, padding means

adding some pixels on left side, whose values are same as the very left pixel in the original image and some pixels in the image were trimmed, since the image was shifted to right. Also, logarithm of raw tomography data is taken to change the value to correspond to mass attenuation coefficient. The vertical line which shows up on the left side of the phantom is a detector artifact. Figure R.1.4 shows the sinogram of Lucite B with Shepp Logan filter, which enhances the clarity of the edges. Kernel sizes of 10, 15, 30, and 40 were tried and the kernel size of 30 was chosen subjectively based on the observed image quality. A kernel size of 30 is recommended for conventional usage for back projection.

Figure R.1.5 shows reconstructed image with the Shepp Logan filter. The center of rotation is automatically calculated by the sinogram procedure, but the image shows that it is a little off from the true center of image. This is because of noise in images and asymmetry of the DEI signal. This asymmetry is discussed later. Figure R.1.6 shows reconstructed image without filters. This image shows that simple back projection causes blurring. Comparison of Figures R.1.5 and R.1.6 is interesting for understanding the effects of Shepp Logan filter. At the corners of Figure R.1.5, ray artifacts show up, but this can not be seen in Figure R.1.6. In the very center of Figure R.1.5, a small circle or dot can be seen because of a detector artifact. Also, a semicircular arch can be seen right below the Lucite image. These artifacts are not seen in Figure R.1.6. Thus, Shepp Logan filter does enhance edges in the image, but exaggerates noise at the same time. It should be noted that filter choice is usually a subjective factor and might cause loss of critically important information.

Figure R.1.7 to R.1.14 shows line profiles of raw tomography data, sinograms and reconstructed images to facilitate discussion of more details of the images or intensity

signals. Figure R.1.7 shows a line profile of raw tomography data at $y = 169$, where DEI signals disappear. Please note that y -direction is the angle of rotation for sinograms. DEI signal occurs due to differences of refractive index in the z -direction which is normal to the x - y plane or the reconstructed image. Figure R.1.8 shows a line profile of the sinogram at the same point. The center of column and the center of rotation are matched. Due to this manipulation, the image is shifted to the right and some pixels are padded in the left side of image. Theoretically, the embedded cylindrical Lucite rod should have an elliptical shape for its back projection. So this results matches with theoretical back projection profile fairly well. Figure R.1.9 shows a line profile of sinogram at the same point with Shepp Logan filter. Noise is exaggerated as previously discussed. The negative signals detected here is because of Shepp Logan filtering and not because of the refraction signal. Figure R.1.10 shows a line profile of raw tomography data at $y = 255$, where the refraction signal appears to be the strongest. Figure R.1.11 shows a line profile of the sinogram at the same point. The absolute values of intensity of the refraction signal at both of left and right side should be the same theoretically. However, asymmetries of signals are detected and cause the center of rotation to be slightly different from the center of image. Figure R.1.12 shows a line profile of sinogram at the same point with Shepp Logan filter. The strong signal due to refraction is observed. However, the asymmetry of DEI signals is exaggerated as well. Figure R.1.13 shows a line profile of the reconstructed image with Shepp Logan filter. This result shows the effectiveness of this filter for this phantom in that all signal intensities from Lucite are fairly flat. The maximum noise of back ground is about 0.3 and the maximum DEI signal is about 3.9. Therefore, SNR is 13 in this case. Figure R.1.14 shows a line profile of the reconstructed image without filter. The blurring in this image is

obvious when compared with Figure R.1.13. Since Figure R.1.14 is from simple back projection, $1/r$ artifact can be seen.

Figure R.1.15 to R.1.21 shows the results obtained at the high side of the rocking curve. Figure R.1.15 shows the raw tomography data and Figure R.1.16 shows the normalized data. As discussed previously, the raw tomography data was divided by the normal data and converted to a sinogram after taking logarithm. Figure R.1.17 and Figure R.1.18 show the sinograms of Lucite B at higher side of rocking curve without filtering and with filter, respectively. One of the most significant differences between images of the lower and higher side of rocking curve is that the dark and bright parts are flipped. This is because the rocking curve has different gradients at lower side and higher side. Therefore, the same amount of refraction at each side causes opposite DEI signals.

Figure R.1.19 shows the reconstructed image. The dark and bright parts in the image are different from the result for the lower side of rocking curve (Fig R.1.5). It should be noted that the mismatch of center in this image is small compared with that of Fig R.1.5. The line artifact which showed up at the edge of the embedded Lucite is smaller. Figure R.1.20 and R.1.21 show line profiles of raw tomography data and the sinogram respectively. The DEI signal is fairly symmetric. This causes the difference in the images of Fig R.1.19 and Fig R.1.5. The center of rotation is estimated by calculating intensity times position at each row or angle of sinogram. Since the total mass attenuation by the Lucite is the same, total intensity of each column of sinogram should be same. However, the center of gravity moves as a sinusoidal curve because of the non-axial rotation of the phantom. It should be noted that refraction signal cannot be used to estimate the center of image by this method, since physics of DEI and mass attenuation are totally different parameters. Since Lucite B

is symmetric, the sum of DEI signal at each row is equal to zero. Therefore, the center of rotation can be estimated by the same method as with conventional tomography data.

For the option 3 method of separating the apparent absorption image and the refraction images, we add and subtract the CT images of the higher and lower sides of the rocking curve respectively. We conjecture that the addition provides the absorption image as specified by the theory of DEI presented in Section 2.3 and that the subtraction will give the refraction image. The resulting absorption and refraction image for phantom B is shown in Fig.1.22 and Fig. 1.23. Line scans through absorption and refraction at the location indicated are shown in Fig.1.24 and Fig.1.25 respectively. Note that a line scan through this image at the location of $x=250$ shows that the absorption signals from Lucite attenuation is fairly flat. It is interesting to note that there is a small amount of refraction effect evident in the absorption image. This is most probably coming from a slight drift in the rocking curve during projection data acquisition which causes the higher and lower side image angles to be slightly asymmetric with respect to the center of the rocking curve. Since the angular settings are less than only one microradian above and below the center, even a very minute drift will cause asymmetry and negate the assumptions made in the theory regarding the reflectivity values of the analyzer crystal. Refraction image was obtained by subtracting the higher side CT image from the lower side CT image. The refraction image looks very clean and the line scan through the Lucite rod shows essentially only the refraction signals at the boundaries.

To compare option 3 with option 1, the apparent absorption and refraction images of phantom B using option 1 are shown in Fig. R.1.26 and Fig. R.1.27 respectively. Line profiles of these images are shown in Fig. R.1.28 and Fig.R.1.29 respectively. Details of

option 1 will be discussed in the following section. The biggest differences between option 1 and option 3 is that the refraction signal with option 3 reconstruction shows much larger values than that of option 1. This is because we are taking logarithm for refraction image with option 3. This fact shows that less absorption and highly refractive images are vulnerable to error with the option 3 method.

In summary, option 3 appears to give clean CT images of apparent absorption and refraction that show the expected results. But one might wonder why subtraction of the CT images from the high and low sides of the rocking curve which were generated assuming that the signals are comprised purely of exponential attenuation should produce such good results for the refraction image; after all, the refraction signals do not follow any exponential law. The reason appears to be the fact that on both sides of the rocking curve, for this particular phantom, the signals are comprised almost through the whole phantom by exponential attenuation and the refraction signals are localized just at the boundaries of the embedded rod inside the phantom.

To verify this hypothesis, we simulated the projection data for a Lucite cylinder of the same dimensions as the phantom, assuming just exponential attenuation (no refraction effects). Fig. R.1.30 shows the comparison of line scans through the same projection for the simulation and for the higher side data of the water-filled phantom B. The amplitude was scaled to match the two sets of data. Note that the overall shape of the real image agrees very closely with the simulation which ignored refraction effects. The minor differences observed are likely due to the differences in attenuation coefficient between water and Lucite and the refraction signals present in the real image. Also, the simulated image is free of quantum noise. This agreement demonstrates that the signals in the raw data are

dominated by exponential attenuation. This is also the case for the lower side data.

Therefore CT reconstruction of the higher and lower side data after logarithmic transformation is valid and the subtraction ought to provide a good image of the refraction signals.

5.2 Two-Dimensional Slice Reconstruction Using Option 1:

It is important to recognize that the validity of Option 3 is demonstrated above only for a simple phantom. In a complex biological sample with a very high degree of heterogeneities where refraction might be present throughout the specimen, Option 3 might not be a valid method. Option 1 appears to have a better theoretical basis than Option 3. In this method, the separation of the two components by the addition/subtraction procedure is performed on the projection data (raw tomography data) and not on the CT images of the higher and lower sides. The absorption component projections are reconstructed as in conventional CT after logarithmic transformation, but the refraction projections are reconstructed by filtered back projection without taking logarithms.

Figures R.2.1 through R.2.8 demonstrate how images are reconstructed from raw data with using option 1. First of all, raw tomography data of lower side and higher side are added/subtracted to obtain raw tomography absorption and refraction data. Absorption and refraction raw tomography data are shown in Fig. R.2.1 and Fig. R.2.2, respectively. The apparent absorption image looks like one cylindrical object. The inside rod Lucite can not be seen. Please note that digital addition is a mean filter and subtraction is a high pass filter. Therefore this mathematical procedure imposes filtering to raw tomography data or back projection line profiles at both side of rocking curve. In Fig. R.2.2, two undesirable

sine curves can be seen. This caused artifacts in refraction reconstructed image, which will be shown in the later of this section. These raw tomography data were converted to sinograms. Absorption and refraction sinograms are shown in Fig R.2.3 and Fig R.2.4, respectively. For the absorption image the conventional method which described in previous section was used. Therefore, the absorption image was converted to sinogram, or mass attenuation component. It is performed for the refraction image to shift the refraction image to match the center of the image and the rotation axis. Please note that logarithm was not taken for the refraction image. These absorption and refraction images were filtered using Shepp Logan filter and shown in Fig R.2.5 and R.2.6 respectively. In Fig R.2.5, two vertical lines can be seen. These are boundary of the digital detector. In Fig R.2.6, square shape can be seen on the left side of image. This part showed up because of padding due to shifting the image to the right. This padding caused a big circle-like artifact in the reconstructed image, which will be shown later. Figure R.2.7 and R.2.8 shows reconstructed apparent absorption and refraction images respectively. Figure R.2.9 and R.2.10 shows line profiles at $x=250$ of those. In Fig. R.2.7, refraction signal still can be seen, but the image has high quality. In Fig. R.2.8, you can see artifacts outside of the Lucite. However, outside Lucite is not our concern. Fig. R.2.9 shows slopes outside lucite. This is intrinsic artifact caused by Shepp Logan filter. The boundary between cylindrical Lucite and outside air is clear. Fig. R.2.10 shows four big peaks. Two of those outside are signal from boundary between air and Lucite. These signals are strongest due to the large refractive index difference between air and Lucite. The two inside signals are signals from the boundary between water and the inner Lucite rod. Other small signals are those from artifacts due to air bubbles inside the Lucite container.

A lot of time was spent using option 2 reconstruction method through this research. However, we found that it produced unexplainable artifacts. Option 3 produces good images. Through even further in-depth investigation about reconstruction methods, it was found that option one gave the best result.

5.3 Three-dimensional reconstruction of Phantom C:

In this section, three-dimensional reconstruction of apparent absorption images and refraction images from the transverse multiple slice data which were acquired on the second phantom (phantom C shown in Fig. E.5) with the oblique air holes will be presented. First, two-dimensional images or CT slices of absorption and refraction images obtained using option 1 are shown. These CT images were then stacked up to compose a three-dimensional image. The final result had the dimension of $(x,y,z)=(487,487,40)$. Here, the x and y values denote the transverse image size in pixels and the z -value denotes the height of image in pixels. Note that the height covers only 2 mm (40 pixels) because of some difficulties which were encountered with the stability of the synchrotron beam during the second set of experiments at NSLS. The image is shrunk by factor of four in the x - y plane using the expand command of IDL. Therefore one x - or y -pixel size corresponds to 200 μm . In the vertical direction, there is no reduction of pixel size and one pixel corresponds to 50 μm . Using this array, transverse slices of absorption image and refraction image were obtained. Line profiles of refraction image and absorption image were also obtained, where line profile means one row or column of image plane(x - y plane). Finally, three-dimensional voxel projection images of absorption and refraction images will be shown. The vertical slices showed that it is possible to get three-dimensional information of DEI

signal. However, the voxel projection images show some difficulties of DEI in producing three-dimensional voxel projection.

Figures R.3.1 and R.3.2 show the CT reconstruction of radial refraction and apparent absorption images, respectively. Let us label the holes in upper left, center and lower right as 1, 2, and 3, respectively. The slices for absorption images were taken at the same locations. Fig R.3.1 shows strong noise outside Lucite. This is caused by beam intensity being not automatically adjusted for the refraction image. However, the region outside of the Lucite is of no interest. Fig R.3.2 shows some contamination from refraction signals within the absorption image. As with the previous results on phantom B, there appear to be some contamination from refraction effects in the absorption image and vice versa in the refraction image. This was likely caused by slight drift of the angular position set on the rocking curve of the analyzer crystal while performing the data acquisition. Since the angular settings are at only $\pm 0.8 \mu\text{rad}$ from the peak of the rocking curve, even a very slight drift in the rocking curve during the data acquisition will negate the cleanliness of the refraction and absorption images.

Figure R.3.3 and Figure R.3.4 show the transverse slices of the refraction image and the apparent absorption image respectively. These images show that signals from the gradients in the refractive index shows up correctly in the vertical cross section plane. The reason for some gray scale difference in images is the differences in the refraction signal strength in the images. For example, if an image has strong positive refraction signal, the other pixels have relatively low values. Therefore, the image looked darker. (b.1) showed the elliptical shape in the signal. This was caused by the fact that the slice was taken at near the surface between the second channel and Lucite cylinder. (b.2) and (b.3) show the signal

asymmetry. This was caused by fact that the direction of hole and the transverse plane did not go in the same direction. In Fig R.3.4, clear surfaces between channels and Lucite can be seen, although these images include partial contamination from the refraction signal. From (b.1) to (b.4), the signals from refraction are seen. However, these images showed a clear edge, since apparent absorption image excludes scattering. Specifically, please note that the holes and backgrounds have similar gray scale levels in each image.

For further discussion of image qualities, the line profiles of refraction image and apparent absorption image are shown in Figure R.3.5 and Figure R.3.6 respectively. The x-axis and y-axis in these figures represent pixel number from the left side of an image and relative intensity. The signals from refractive index can be seen in Fig. R.3.5. The reason why the edge of Lucite can be seen clearly is that the noise level dramatically increased outside the Lucite. Please note that this profile is free from the absorption component. However, Fig R.3.6 shows contamination from refraction signals and slight slope outside Lucite. However, clear edge between Lucite and the outside air can be seen and channel 2 showed up clearly. This channel has almost identical value with outside air as expected.

Using the 2-D slices, three-dimensional voxel projection of refraction and apparent absorption images were attempted. The results are shown in Figure R.3.7 and Figure R.3.8 respectively. Voxel projection assigns opacity according to intensity of each voxel. Figure R.3.7 (a) shows the surfaces of channels since these signals include information on the gradient of the refractive index. The non-uniformities within the holes are likely caused by the roughness developed during machining of the holes. The reason that dark regions exist inside the channels is that signals from refractive index become zero at a certain angle, at

which the difference of refractive index disappear in z-direction. Signals from refraction reverse at this point from positive to negative or vice versa.

Fig R.3.8 shows the 3-D apparent absorption image. To obtain this image, the procedures described below were performed. Since 3-D imaging here is just a procedure for visualization, empirical adjustments as below could be made in order to make the images visually acceptable. First, values outside of the Lucite were changed to zero and one was added to this region. The median of Lucite intensity was calculated and this value was divided by two. This value was multiplied by the values outside the Lucite. According to these processes, outside Lucite has a unique constant equal to the median of Lucite value divided by two. The high opacity values were assigned to channels. Lucite was assigned small opacity. The opacity for Lucite was set to one tenth of those of channels. The result shown has good quality, but mitigation of noise in image can produce clearer 3-D images.

6. Conclusions and Recommendations

There were two main objectives of this research. One was to examine applicability of DEI to produce three-dimensional CT images using phantoms and to investigate the applicability of this technique to more complicated samples such as biological specimens. This included developing an IDL code for filtered back projection and filter choices for this algorithm. The other was three-dimensional voxel projection of three-dimensional array data.

The two-dimensional cross sectional images of CT slices showed physically meaningful images and intensity profiles. Three-dimensional voxel projection of a Lucite phantom with holes slanted at different angles was also successful. The results showed that DEI modality and CT images of apparent absorption and of refraction would reveal information which standard CT images can not produce.

Two major problems which encountered thorough this research is briefly mentioned. One of the problems which caused difficulty of three-dimensional voxel projection was that intensity of the signal from refraction depends both on x-ray projection angles and the refractive index. This meant that refraction signal would display two objects of the same refractive index but different projection angle with two different opacities. Thus refraction projections are not intrinsically suitable for 3-D voxel projection if one of the aims is to have refraction images that will be representative of the structural pattern in the object. Secondly, the two sets of diffraction enhanced data taken on either side of the rocking curve of the analyzer crystal were separated into two images one presumably containing only the effect of x-ray absorption within the object and the other containing only the refraction component. However, the results showed that the perfect separation of these two

components were difficult to achieve practically due to the problem of drift of the rocking curve of the analyzer crystal. Because of the very steep slope of the rocking curve, even very small drift of the order of one or two microradians could cause significant asymmetry in the angular positions at which the two data sets were taken. The addition/subtraction algorithm that was used to separate the two data sets into images of pure absorption and pure refraction components would instead provide images each image showing some contamination from the other component. This was particularly true for the absorption image. The refraction images were relatively free from contamination from apparent absorption signal.

The first problem can be solved by simultaneously viewing the information provided by both the absorption and refraction images. The absorption image is much like a conventional CT image in that it represents the physical structure of x-ray absorption in the object. The refraction image clearly delineates the boundaries of the structures within the object and can show also very small heterogeneities if they have sharp gradients in refractive indices but similar absorption characteristics as the bulk of the object. Therefore, simultaneously viewing a combination of absorption, refraction, and peak radiography images is very important for interpreting DEI tomographic data and using all of the information contained in them. Also, the refraction image can be useful for edge detection or segmentation of images because of its intrinsically strong signals. The second problem also has a solution. By taking images at multiple points on the rocking curve and not just three images, namely at lower, higher and peak angular settings, it is possible to estimate more accurately the Darwin width of rocking curve and possibly make corrections for the drift of the rocking curve. For further work, some other filters can be tried instead of Shepp

Logan filter. For three dimensional reconstructions, noise introduction should be minimized. Also, for taking images of more complicated samples than the phantoms, a more sophisticated method for estimating center of images needs to be developed.

There are two interesting findings in this research. One is that subtraction method for calculating refraction images which we suggested appear to be much more free from contamination from absorption component as compared to the current practice of mapping the image of the refraction angles. The other is that the procedural order of image processing, namely, the order in which logarithmic transformation and subtraction/addition will seriously affect the quality of image. In other words, the raw data can not be treated the same way as in conventional tomography. If one makes mistake in this order, the result will show a humplike artifact in both absorption and refraction images.

7. References

- [1] D Chapman et al, Diffraction enhanced x-ray imaging, *Phys. Med. Biol.* **42** (1997) 2015-2025., UK
- [2] F D Dilmanian et al, Computed tomography of x-ray index of refraction using the diffraction enhanced imaging method, *Phys. Med. Biol.* **45** (2000) 933-946., UK
- [L.1] M. Ando and C. Uyama (Eds.), Medical Applications of Synchrotron Radiation, Springer-Verlag (1998), Tokyo
- [L.2] Jerrold T. Bushberg et al, The Essential Physics of Medical Imaging, Lippincott Williams & Wilkins (1994), Baltimore Maryland USA.
- [L.3] Avinash C. Kak and Malcolm Slaney, Principles of Computerized Tomographic Imaging, IEEE Press (1987), New York.
- [L.4] Macovski, A. Medical Imaging Systems, Prentice-Hall (1983), Englewood Cliffs, NJ.
- [L.5] Z.H. Cho, Foundations of Medical Imaging, John Wiley & Sons (1993), USA
- [L.6] Pisano ED, Johnston RE, Chapman D, Geradts J, Iacocca MV, Livasy CA, Washburn DB, Sayers DE, Zhong, Z, Kiss MZ, Thomlinson WC. 2000. Human breast cancer specimens: diffraction-enhanced imaging with histologic correlation - improved conspicuity of lesion detail compared with digital radiography. *Radiology* **214**(3): 895-901
- [L.7] Hasnah MO, Zhong Z, Oltulu O, Pisano E, Johnston RE, Sayers D, Thomlinson W, Chapman D. 2002. Diffraction enhanced imaging contrast mechanisms in breast cancer specimens, *Med. Phys.* **29** (10): 2216-2221.
- [L.8] J. Baruchel, A. Lodini, S. Romanzetti, F. Rustichelli and A. Scrivani 2001, "Phase contrast imaging of thin biomaterials", *Biomaterials* **22** 1515-1520

- [L.9] V.N. Ingal, E.A. Beliaevskaya, A.P. Brinskaya and R.D. Merkurieva, “Phase Mammography – a new technique for breast investigation”, *Physics in Medicine and Biology*, Vol. 43, pp. 2555-2567 (1998)
- [e1] Mangra D, Sharma S and Jendrzeczyk J, Passive vibration damping of the APS machine components, *Rev. Sci. Instrum.* **67** 3374 (1996).
- [e2] Chapman D, Pisano E, Thomlinson W, Zhong Z, Johnston R E, Washburn D and Sayers D, Medical and biological applications of diffraction enhanced imaging Breast Disease, *Rev. Mod. Phys.* **10** 197-207 (1998).
- [e3] Thomlinson W, Chapman D, Zhong Z, Johnston R and Sayers D, Diffraction enhanced x-ray imaging *Medical Applications of Synchrotron Radiation* ed M Ando and C Uyama (Tokyo: Springer) pp 72-7 (1998).
- [e4] Zhong Z, Thomlinson W, Chapman D and Sayers D, Implementation of diffraction enhanced imaging at NSLS and APS, *Nucl. Instrum. Methods Phys. Res.* (1999)
- [I.1] Liam E. Gumley, *Practical IDL Programming*, Morgan Kaufmann (2001), CA.
- [I.2] David W. Fanning, *IDL Programming Techniques* 2nd edition, Fanning Software Consulting (2000), CO.
- [I.3] Rivers Mark, [Tutorial Introduction to X-ray Computed Microtomography Data Processing](http://www-fp.mcs.anl.gov/xray-cmt/), <http://www-fp.mcs.anl.gov/xray-cmt/> , ANL(1998)

8. Appendices

8.1 IDL Codes

IDL codes, which are useful to refer to, are selected and shown below. For further references, please contact with me.

```
*****
*****
Pro angle1_t1 is the main code used to analyze 2-D data. This code includes
subroutines(other files) such as sinogram and tomofilter with reconstruction method 1
*****
*****
PRO angle_t1
myfileL='angle1'
myfileR='angle2'
key='h:\hiro\'
imagedir=key+'obtained_img\'

; caution!! to variables
bin_size=4
acc_values=50/bin_size
air_values=150/bin_size
filter_size=30
filter_d=1

.*****
;
;Please run the other code called angle1 and angle 2 to obtain sinogram
;from raw tomography data; the way obtained sinogram is shown in Pro b1_read_data
.*****
;
sino_L=read_ary(imagedir+myfileL+'_sino')
sino_R=read_ary(imagedir+myfileR+'_sino')

raw_sinL=rotate(sino_L,1)
raw_sinR=rotate(sino_R,1)

raw_sinL=raw_sinL[*;0:179]
raw_sinR=raw_sinR[*;0:179]
;stop
n_ang=n_elements(raw_sinL[0,*])
.*****
;normalization of each side image
.*****
;
For i=0,n_ang-1 do begin
```

```

clip_l=raw_sinl[452:511,i]
clip_r=raw_sinr[452:511,i]
n_cl=n_elements(clip_l)
n_cr=n_elements(clip_r)

norm_l=total(clip_l)/n_cl
norm_r=total(clip_r)/n_cr
raw_sinl[* ,i]=raw_sinl[* ,i]/norm_l
raw_sinr[* ,i]=raw_sinr[* ,i]/norm_r

;***** plot of lower and higher side profiles *****
if ((i mod 10) eq 0) then begin
  loadcolors
  window, /free
  plot, raw_sinl[* ,i], subtitle='i='+string(i)
  oplot, raw_sinr[* ,i], color=2
  loadct, 0
endif
;*****
ENDFOR

;min_l=min(raw_sinl)
;min_r=min(raw_sinr)
;max_l=max(raw_sinl)
;max_r=max(raw_sinr)
;raw_sinr= raw_sinr < max_l
;raw_sinr= raw_sinr > min_l
stop

;*****
;Produce refraction and absorption images
;prepare refraction and apparent absorption image
;*****

sino_abs =raw_sinR+raw_sinL
sino_ref =raw_sinR-raw_sinL/sino_abs
;sino_ref=raw_sinR-raw_sinL

stop
;image manipulation for each side image

nanglesL = n_elements(sino_abs[0,*])

```

```

nanglesR = n_elements(sino_ref[0,*])

;check dimensions
if (nanglesL ne nanglesR) then begin
  print, 'dimensions don"t match'
  stop
endif else begin
  nangles = n_elements(raw_sinR[0,*])
  angles=fltarr(nangles) ;declare of dimension
endelse
for i=0,nangles-1 do begin ;0-180 degree for radon trans
  angles(i)=float(i) * !PI/nangles ;change to 2*!PI in case 360 deg
endfor

stop

sino_abs=sinogram(sino_abs, angles,cog=cog,acc_values=acc_values,
air_values=air_values, $
  /debug)

sino_ref=sinogram3(sino_ref, angles,cog=cog,acc_values=acc_values,
air_values=air_values, $
  center=-60.50,/debug)

tvsize, sino_abs,title='corr_sinL'
tvsize, sino_ref,title='corr_sinR'

stop

sino_abs=tomo_filter(sino_abs, filter_size, filter_d, /Shepp_Logan)
filter_d=1.
sino_ref=tomo_filter(sino_ref, filter_size, filter_d, /Shepp_Logan)

;stop

;CAN NOT SUBTRACT/ADD IMAGES HERE!?!
;prepare refraction and apparent absorption image
;sino_ref =raw_sinR-raw_sinL
;sino_abs =raw_sinR+raw_sinL

tvsize, sino_ref
tvsize, sino_abs

```

```

;stop
redo1 =1

IF redo1 THEN BEGIN
;re-construction

;anglesA = n_elements(sino_abs[0,*])

;anglesR = n_elements(sino_ref[0,*])

;check dimensions
; if (anglesA ne anglesR) then begin
;   print, 'dimensions don"t match'
;   stop
; endif else begin
;   nangles = n_elements(sino_ref[0,*])
;   angles=fltarr(nangles) ;declare of dimension
;   endwhile
;stop
;for i=0,angles-1 do begin ;0-180 degree for radon trans
;   angles(i)=float(i) * !PI/nangles ;change to 2*!PI in case 360 deg
;endfor

nx_L = n_elements(sino_abs[*],0)
nx_R = n_elements(sino_ref[*],0)

b_L = fltarr (nx_L,nx_L) ;initialreconstructedimage
b_R = fltarr (nx_R,nx_R)

;stop
wd

for i=0,angles-1 do begin ;180 degree image
  if (i eq 0) then begin
    ; tvsize, b
  endif
  riemann, sino_abs, b_L, i * !PI/nangles, row=i, /backproject, $
  center=183.0,cubic=-0.5 ;in case 360 put "2.*" coz 0-2*!PI

;print, 'reconstructing', i, ' of, nangles
;tv, bytscl(b_L)

```

```

endfor

for i=0,nangles-1 do begin ;180 degree image center=183
    riemann, sino_ref, b_R, i * !PI/nangles, row=i, /backproject, $
        cubic=-0.5
    ;print, 'reconstructing', i, ' of', nangles
    tv, bytscl(b_R)
    ;stop
endfor

endif
tvsize,b_L,title='absorption image reconstructed'
tvsize,b_R,title='Refraction image reconstructed'

;print_image, b_L, file=imagedir+myfileL+'test'
;print_image, b_R, file=imagedir+myfileR+'test'

stop
END

*****
*****
sinogram.pro and tomofilter.pro is obtained by ANL webpage
*****
*****

function sinogram, input, angles, $
    acc_values = acc_values, $
    air_values = air_values, $
    backlash = backlash, $
    center = center, $
    tweak_center = tweak_center, $
    cog = cog, $
    debug = debug

;+
; NAME:
;     SINOGRAM.PRO
; PURPOSE:
;     To convert raw tomography data into a sinogram.
; CATEGORY:
; CALLING SEQUENCE:
;     result = SINOGRAM(INPUT, ANGLES, [keywords])
; INPUTS:
;     INPUT
;     An array of raw tomography data. INPUT(I, J) is the intensity at

```

```

; position I for view angle J. Each row is assumed to contain at least
; one air value at each end for normalization.
; ANGLES
; An array of the angles of each row of the input. Units are radians.
; OPTIONAL INPUT PARAMETERS:
; NONE
; KEYWORD PARAMETERS:
; ACC_VALUES=acc_values
; The number of values to be discarded at the beginning and end of each
; row. These values are typically discarded because the stage was in its
; acceleration/deceleration phase or because there are simply an
; unnecessarily large number of air values at the ends of each row.
; This keyword is only useful for first-generation CT data.
; The default value is 0.
; AIR_VALUES=air_values
; The number of air values to be averaged together at the beginning and
; end of each row, after discarding the ACC_VALUES. This averaging is
; done to decrease the statistical uncertainty in the air values.
; The default value is 10.
; COG=cog
; This keyword is used to return the measured and fitted
; center-of-gravity data for the sinogram. The center-of-gravity data are
; very useful for diagnosing problems such as backlash, beam hardening,
; detector saturation, etc. COG is dimensioned (n_angles, 2), where
; n_angles is the number of angles in the input array. COG(*,0) is the
; measured center-of-gravity data. COG(*,1) is the fitted data. The
; following command can then be given after the SINOGRAM command
; IDL> PLOT, COG(*,0)
; IDL> OPLOT, COG(*,1)
; to see if the sinogram data are reasonable.
; /CENTER
; Used to specify that the output is to be shifted left or right so that
; the fitted rotation axis of the sinogram is centered exactly on the
; center column of the output array. This operation is used to correct
; for the fact that the rotation axis may not have been perfectly
; centered when the data were collected.
; The default is not to center the output.
;
; TWEAK_CENTER=tweak_center
; Used to specify a "tweak" to the center. This tweak value is a floating
; point value (in pixels) which is added to the center which is determined automatically
; by the /CENTER keyword.
;
; /BACKLASH
; Used to specify that even rows of the image are to be shifted left or

```

```

; right so that the fitted rotation axis of the even rows is the same
; as that for the odd rows. This is used to correct for backlash on
; images done with first generation CT scans, when the scanning is
; done bidirectionally.
; The default is not to correct backlash.
; /DEBUG
; Used to turn on debugging output. The default is not to print debugging output.
;
; RETURN:
; The output array containing the corrected sinogram. It is always of
; type FLOAT.
;
; PROCEDURE:
; This routine creates a sinogram from raw tomography data. It does the
; following:
; - Converts to an odd number of columns (if necessary) by discarding the
; last column
; - Discards unwanted or unneeded pixels from the left and right edges of the
; image. These could be values collected during motor acceleration or
; extra air values which will simply slow down the reconstruction.
; "ACC_VALUES" pixels are discarded from both the left and right edges
; of the array.
; - Averages the air values for "air_values" pixels on the left and right
; hand sides of the input.
; - Logarithmation. output = -log(input/air). The air values are
; interpolated between the averaged values for the left and right hand
; edges of the image for each row.
; - Backlash correction (optional) If /BACKLASH is specified then motor
; backlash is corrected for. This is done by fitting the
; center-of-gravity separately for the even and odd rows of the image
; and then shifting the even rows so the the rotation axes are the same.
; The measured center-of-gravity is fitted to a sinusoidal curve
; of the form  $Y = A(0) + A(1)*\text{SIN}(X + A(2))$ .
; A(0) is the rotation axis
; A(1) is the amplitude
; A(2) is the phase
; The fitting is done using routine CURVE_FIT in the User Library.
; The shifting is done using routine POLY_2D which can shift by
; fractional pixels.
; - Centering of the rotation axis (optional). If /CENTER is specified then
; the image is shifted so that the rotation axis obtained by fitting the
; center-of-gravity data for all rows in the image coincides exactly
; with the center column. If TWEAK_CENTER is specified then this value is
; added to the fitted center before the shifting is done.
; The shifting is done using routine POLY_2D which can shift by

```

```

; fractional pixels.
; MODIFICATION HISTORY:
; Created 21-OCT-1991 by Mark Rivers.
; MLR 25-NOV-1994:
; Removed BSIF_COMMON
; Made TOMO_HEADER a structure passed to the routine
; This structure must contain the fields .ANGLE, .WIDTH, .STEP_SIZE
; MLR 13-MAY-1998
; Converted from a procedure to a function, added ANGLES parameter, removed
; TOMO_HEADER parameter. Added TWEAK_CENTER and DEBUG keywords.
;-

```

```

if n_elements(air_values) eq 0 then $
    air_values = 10
if n_elements(acc_values) eq 0 then $
    acc_values = 0
if n_elements(tweak_center) eq 0 then $
    tweak_center = 0.

```

```

ncols = n_elements(input(*,0))
nrows = n_elements(input(0,*))
; If there are an even number of columns in the image throw out the last one
if (ncols mod 2) eq 0 then ncols=ncols-1

```

```

; Throw out the acceleration values, convert data to floating point
output = float(input(acc_values:ncols-acc_values-1, *))
ncols = n_elements(output(*,0))

```

```

;stop

```

```

cog = fltarr(nrows) ; Center-of-gravity array
linear = findgen(ncols) / (ncols-1)
lin2 = findgen(ncols) + 1.
weight = fltarr(nrows) + 1.
for i=0, nrows-1 do begin
    air_left = total(output(0:air_values-1,i)) / air_values
    air_right = total(output(ncols-air_values:ncols-1,i)) / air_values
    air = air_left + linear*(air_right-air_left)
    output(0,i) = -alog(output(*,i)/air > 1.e-5)
    cog(i) = total(output(*,i) * lin2) / total(output(*,i))
endfor
odds = where((indgen(nrows) mod 2) ne 0)
evens = where((indgen(nrows) mod 2) eq 0)
x = angles

```

```

a = [(ncols-1)/2., $ ; Initial estimate of rotation axis
      (max(cog) - min(cog))/2., $ ; Initial estimate of amplitude
      0.] ; Initial estimate of phase
cog_fit = curvefit(x(odds), cog(odds), weight(odds), a, sigmaa, $
                  function_name='sine_wave')
cog_odd = a(0) - 1.
if (keyword_set(debug)) then print, format=(a, f8.2, a, f8.2)', $
'Fitted center of gravity for odd rows = ', cog_odd, ' +-', sigmaa(0)
cog_fit = curvefit(x(evens), cog(evens), weight(evens), a, sigmaa, $
                  function_name='sine_wave')
cog_even = a(0) - 1.
if (keyword_set(debug)) then print, format=(a, f8.2, a, f8.2)', $
'Fitted center of gravity for even rows = ', cog_even, ' +-', sigmaa(0)
if (n_elements(backslash) ne 0) then begin
  back = cog_even - cog_odd
  if (keyword_set(debug)) then print, format=(a, f8.2)', $
  'Backlash (even rows shifted right relative to odd rows) = ', back
  P = [[back, 0.],[1., 0.]]
  Q = [[0., 1.],[0., 0.]]
  temp = poly_2d(output(*, evens), P, Q, 1)
  for i=0, nrows-1, 2 do begin
    output(0, i) = temp(*, i/2)
    cog(i) = total(output(*,i) * lin2) / total(output(*,i))
  endfor
endif
cog_fit = curvefit(x, cog, weight, a, sigmaa, $
                  function_name='sine_wave')
cog_mean = a(0) - 1.
error_before = cog_mean - (ncols-1)/2.
if (keyword_set(debug)) then print, format=(a, f8.2, a, f8.2)', $
'Fitted center of gravity = ', cog_mean, ' +-', sigmaa(0)
if (keyword_set(debug)) then print, format=(a, f8.2)', $
'Error before correction (offset from center of image) = ', error_before
if (n_elements(center) ne 0) then begin
  P = [[error_before+tweak_center, 0.],[1., 0.]]
  Q = [[0., 1.],[0., 0.]]
  output = poly_2d(output, P, Q, 1)
  for i=0, nrows-1 do begin
    cog(i) = total(output(*,i) * lin2) / total(output(*,i))
  endfor
endif
cog_fit = curvefit(x, cog, weight, a, sigmaa, $
                  function_name='sine_wave')
cog_mean = a(0) - 1.
error_after = cog_mean - (ncols-1)/2.
if (keyword_set(debug)) then print, format=(a, f8.2, a, f8.2)', $

```

```

    'Fitted center of gravity after correction= ', cog_mean, ' +/-', sigmaa(0)
    if (keyword_set(debug)) then print, format='(a,f8.2)', $
    'Error after correction (offset from center of image) = ', error_after
endif

cog = [[cog], [cog_fit]]

if (keyword_set(debug)) then print, "Sinogram used average of "+string(air_values)+"
pixels for air"
if (keyword_set(debug)) then print, "Skipped "+string(acc_values)+" acceleration pixels"
if (n_elements(backlash) ne 0) then begin
    if (keyword_set(debug)) then print, "Backlash corrected "+string(back)+" pixels"
endif
if (n_elements(center) ne 0) then begin
    if (keyword_set(debug)) then print, "Center corrected "+string(error_before)+" pixels"
endif

return, output
end

```

```

*****
*****

```

```

;tomo_filter.pro;+
; NAME:
;   TOMO_FILTER
;
; PURPOSE:
; Filters a sinogram before backprojection. A selection of filters is available.
;
; CATEGORY:
;   Tomography data processing
;
; CALLING SEQUENCE:
;   Result = TOMO_FILTER(Sinogram, Filter_size, D, /GEN_HAMMING, /LP_COSINE,
;/SHEPP_LOGAN, /RAMLAK, /NONE)
;
; INPUTS:
;   Sinogram:   The unfiltered sinogram. This must be a 2-D array.
;
; OPTIONAL INPUTS:
;   FILTER_SIZE: The half-size of the filter in pixels. The default is 32.
;   D:           An additional filter parameter. The default is 1.0
;

```

```

; KEYWORD PARAMETERS:
; /GEN_HAMMING: Setting this keyword causes the function to use a
GEN_HAMMING filter.
; /LP_COSINE: Setting this keyword causes the function to use an LP_COSINE filter.
; /SHEPP_LOGAN: Setting this keyword causes the function to use a Shepp-Logan
filter.
; This is the default.
; /RAMLAK: Setting this keyword causes the function to use a RAMLAK filter.
; /NONE: Setting this keyword causes the function to use no filter.
;
; OUTPUTS:
; This function returns the filtered sinogram.
;
; PROCEDURE:
; For each row in the sinogram, this function simply does the following:
; Pads the input sinogram
; Does a convolution with the appropriate filter
; The code for the filters was taken from the IDL tomography demo program which is
included in
; the IDL distribution. It would be easy to add additional filters in the future.
;
; EXAMPLE:
; f = tomo_filter(sinogram, /Shepp_Logan)
;
; MODIFICATION HISTORY:
; Written by: Mark Rivers, May 13, 1998
;-

```

```

; *** *** Reconstruction Filters from IDL reconstruction demo *** ***

```

```

Function None, x, d
return, [1.0]
end

```

```

Function RAMLAK, x, d
zero = where(x eq 0.0, count)
q = x
if (count ne 0) then q(zero) = .01
y = -sin(!pi*x/2)^2 / (!pi^2 * q^2 * d)
.*****
;caution
.*****
d=1.0 ;??? the line abobe modify 'd' ???????
if count ne 0 then y(zero) = 1./(4.*d)

```

```
return, y
end
```

```
Function Shepp_logan, x, d
d = !pi^2 * d * (1.-4.*x^2)
zeros = where(abs(d) le 1.0e-6, count)
if count ne 0 then d(zeros) = .001
return, 2./d
end
```

```
Function lp_cosine, x, d
return, 0.5 * (ramlak(x-.5,d) + ramlak(x+.5,d))
end
```

```
Function Gen_Hamming, x, d, alpha
if n_elements(alpha) le 0 then alpha = 0.5
return, alpha * ramlak(x,d) + ((1.-alpha)/2) * (ramlak(x-1,d) + ramlak(x+1,d))
end
```

```
function tomo_filter, image, filter_size, d, gen_hamming=gen_hamming,
lp_cosine=lp_cosine, $
shepp_logan=shepp_logan, ramlak=ramlak, none=none
if (n_elements(filter_size) eq 0) then filter_size = 32
nfilter = 2*filter_size+1
x = findgen(nfilter)-filter_size
if (n_elements(d) eq 0) then d=1.0
if (keyword_set(gen_hamming)) then filter = gen_hamming(x, d) else $
if (keyword_set(lp_cosine)) then filter = lp_cosine(x, d) else $
if (keyword_set(shepp_logan)) then filter = shepp_logan(x, d) else $
if (keyword_set(ramlak)) then filter = ramlak(x, d) else $
if (keyword_set(none)) then filter = none(x, d) else $
filter = shepp_logan(x,d)
size = size(image)
ncols = size[1]
nrows = size[2]
s = image
temp = fltarr(ncols + 2*nfilter)
for i=0, nrows-1 do begin
; Pad array with data from first and last columns
temp[0:nfilter-1] = image[0,i]
temp[nfilter+ncols-1:ncols+2*nfilter-1] = image[ncols-1,i]
temp(nfilter) = image(*,i)
temp = convol(temp, filter)
s(0,i) = temp(nfilter : nfilter+ncols-1)
endfor
```

```
return, s
end
```

```
*****
*****
```

```
Pro b1_read_data is the main code used to obtain sinograms for 3-D data. This code
includes subroutines(other files) such as sinogram and tomofilter with reconstruction
method 1
```

```
*****
*****
```

```
; b1_read_data.pro
; PURPOSE:
; reconstructino procedure using back projection method
; size reduction of raw data
; CATEGORY:
;   Tomography data processing
;
; CALLING SEQUENCE:
;
; INPUTS:
;   CT_Arrays(slice, x_dim,y_dim), or raw data obtained by
;   Digital detector at x-15A at BNL
;
; OPTIONAL INPUTS:

; KEYWORD PARAMETERS:

; OUTPUTS:
;   This program returns reconstructed tomography image.
;
; PROCEDURE:
;process raw data
;modify raw data to sinogram
;filter the sinogram
;reconstruct data using riemann sum command
; EXAMPLE:
;
; MODIFICATION HISTORY:
;   Written by:   Hironobu Horiba Dec. 2002
;               Zhong Zhong
;-
```

```
function to_char, number
    chars='000000'+strcompress(string(number), /remove_all)
```

```

        length=strlen(chars)
        chars=strmid(chars, length-4, length)
return, chars
end

pro b1_read_data
;parameters
key='h:\hiro\bnl_feb_03\'
myfile='b2'

analyzer_positions=1 ; number of analyzer positions taken
                    ; set this number to the position
                    ; where you would like to analyz

read_data=-1

imgcheck =-1 ;check the height where data duplicate
           ;change myfile to get another height
adjdata =-1 ;obtain data which are removed detector
           ;artifacts
make_sino =1

;y0=636 the hight where the data trimmed
;y1=704

;air=20
;rot=360
;bck=20

bin_size=4
acc_values=50/bin_size
air_values=150/bin_size
filter_size=30
filter_d=1

processed_dir=key+'data_obtained\'
analyzed_dir =key+'data_analyzed\'
sino_dir =key+'sino\'+'myfile+'\'
;image_dir=key+'images\'
;data_dir=key+'data\'

c='_'+strcompress(string(analyzer_positions), /remove_all)
bck_file=myfile+c+'_bck'
air_file=myfile+c+'_air'

```

```

img_file=myfile+c+'_img'

if (read_data gt 0) then begin

    print,'reading background data'
    restore, processed_dir+bck_file
    ct_array=float(ct_array)
    sz=size(ct_array)
    n_hframes=sz(1)
    nx=sz(2)
    ny=sz(3)
    bck=reform(rebin(ct_array, 1, nx, ny))
;rebin==compression and averaging data

    print,'reading air data'
    restore, processed_dir+air_file
    ct_array=float(ct_array)
    sz=size(ct_array)
    n_frames=sz(1)
    nx=sz(2)
    ny=sz(3)
    air=reform(rebin(ct_array, 1, nx, ny))

    print,'reading image data'
    restore, processed_dir+img_file
    ct_array=float(ct_array)
    sz=size(ct_array)
    n_frames=sz(1)
    nx=sz(2)
    ny=sz(3)

    print, 'end of reading files'
    expand, bck, nx/bin_size, ny, bck
    expand, air, nx/bin_size, ny, air
;expand=resize data by bylinear interpolation

;setting array and norm for raw data adjustment
;to remove detector artifacts
    sct_array=fltarr(n_frames, nx/bin_size, ny)
    norm=air-bck
    norm=norm > 1.
endif
;*****
;check the height where image duplicate in two data sets

```

```

;this part should be done just one time
  if (imgcheck gt 0) then begin
    ct_array_slice=ct_array[0:39,*,*]
    help, ct_array_slice
    tvsize,reform(ct_array_slice[1,*,*])
    write_ary, ct_array_slice, analyzed_dir+ myfile+'imgcheck'
    ;check another program further analysis
  endif
;*****

  if (adjdata gt 0) then begin
    for i=0, n_frames-1 do begin

      this_image=reform(ct_array(i, *, *))
      expand, this_image, nx/bin_size, ny, this_image
      this_image=(this_image-bck)
      this_image=this_image > 1.
      sct_array(i, *, *)=this_image/norm
    endfor

    save, filename=analyzed_dir+ myfile+'adjusted.dat', sct_array, /verbose
  endif

  if (make_sino gt 0) then begin
    restore, analyzed_dir+ myfile+'adjusted.dat'
    sct_array=sct_array[0:179,*,9:58]
    sz=size(sct_array)
    num_slices=sz(3)
    ;sino_dir
    for i=0,num_slices-1 do begin
      sino=reform(sct_array(*, *, i))

      file_names='_sino'
      str_i=to_char(i)
      file_names=file_names+str_i
      save, filename=sino_dir+myfile+c+file_names, sino, /verbose
      ;ex)filename==b11_sino
      ;tvsize,sino
      ;wd
    endfor
  endif
stop
end

```

```

*****
*****
Pro b2_volrender_abs_t1 is the main code used to obtain voxel array for 3-D data of
absorption images. This code is reconstructed using method 1.
*****
*****
PRO b2_volrender_abs_t1

img_key='h:\hiro\obtained_img\'
myfile='b2'

restore, img_key+'b2images\'+'myfile'+volume_abs_t1.dat'
v=vol_abs
stop
undefine, vol_abs

redo=0
if redo then begin
;***** trim the array using notch filter and padding filter *****
restore, img_key+'b2images\'+'notch_b2.dat'
pad=1.-notch3D
med=median(v[208:284,145:183,0:39]) ;calculate median value of lucite
med=med/2.
pad=pad*med
v=v*notch3D
v=v+pad
undefine, notch3D
undefine, pad
;*****
endif
;stop

sz=size(V)
Vx=sz(1)
Vy=sz(2)
Vz=sz(3)

V_max=max(V) ;28.834
V_min=min(V) ;1.99051
;V=V > V_min/3.
;V=V < V_max/5.
;V=(V-V_min)/(V_max-V_min)*255
;V_max_scaled=max(V)
;V_min_scaled=min(V)
;stop

```

```

V=bytsc1(V)
stop

;creating slices of x-z plane
redo=1
if redo then begin
while (redo eq 1) do begin
read, y, prompt='enter y(end=-1)'
wd
if (y eq -1) then begin
redo=-1
print, redo
endif else begin
y=fix(y)
str_y=strcompress(string(y), /remove_all)
v_slice=reform(v[*],y,*)
tvsize, v_slice
saveimage, img_key+'b2images\'+'b2_abs_y'+str_y+'.tif',/tiff
endelse
endwhile
endif
stop
; Create the opacity vector:
rgbo = BYTARR(256,2)

;Red and opacity for muscle:outside
;rgbo[30:140, *] = 5

;White and opacity for bone:inside
rgbo[210:255, *] = 1
rgbo[200:209, *] = 1
rgbo[190:199, *] = 5
rgbo[185:189, *] = 0
rgbo[180:184, *] = 0
rgbo[170:179, *] = 10
rgbo[160:169, *] = 10
rgbo[155:159, *] = 10
rgbo[150:154, *] = 10
rgbo[144:149, *] = 10
rgbo[140:143, *] = 10
rgbo[130:139, *] = 10
rgbo[120:129, *] = 10
rgbo[110:119, *] = 10
rgbo[100:109, *] = 10

```

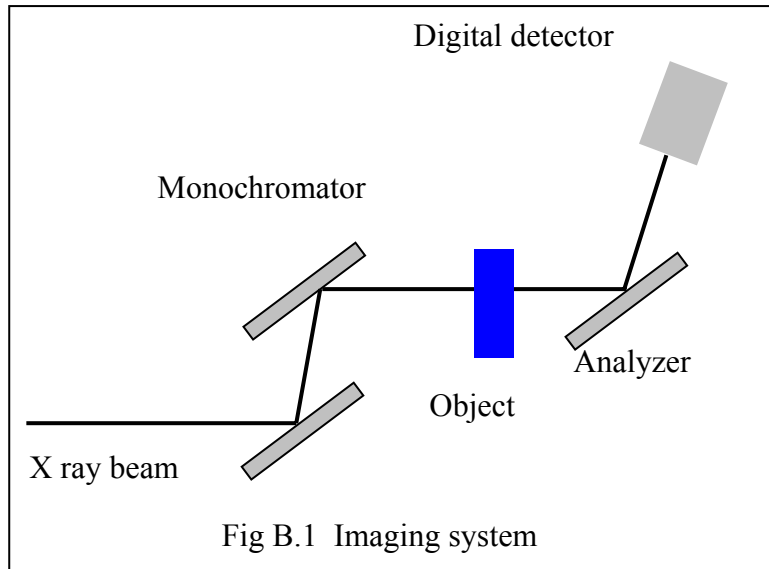
```

rgbo[90:99, *] = 10
rgbo[80:89, *] = 10
rgbo[70:79, *] = 20
rgbo[60:69, *] = 20
rgbo[50:59, *] = 20
rgbo[40:49, *] = 20
rgbo[30:39, *] = 20
rgbo[20:29, *] = 20
rgbo[10:19, *] = 20
rgbo[0:9, *] = 20
;V_max=max(V)
;V_min=5
;V=255*(V-V_min)/V_max
SCALE3, XRANGE=[0, Vx-1], YRANGE=[0, Vy-1], ZRANGE=[0, Vz-1]

result=voxel_proj(V,rgbo)
wd
tvsize, result
;saveimage, img_key+'b2images\'+'b2_abs_3D_img.bmp',/bmp
saveimage, img_key+'b2images\'+'b2_abs_3D_img.tif',/tiff
stop
;window,/free
;T3D ./reset, rot=[0,0,0]
SCALE3, XRANGE=[0, Vx-1], YRANGE=[0, Vy-1], ZRANGE=[0, Vz-1],ax=90
V=byte(V)
result=voxel_proj(V,rgbo)
wd
tvsize, result, title='rotated'
;saveimage, img_key+'b2images\'+'b2_abs_3D_img_original_rot.tif',/tiff
;v_slice=reform(V[*,*],1)
;tvsize, v_slice
stop
end

```

9. Figures



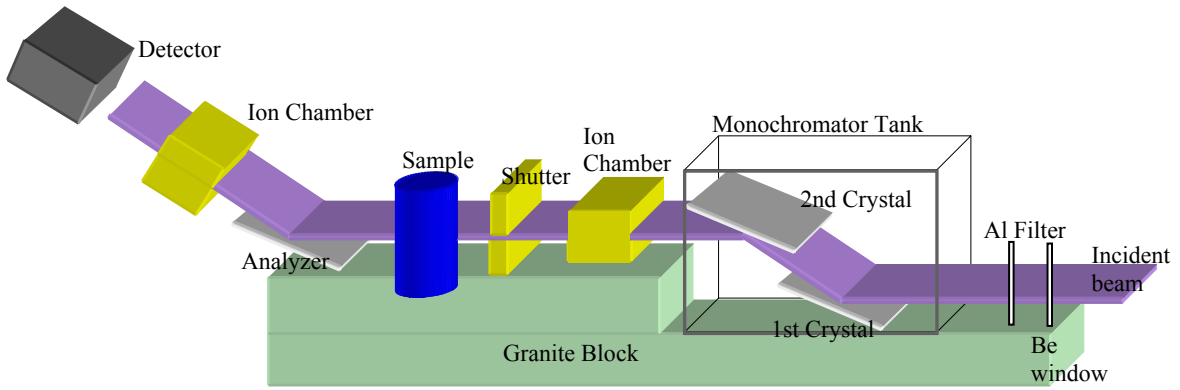
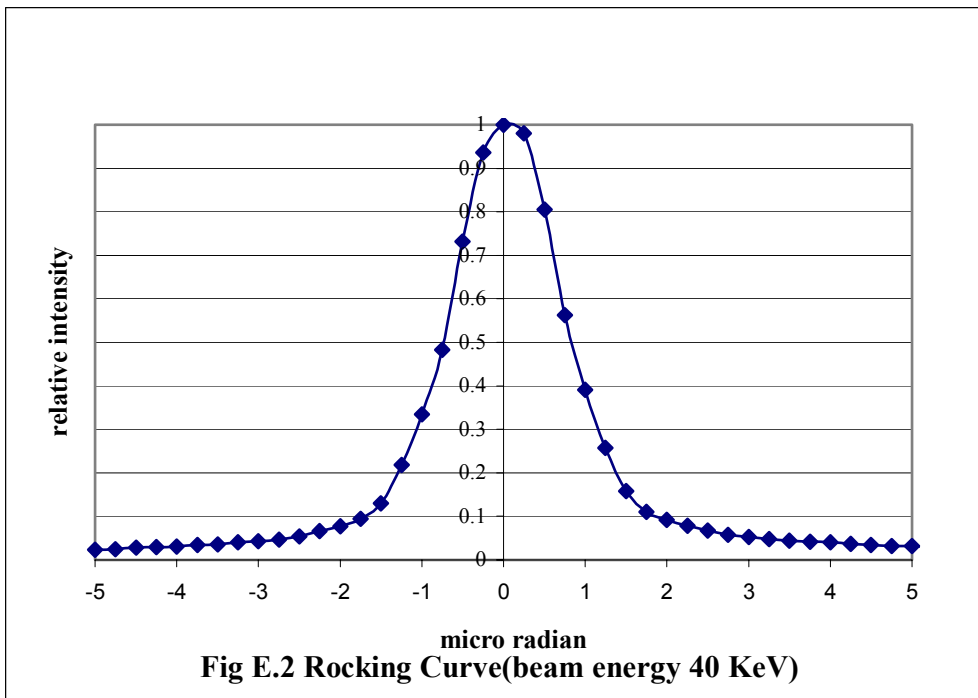


Fig. E1 Set up at the NSLS X15A beamline



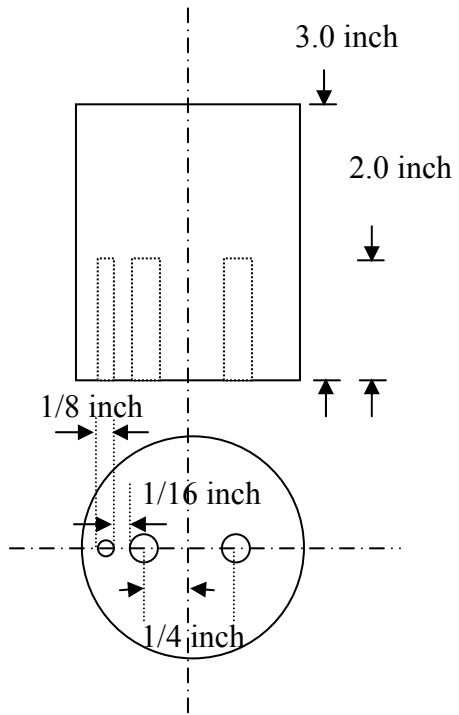


Fig. E3 The design of phantom A

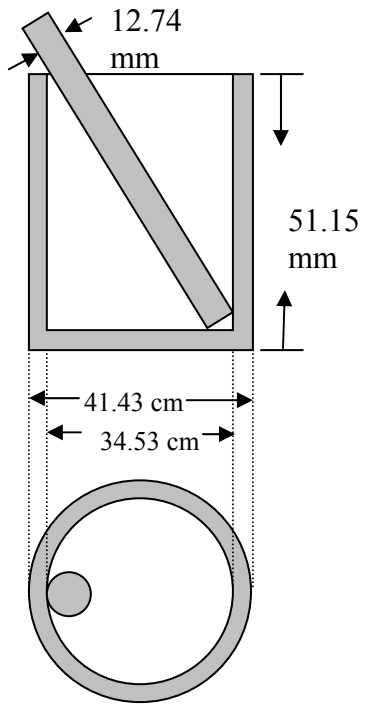


Fig. E4 The design of phantom B

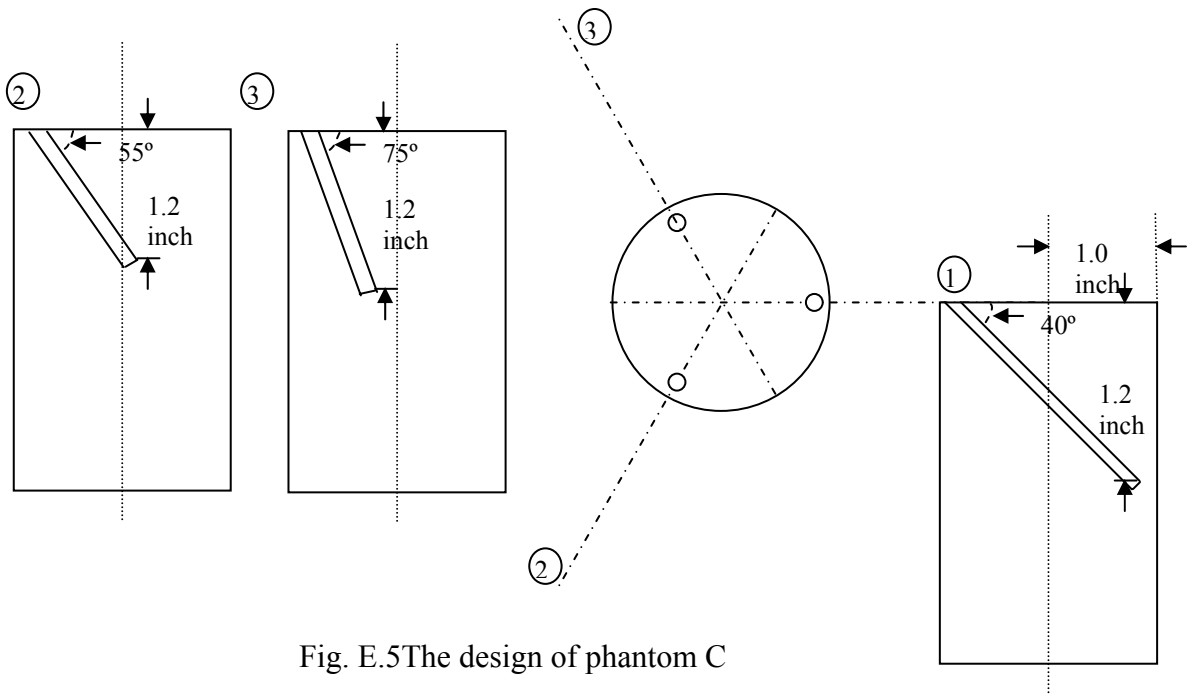


Fig. E.5The design of phantom C

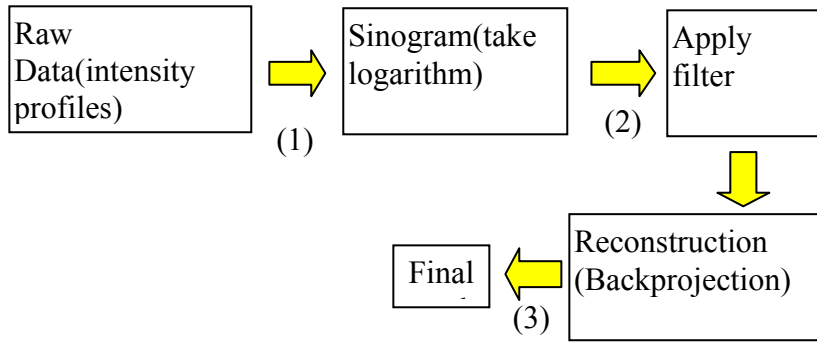


Fig. I.1 The block diagram of image processing procedure

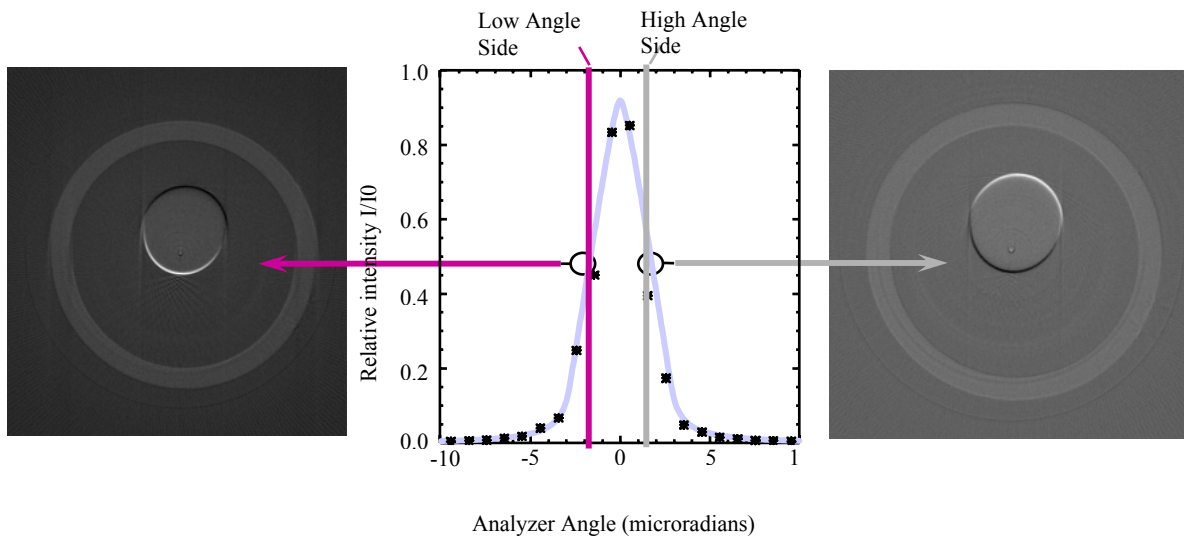


Fig. I.2 The example of Higher and lower side images

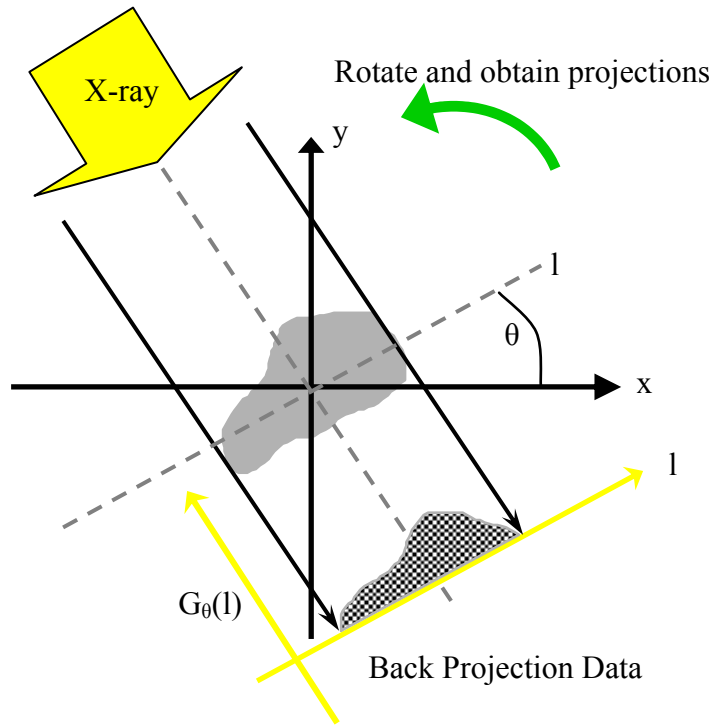


Fig. I.3 Schematics of back projection

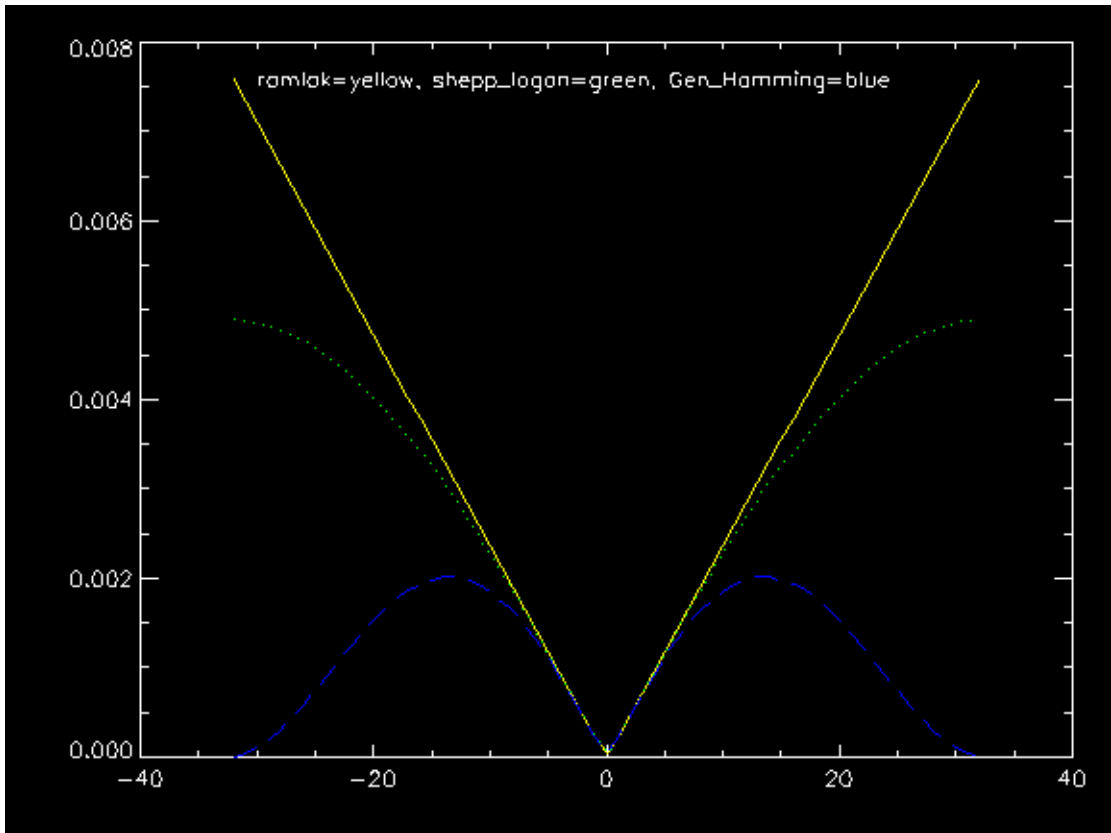


Fig. I.4 Filters in frequency domain. Green line is Shepp Logan Filter

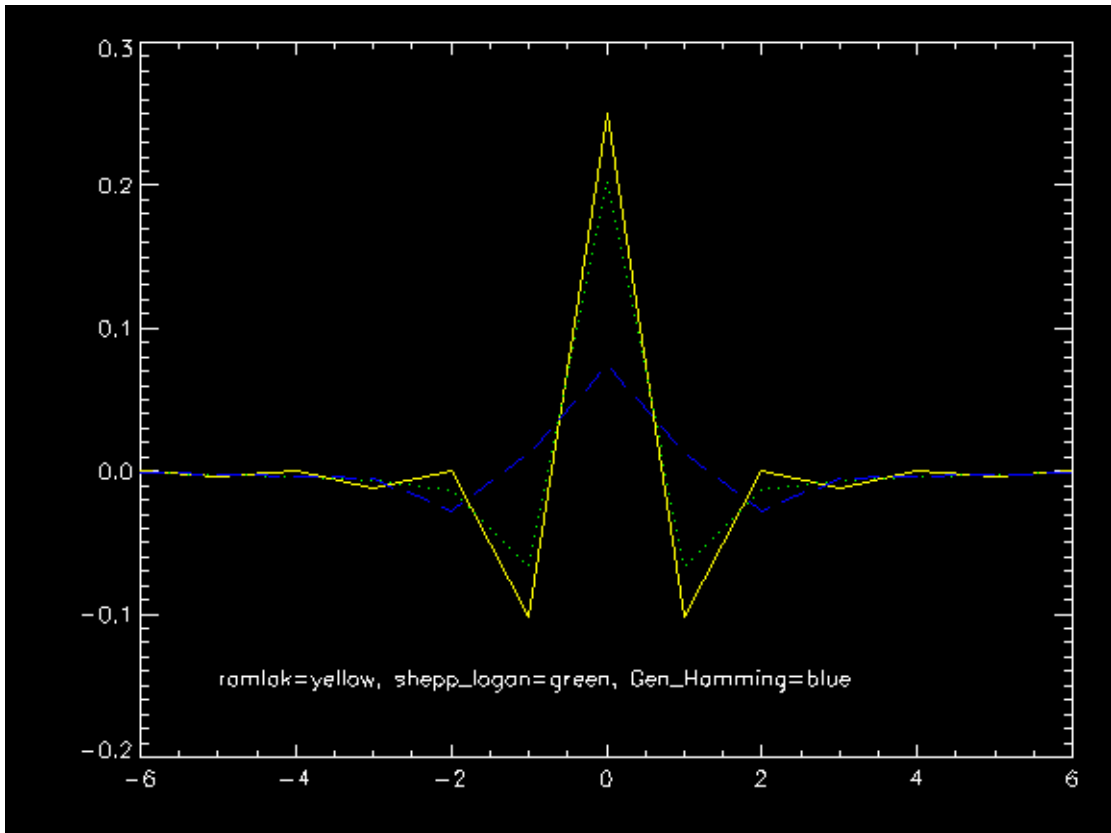


Fig I.5 Filters in spatial domain.



Fig R. 1.1 A slice of the raw data from a projection

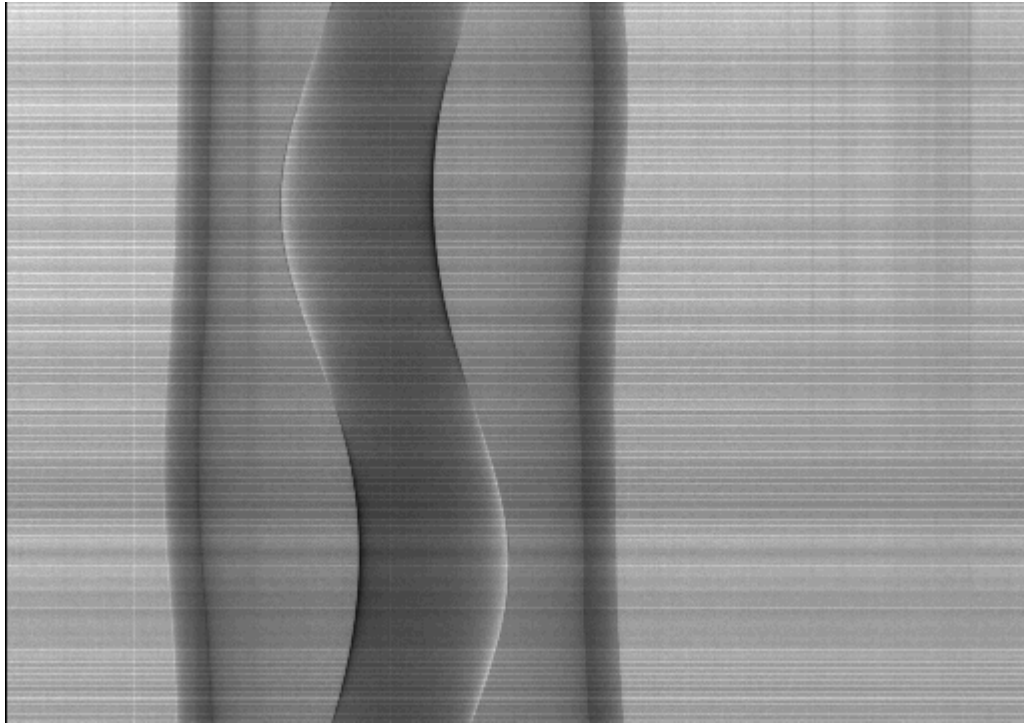


Fig R. 1.2 Raw tomography data of Lucite phantom B at lower side of the rocking curve. All the projections are shown

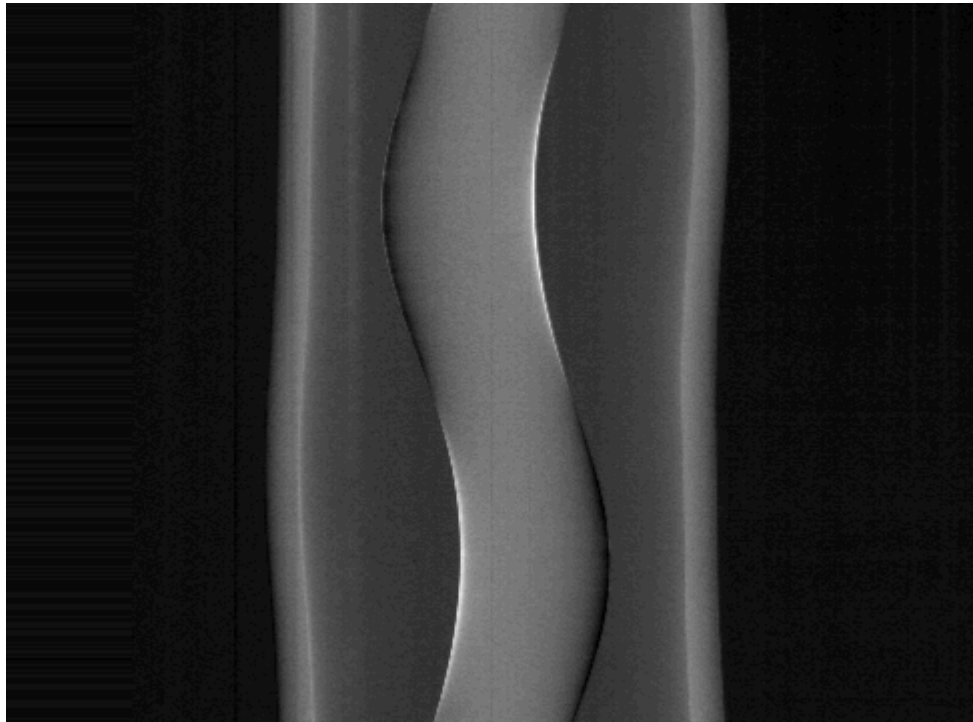


Fig. R. 1.3 Sinogram of Lucite B at lower side of Rocking curve

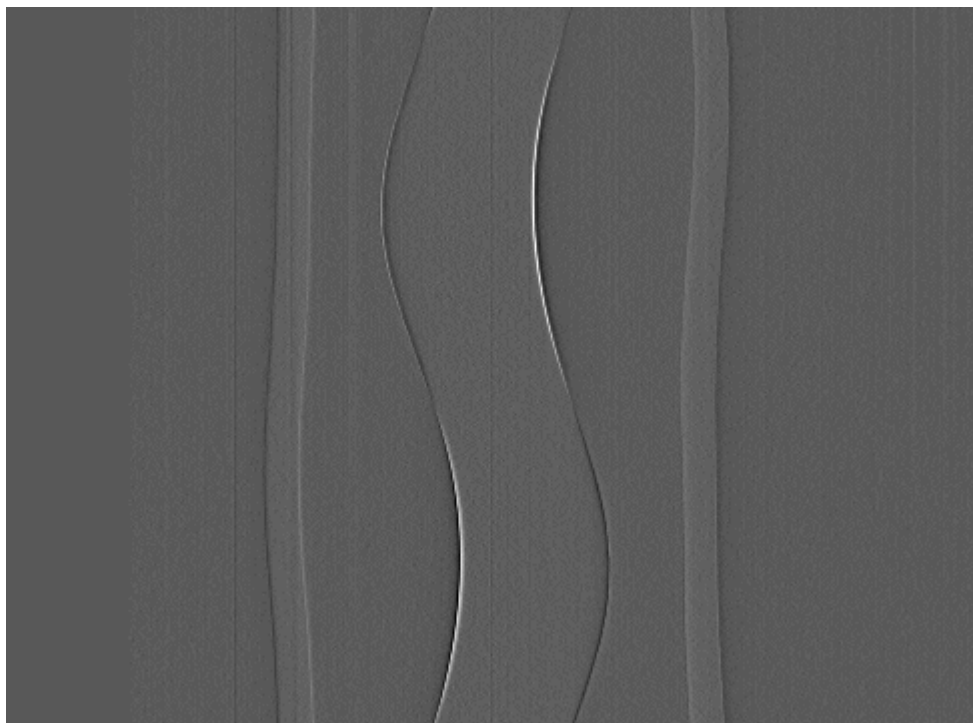
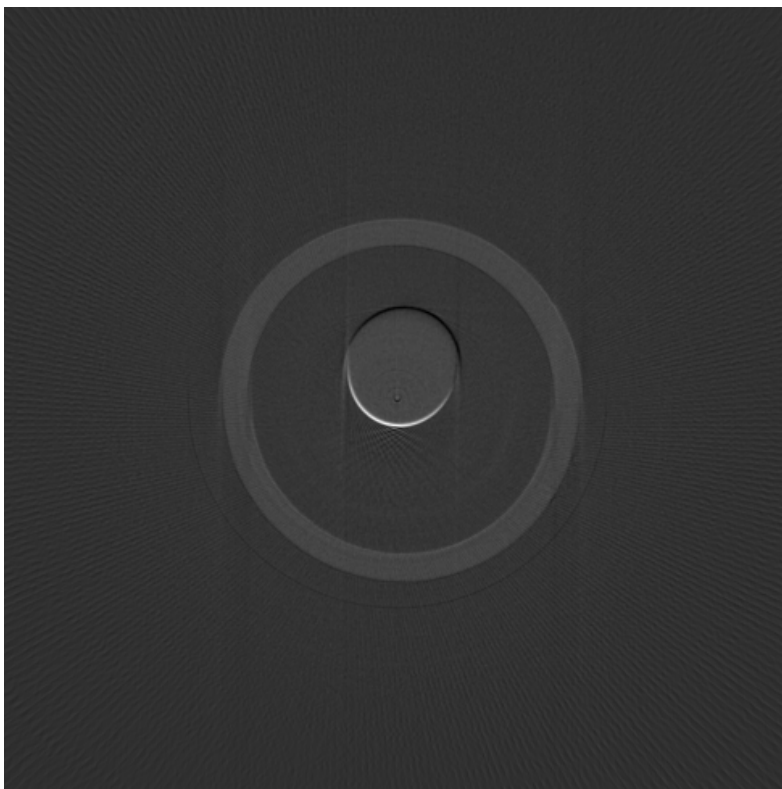


Fig R. 1.4 Sinogram with Shepp Loagan Filter



FigR. 1.5 Reconstructed image with Shepp Logan Filter

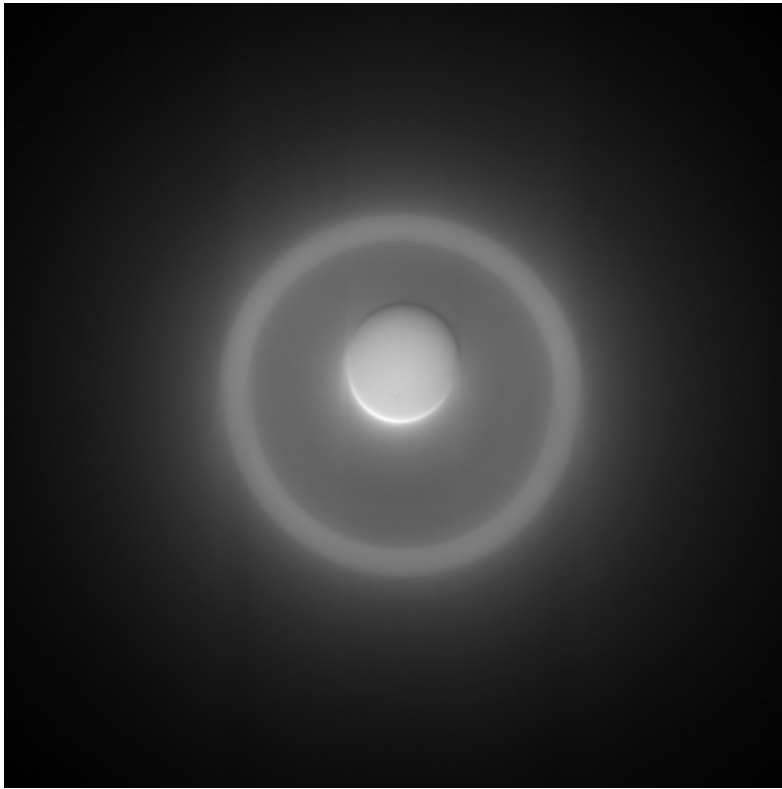


Fig R. 1.6 Reconstructed image without Filter

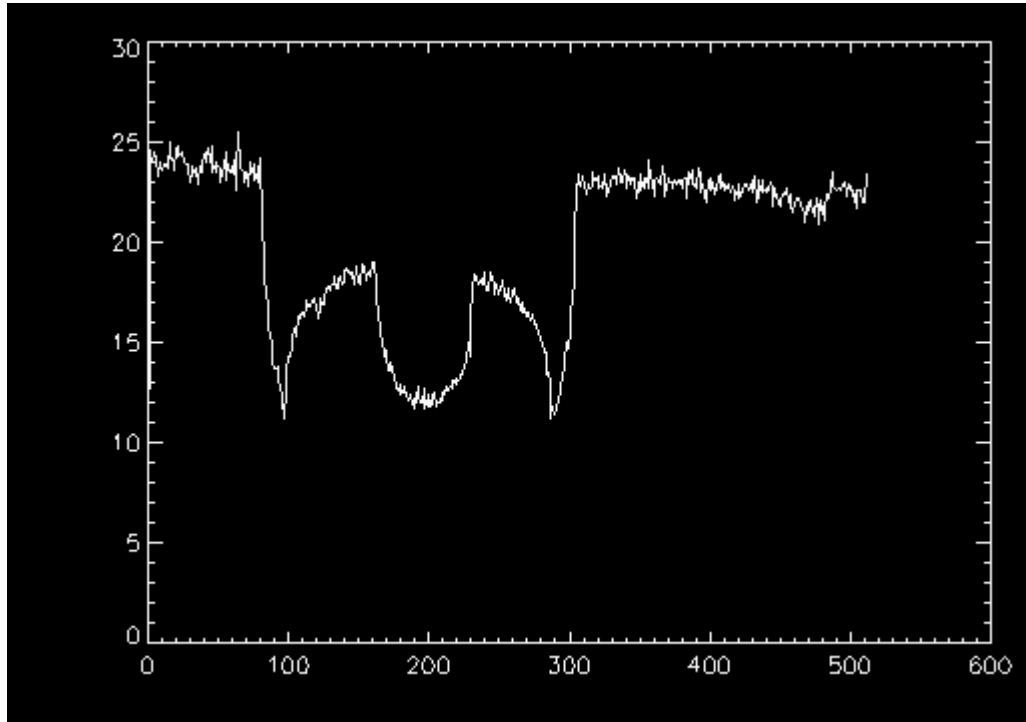


Fig R. 1.7 Line profiles of raw tomography data at $y=169$

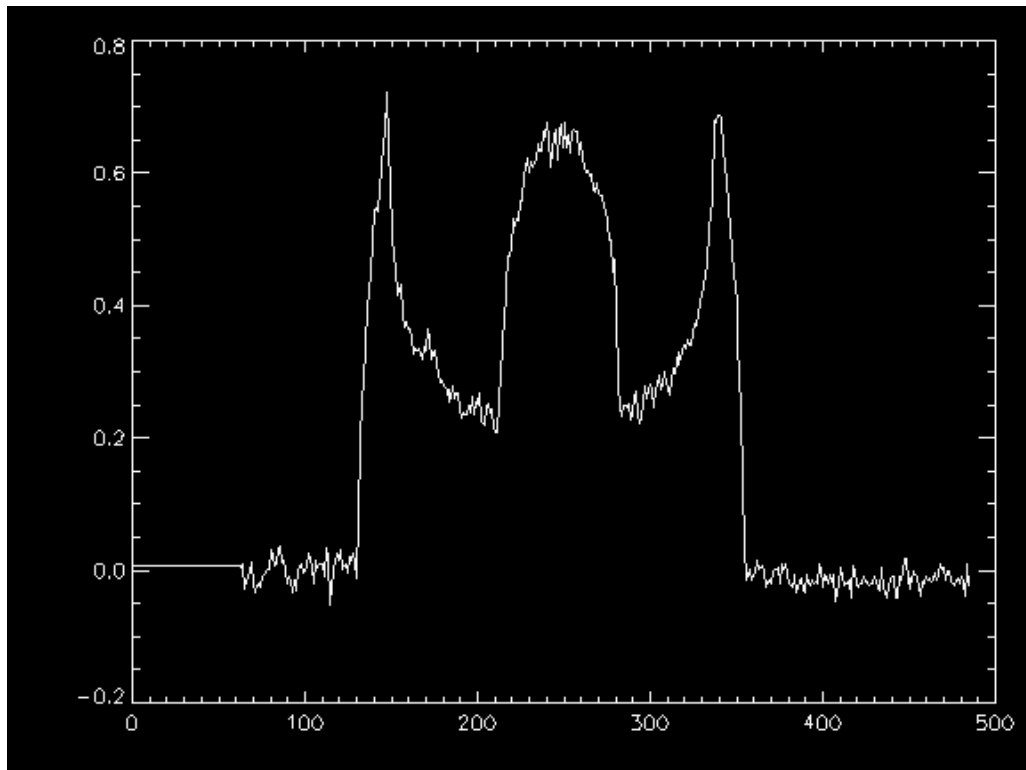


Fig R. 1.8 Line profiles of sinogram at $y=169$

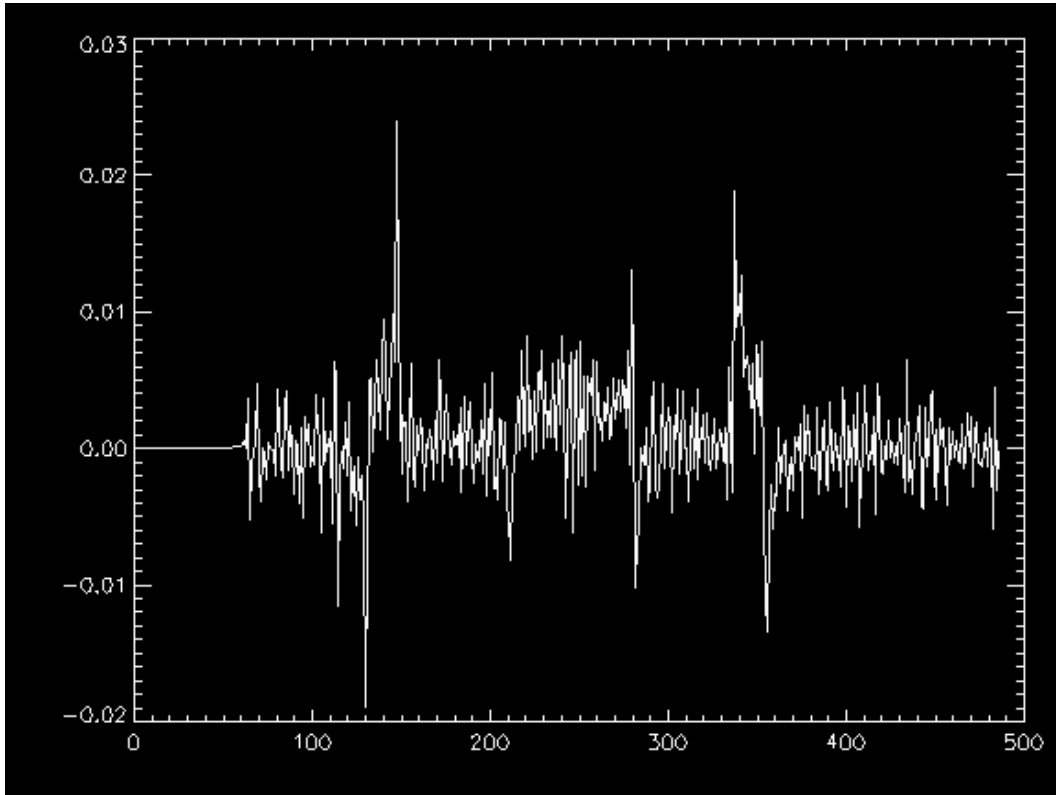


Fig R. 1.9 Line profiles of sinogram at $y=169$ with Shepp Logan filter

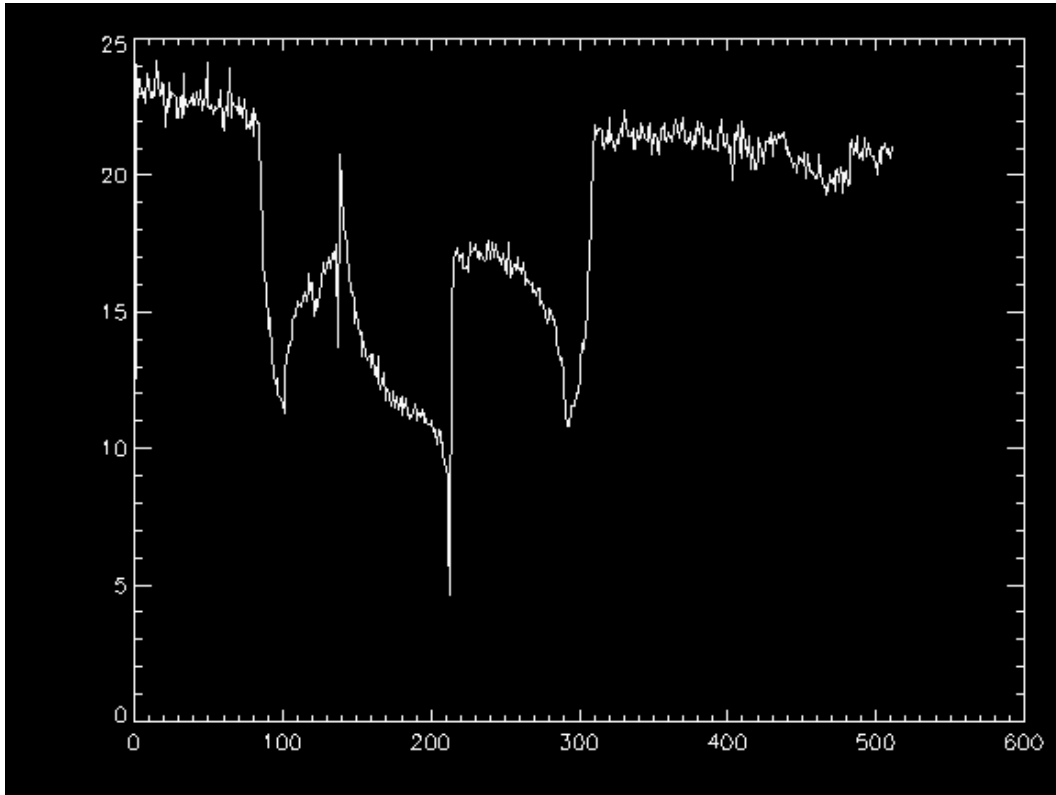


Fig R. 1.10 Line profiles of raw tomography data at $y=255$

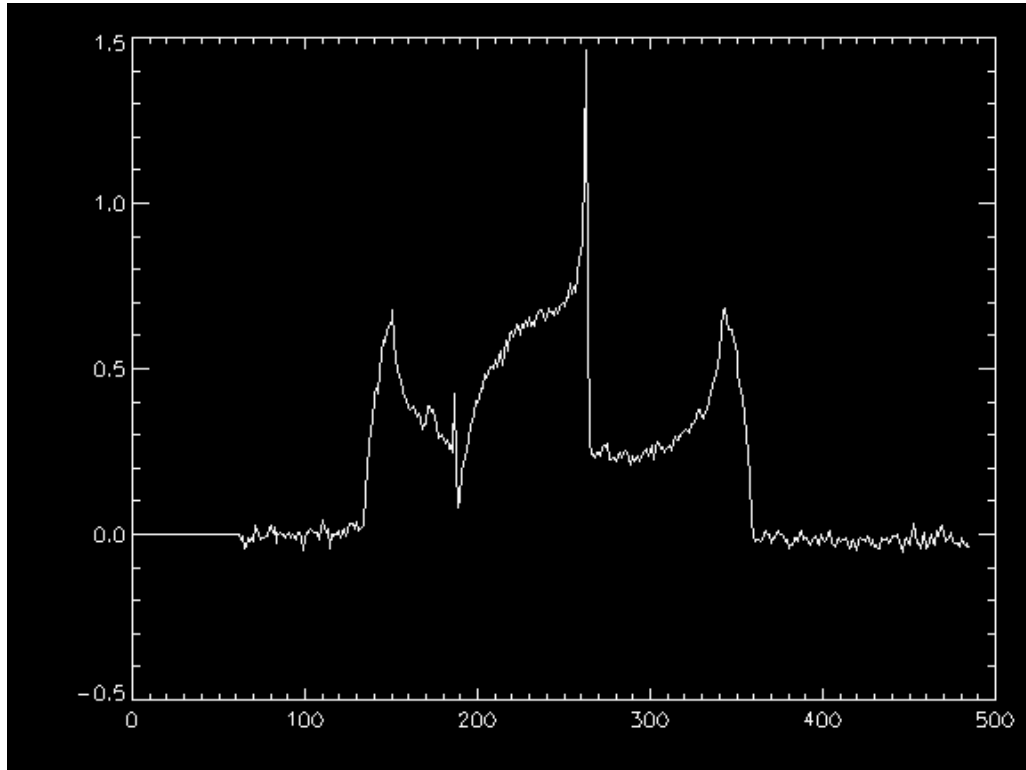


Fig R. 1.11 Line profiles of sinogram at $y=255$

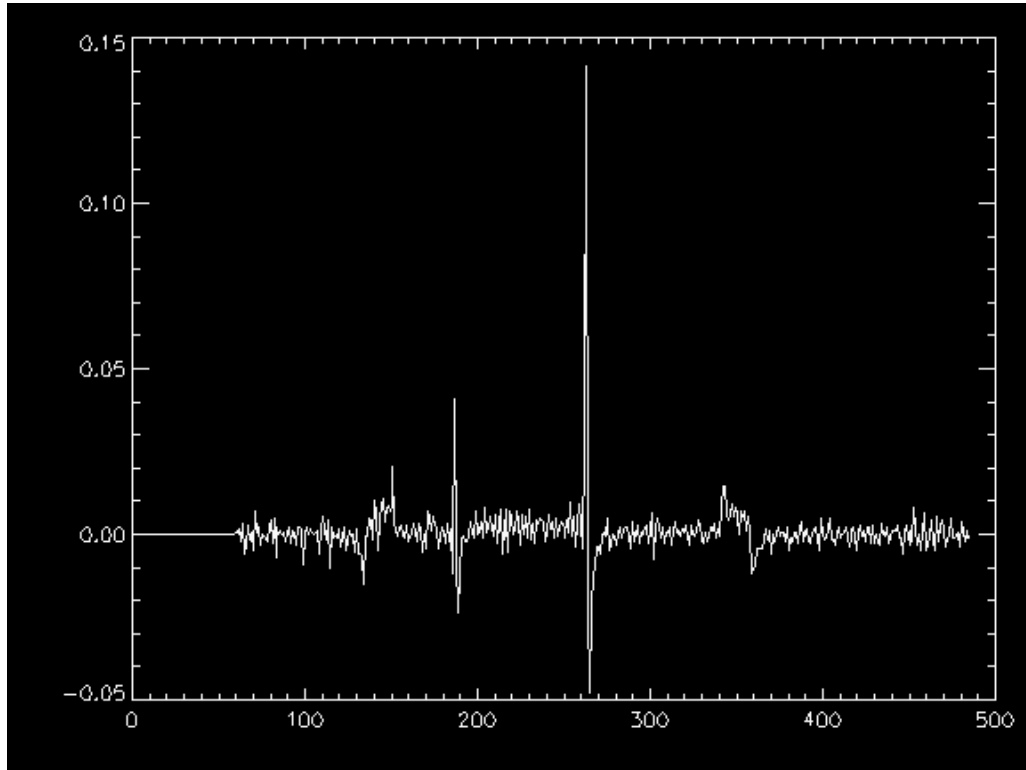


Fig R. 1.12 Line profiles of sinogram at $y=255$ with Shepp Logan filter

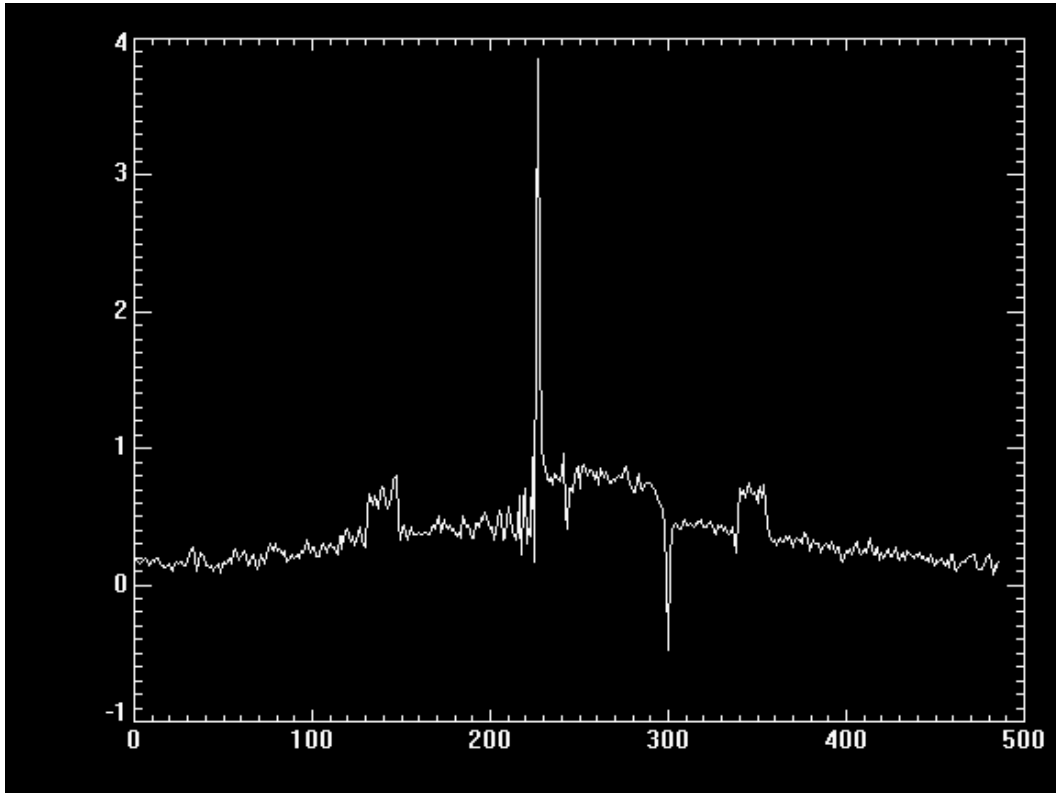


Fig R. 1.13 Line profiles of reconstructed data at $y=255$ with Shepp Logan filter

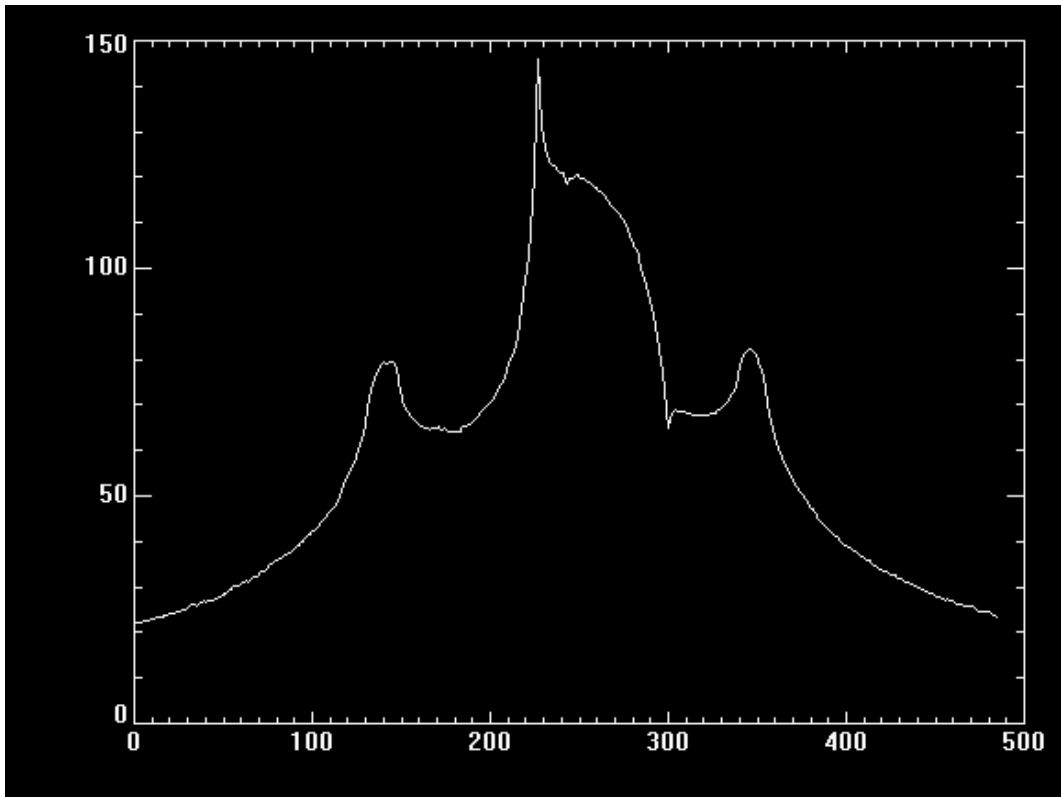


Fig R.1.14 Line profiles of reconstructed data at $y=255$ without filter



Figure R.1.15 A slice of raw data obtained from the detector

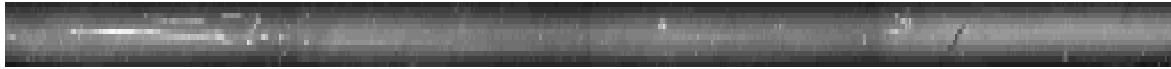


Figure R. 1.16 the normal image for image adjustment

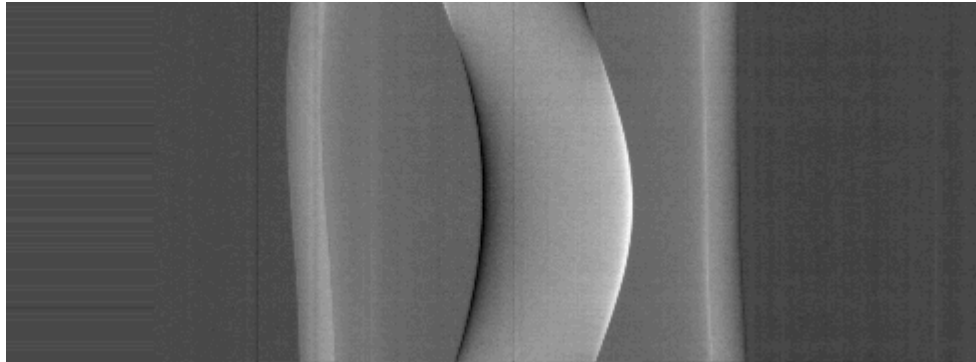


Figure R. 1.17 sinogram of Lucite B at higher side of rocking curve

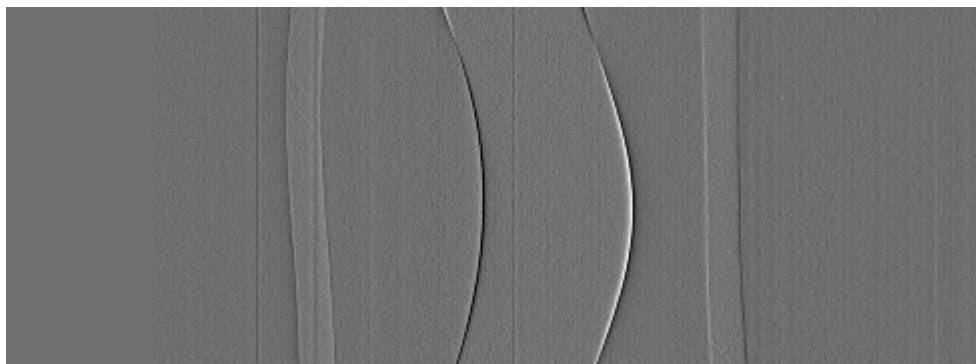


Figure R. 1.18 Sinogram of Lucite B at higher side of rocking curve with Shepp Logan filter

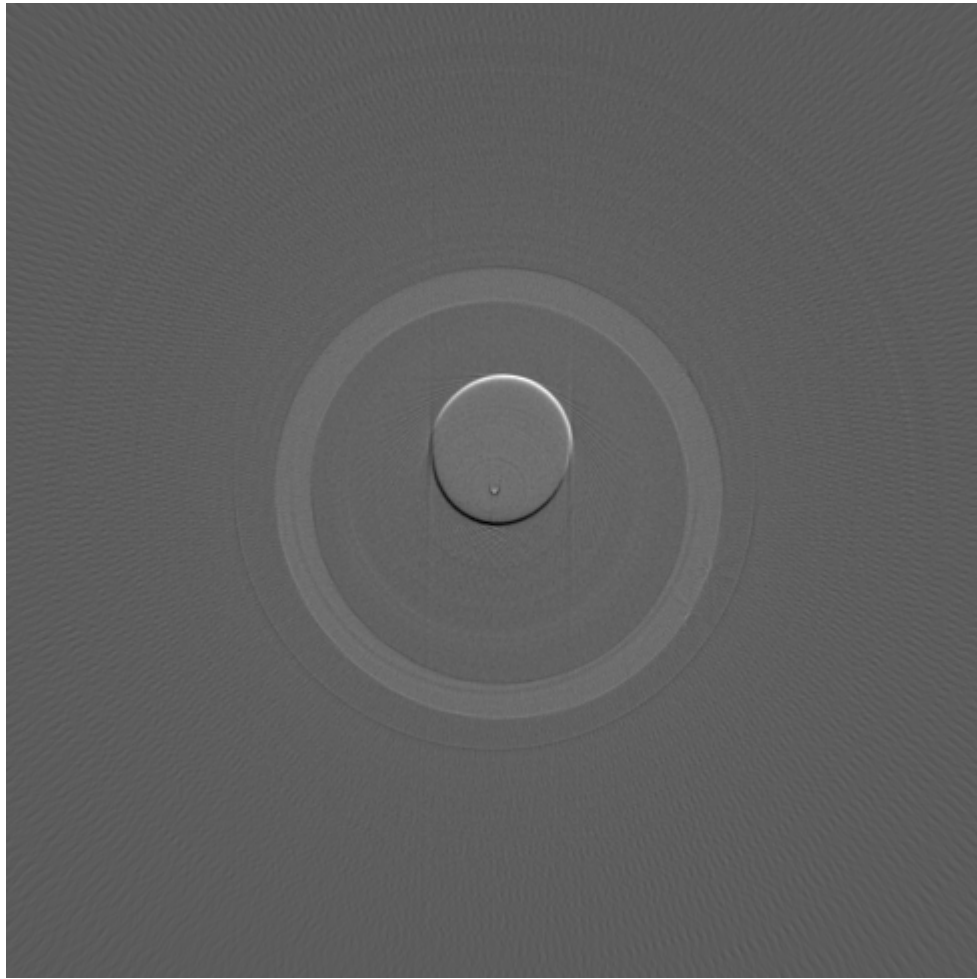


Figure R. 1.19 Reconstructed image with Shepp Logan filter

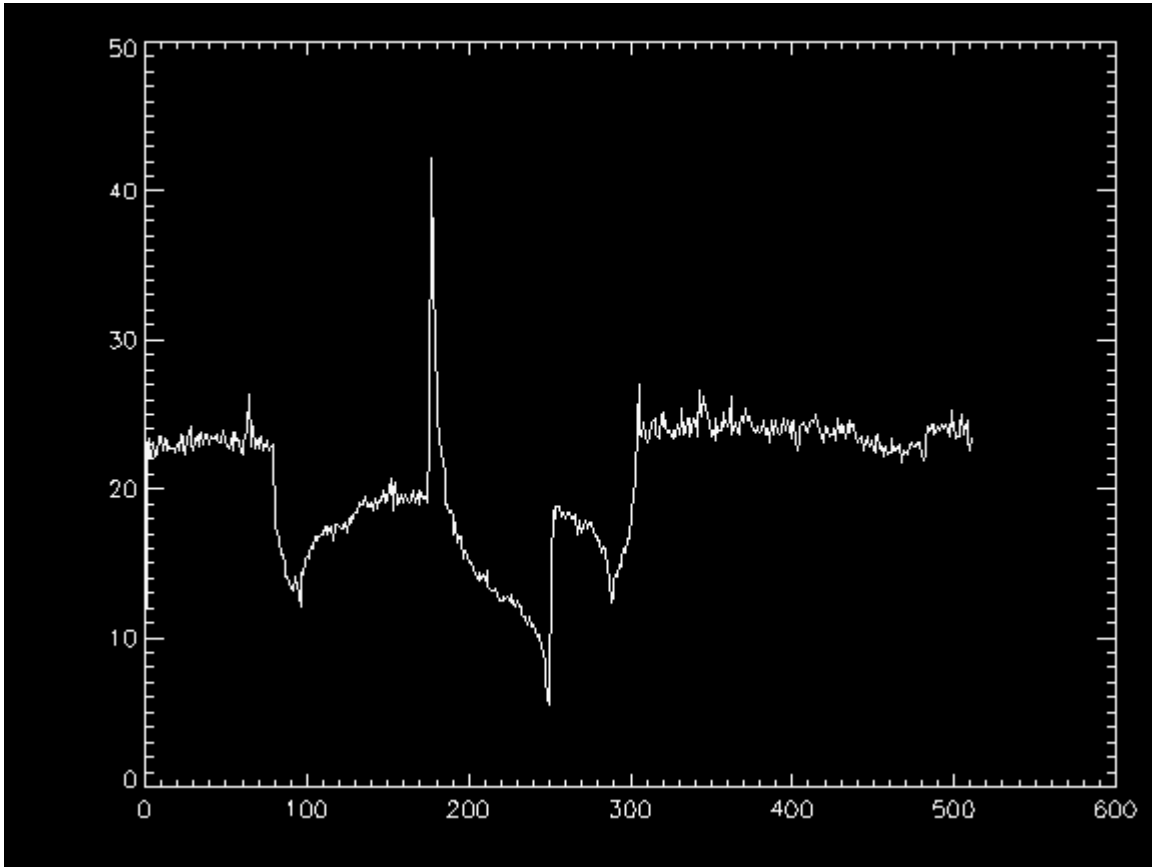


Figure R. 1.20 a line profile of raw tomography data at y=94

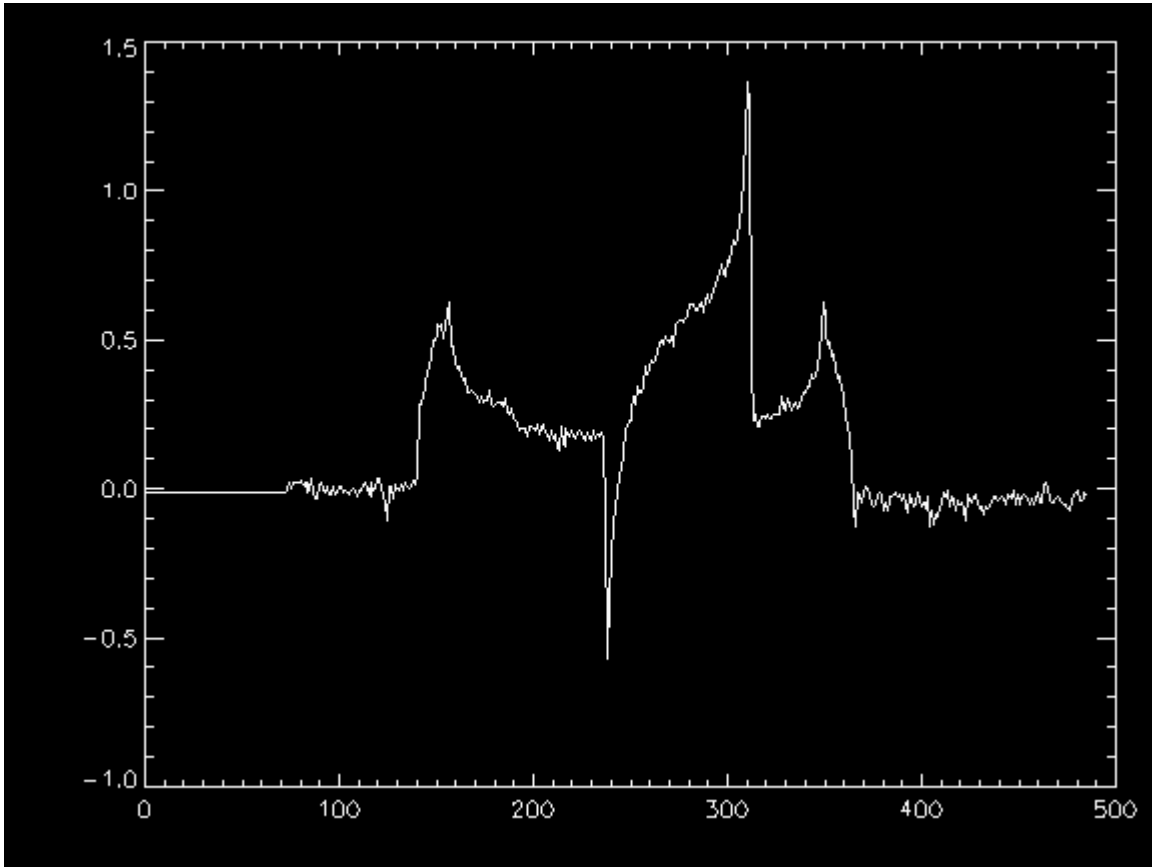


Figure R. 1.21 a line profile of sinogram at $y=94$



Fig. R.1.22 The apparent absorption image of the Lucite B using option 3

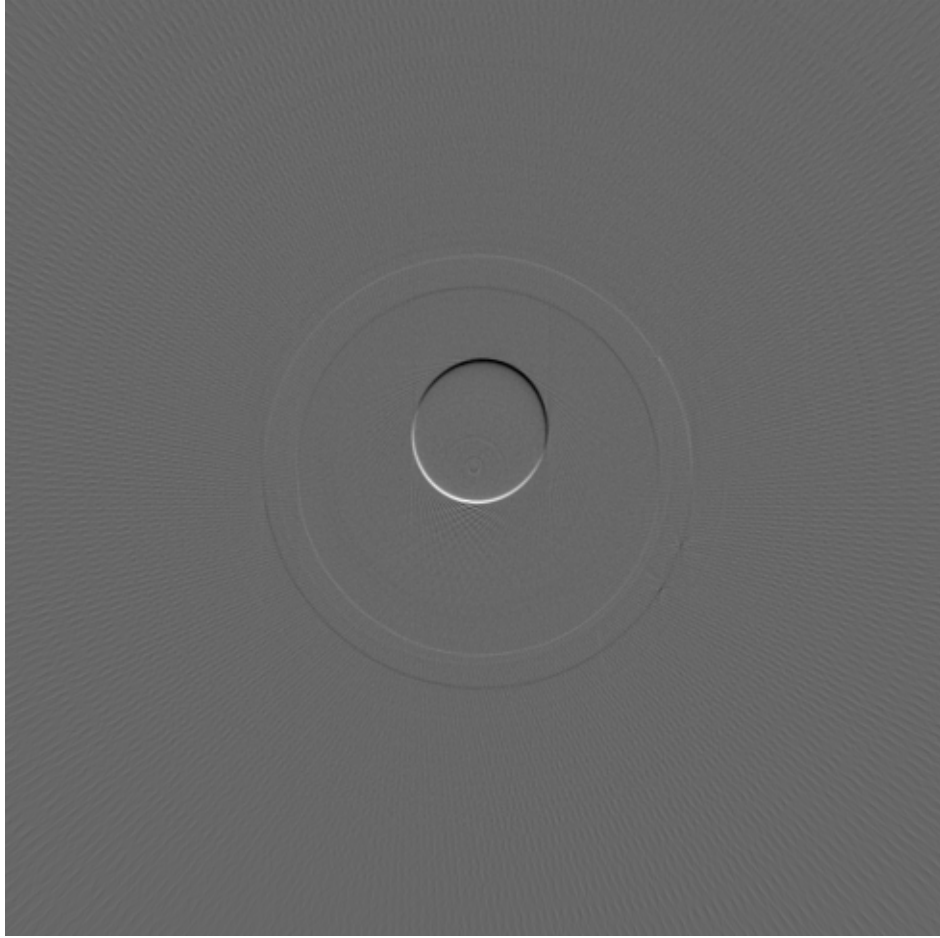


Fig.1.23 The refraction image of the Lucite B using option 3

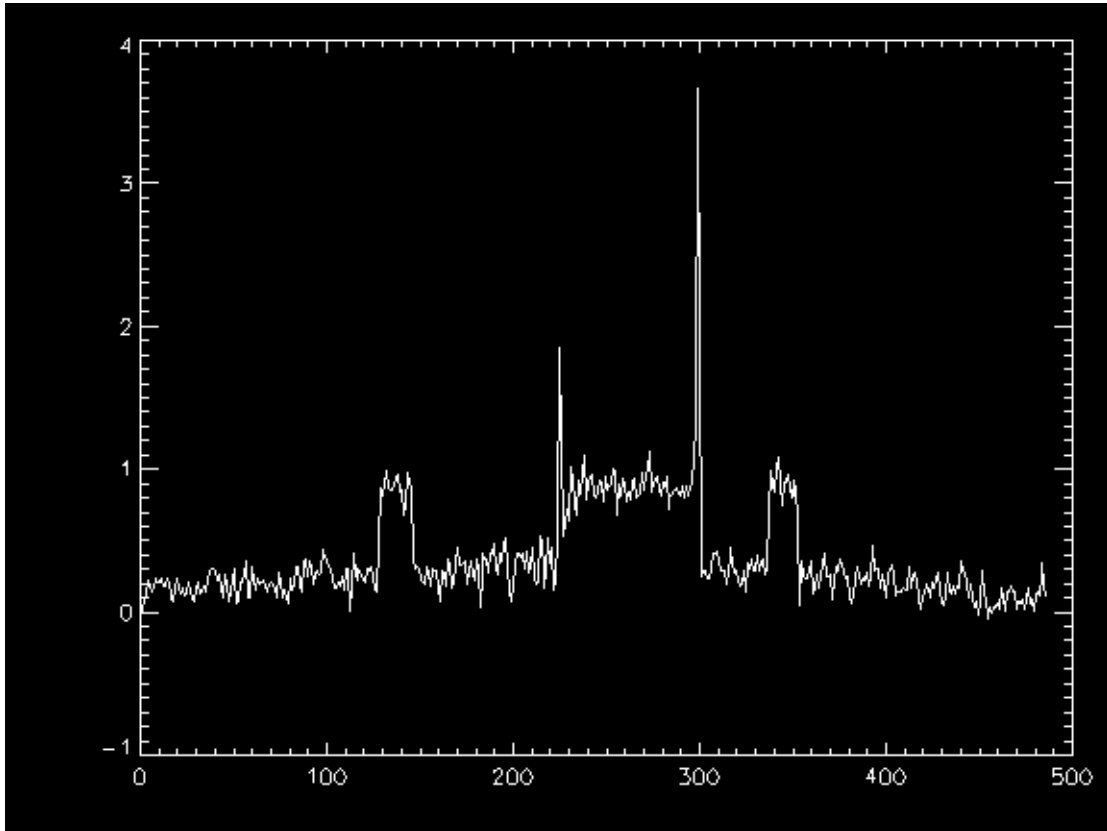


Fig.R.1.24 A line profile of absorption image of the phantom B using option 3

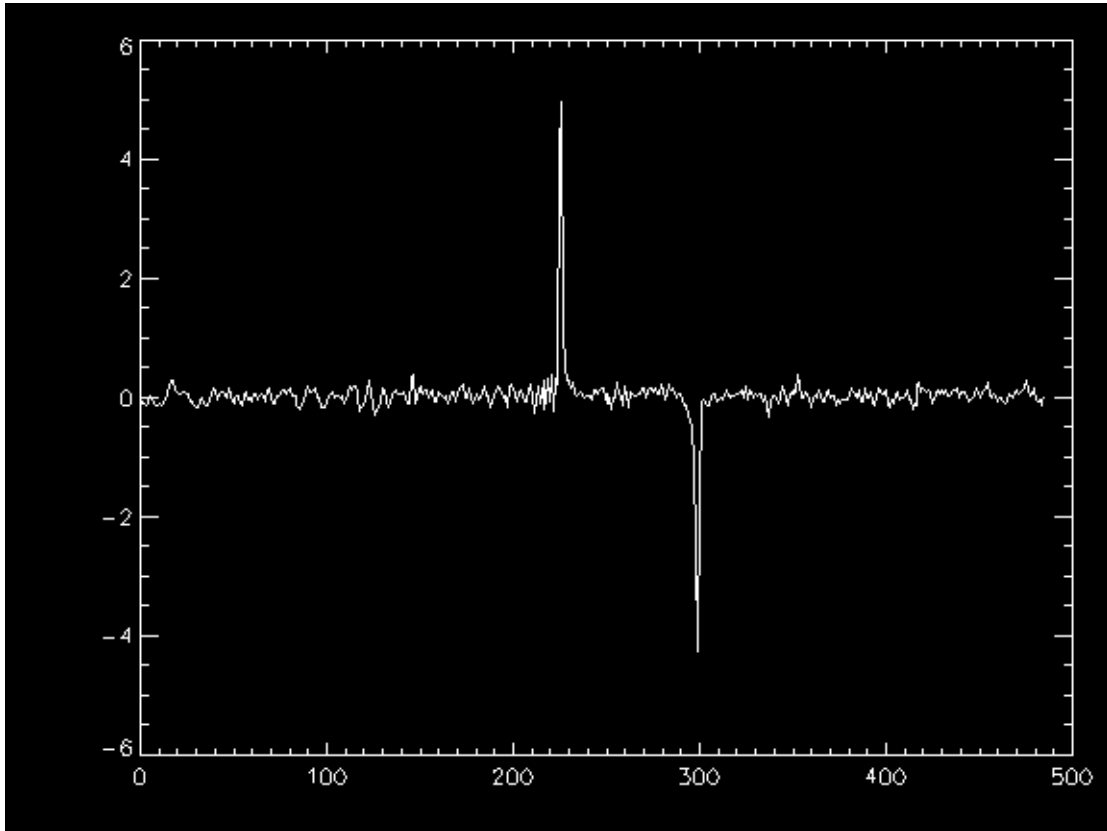


Fig.R.1.25 A line profile of refraction image of the phantom B using option 3

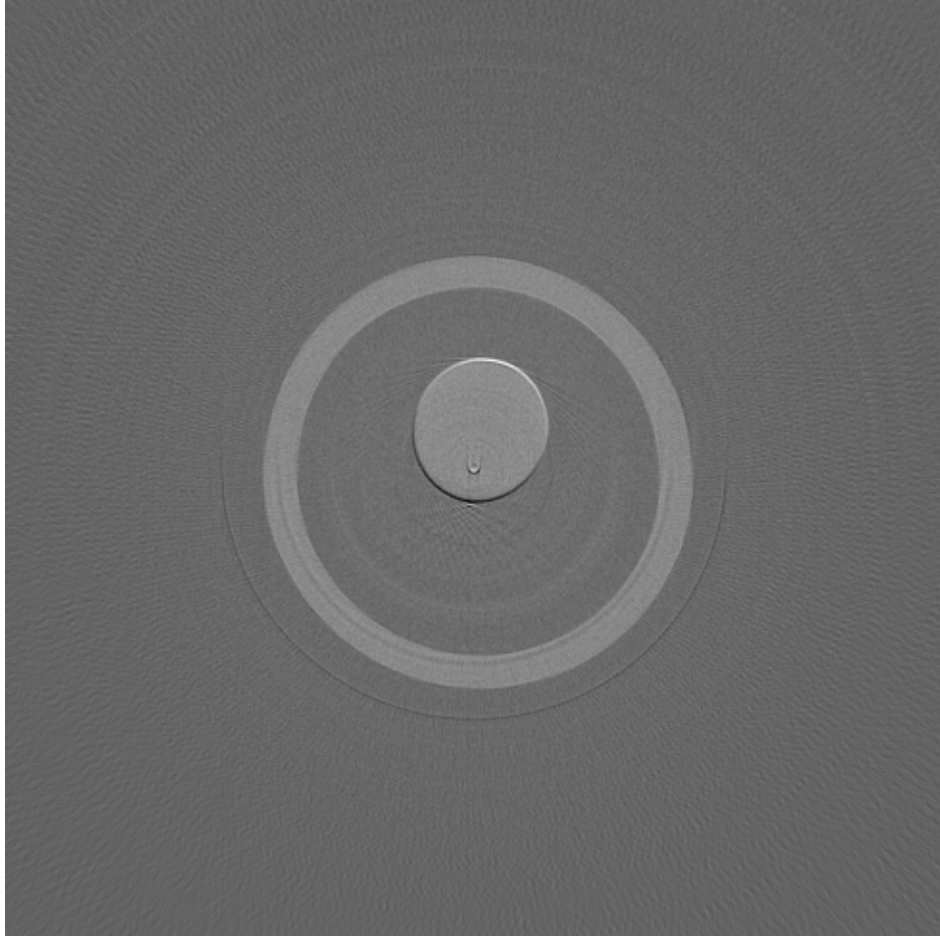


Fig.1.26 The apparent absorption image of the phantom B using option 1

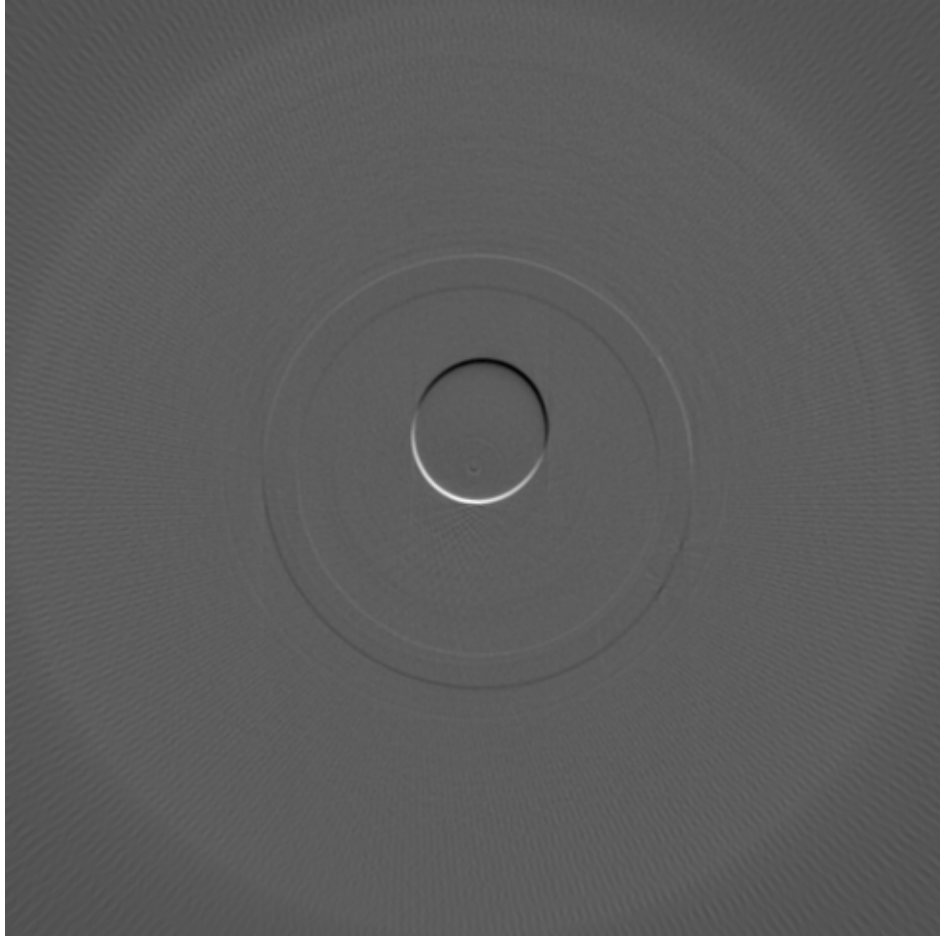


Fig.R.1.27 The refraction image of the Lucite B using option 1

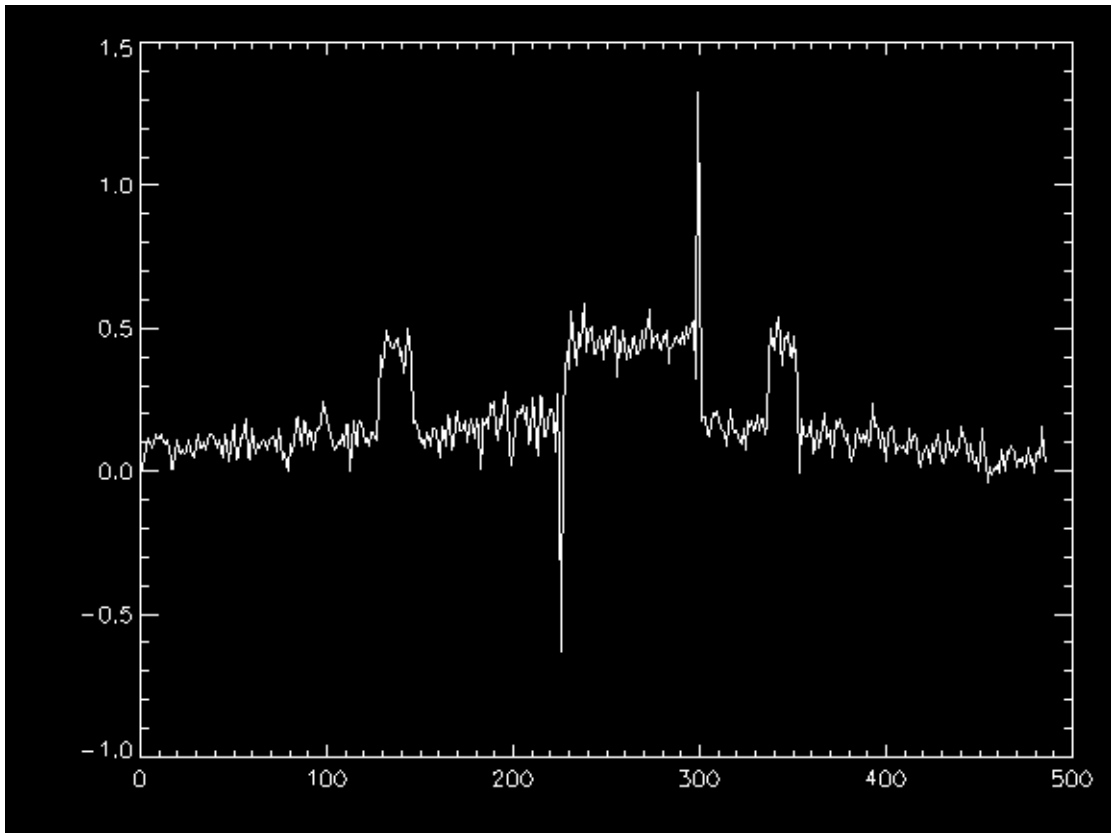


Fig. R.1.28 A line profile of absorption image of the phantom B using option 1

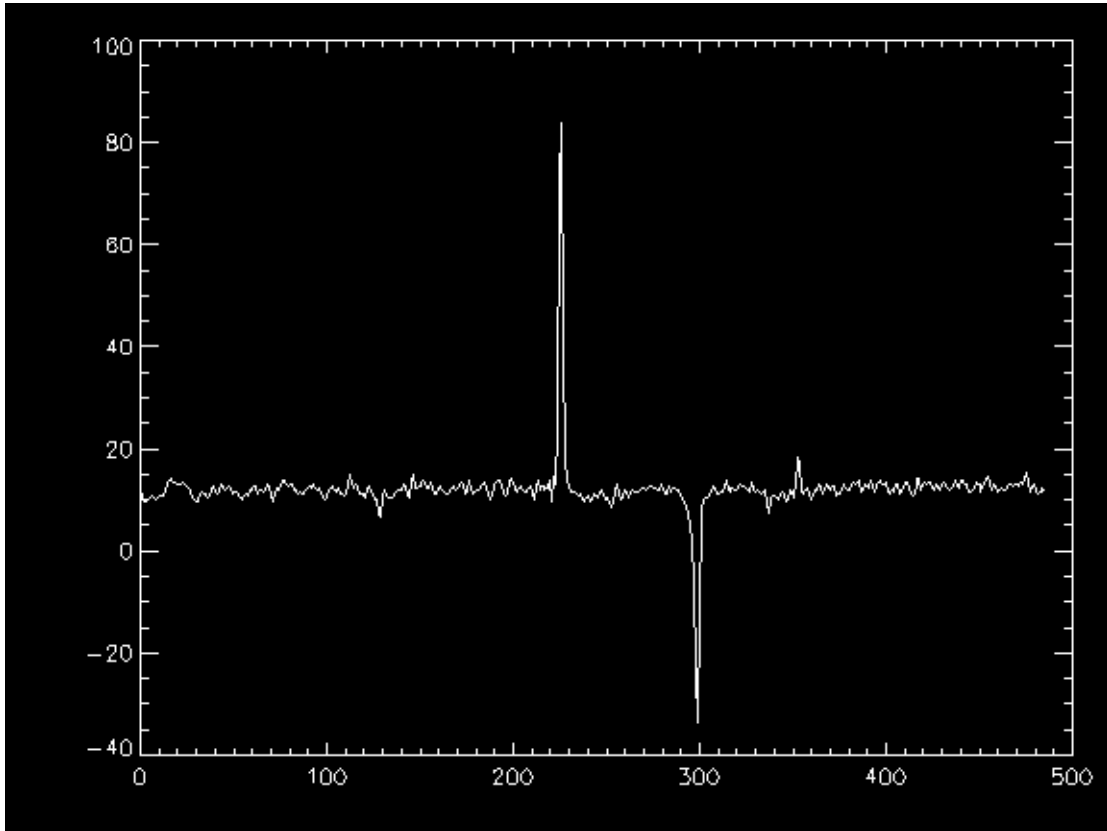


Fig. R.1.29 A line profile of refraction image of the phantom B using option 1

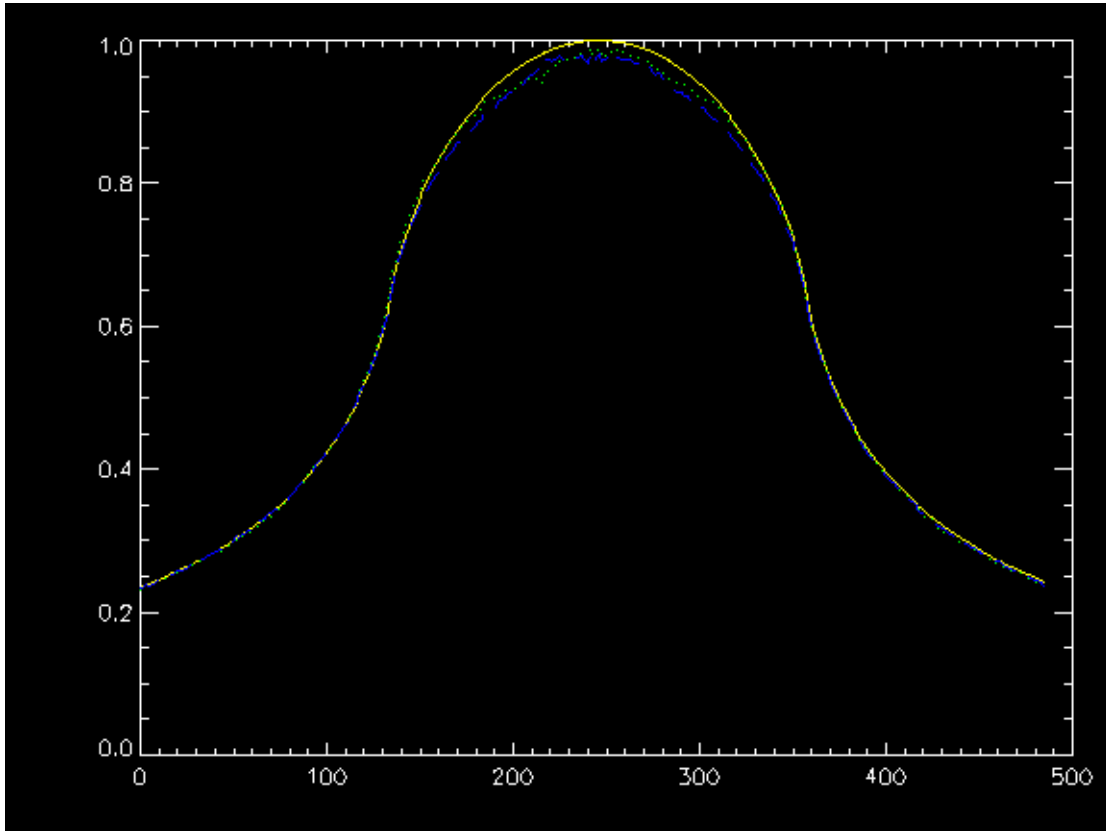


Fig. R.1.30 The comparison of line profiles Higher, Lower and simulation images of phantom B filled with water without any digital filters. Where, yellow, blue and green lines represent simulation, Higher and Lower image profile

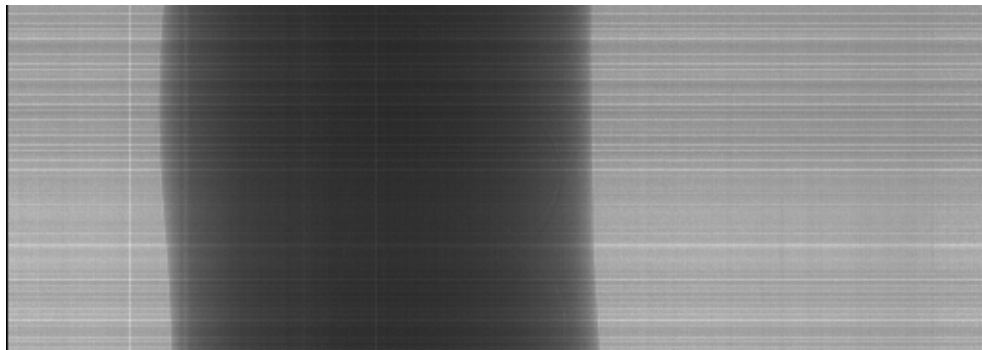


Figure R.2.1 Absorption raw tomography data of phantom B filled with water

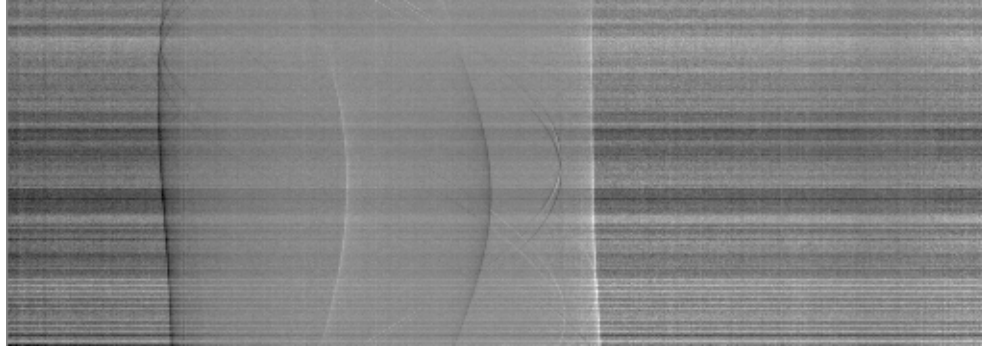


Figure R.2.2 Refraction raw tomography data of phantom B filled with water

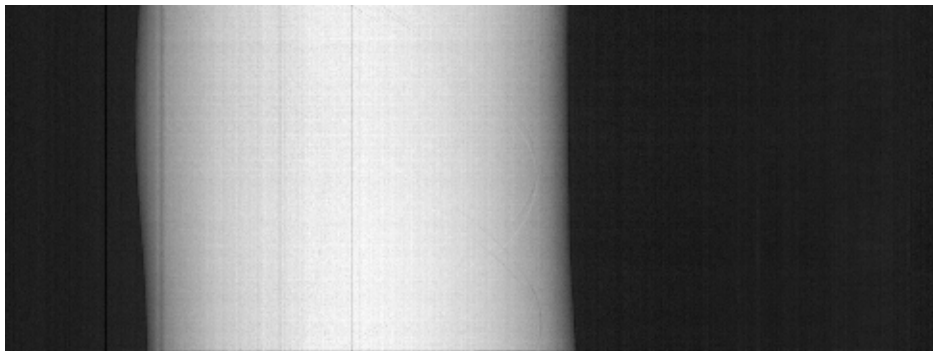


Fig. R.2.3 Absorption sinogram of phantom B filled with water

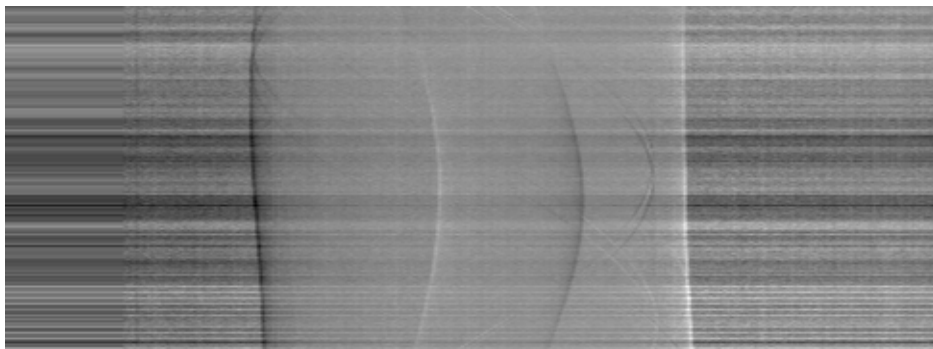


Fig. R.2.4 Refraction sinogram of phantom B filled with water

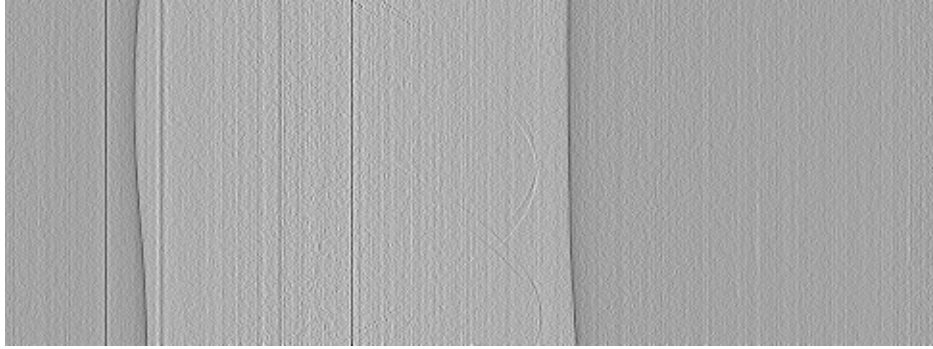


Fig. R.2.5 Filtered absorption sinogram of phantom B filled with water

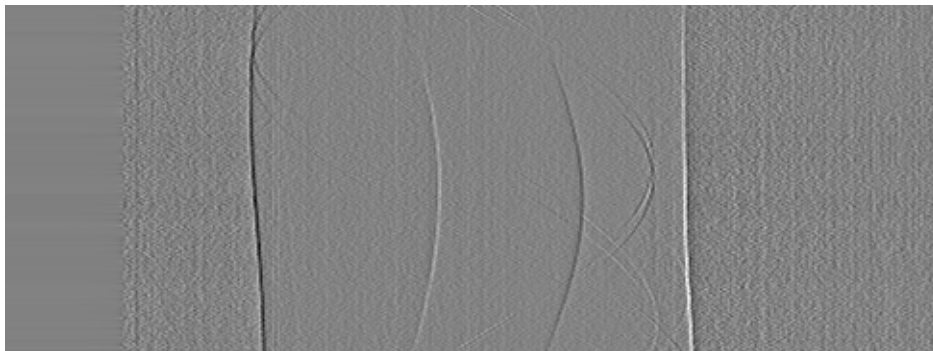


Fig. R.2.6 Filtered refraction sinogram of phantom B filled with water

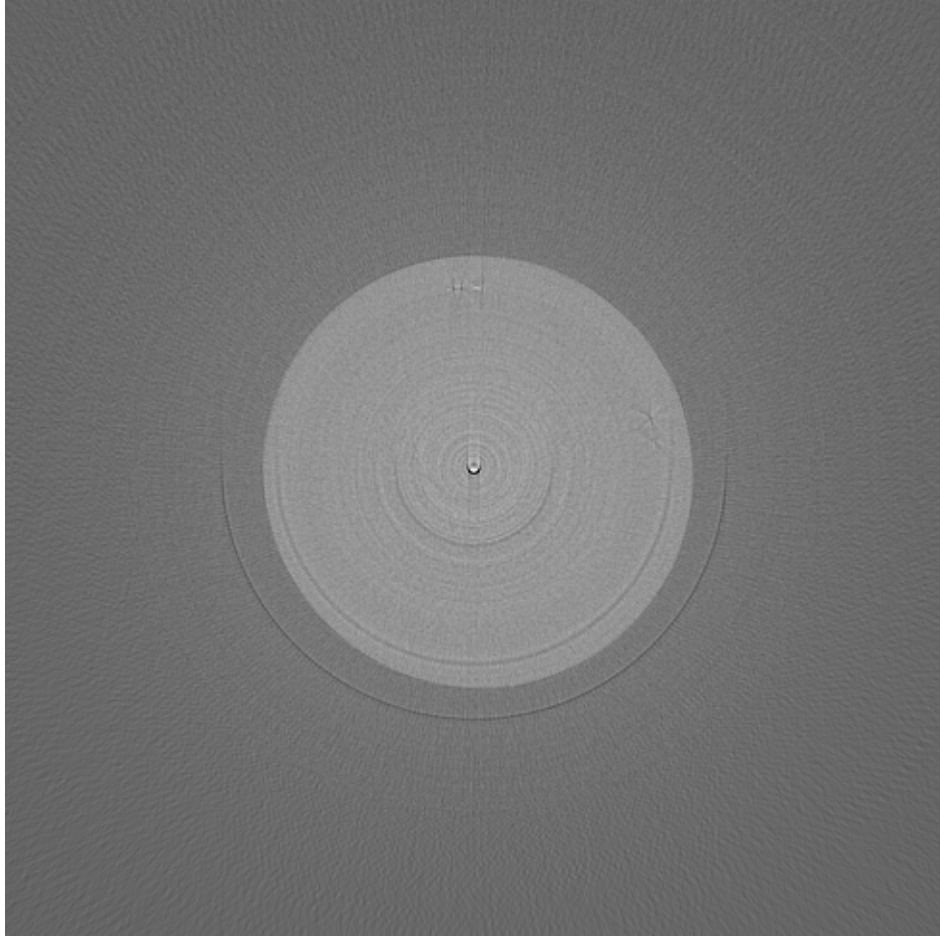


Fig. R.2.7 Reconstructed absorption image of phantom B filled with water

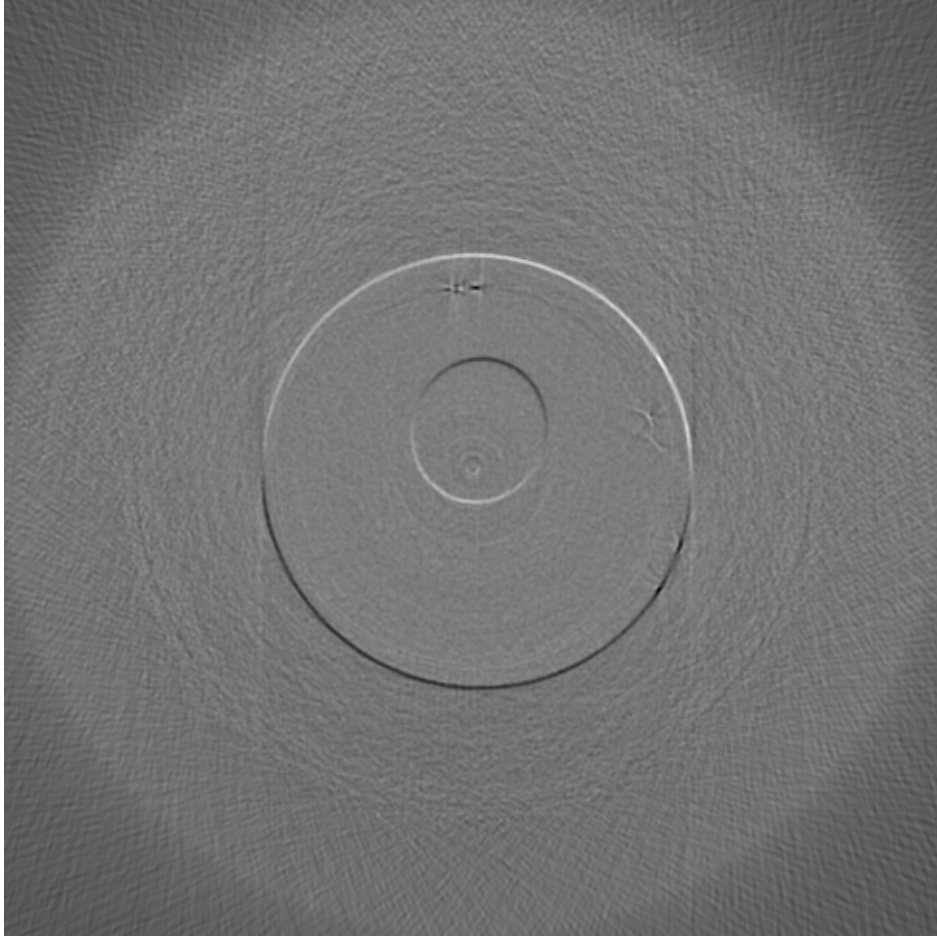


Fig. R.2.8 Reconstructed refraction image of phantom B filled with water

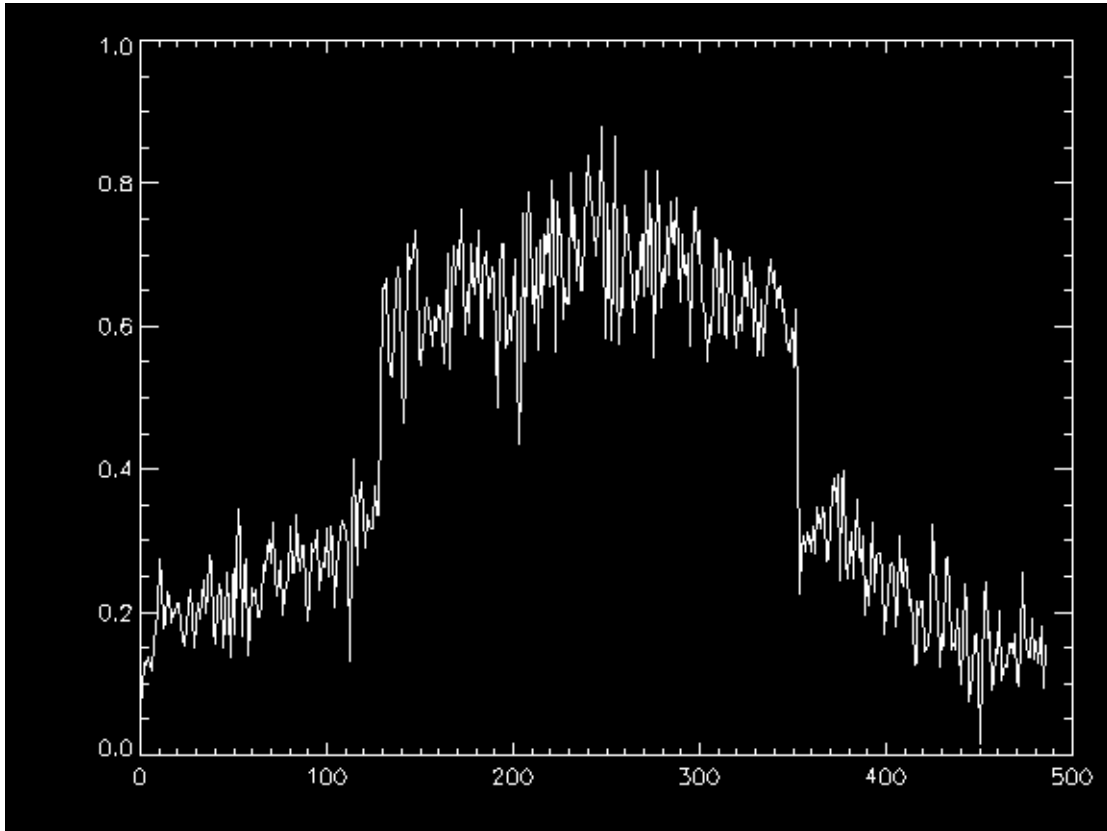


Fig. R.2.9 A line profile of reconstructed absorption image of phantom B filled with water

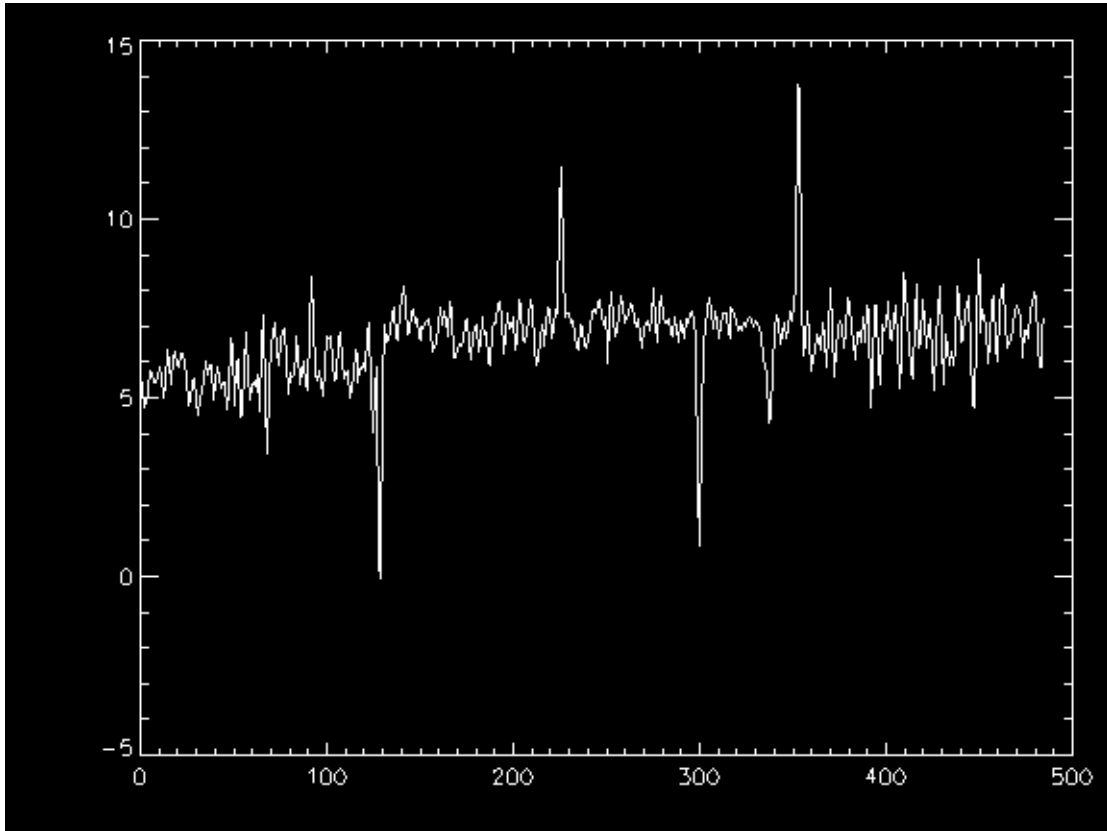


Fig. R.2.10 A line profile of reconstructed refraction image of phantom B filled with water

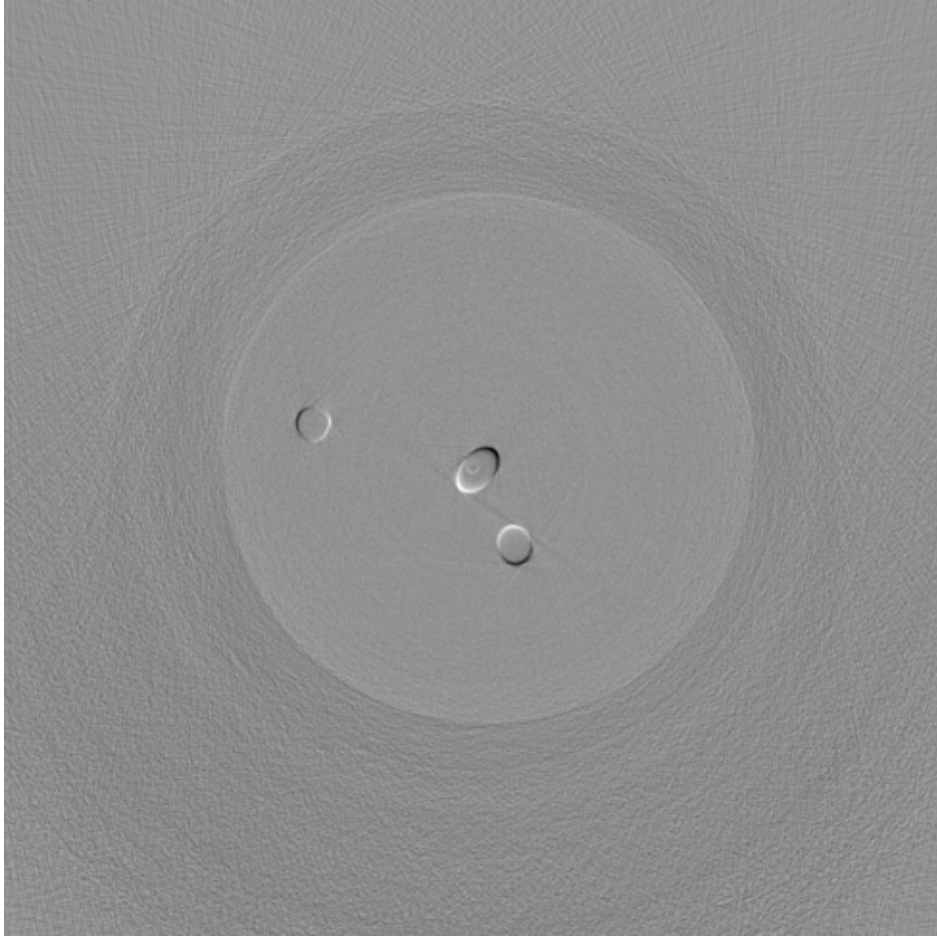


Fig. R.3.1 The refraction image $z=0$ x-y plane

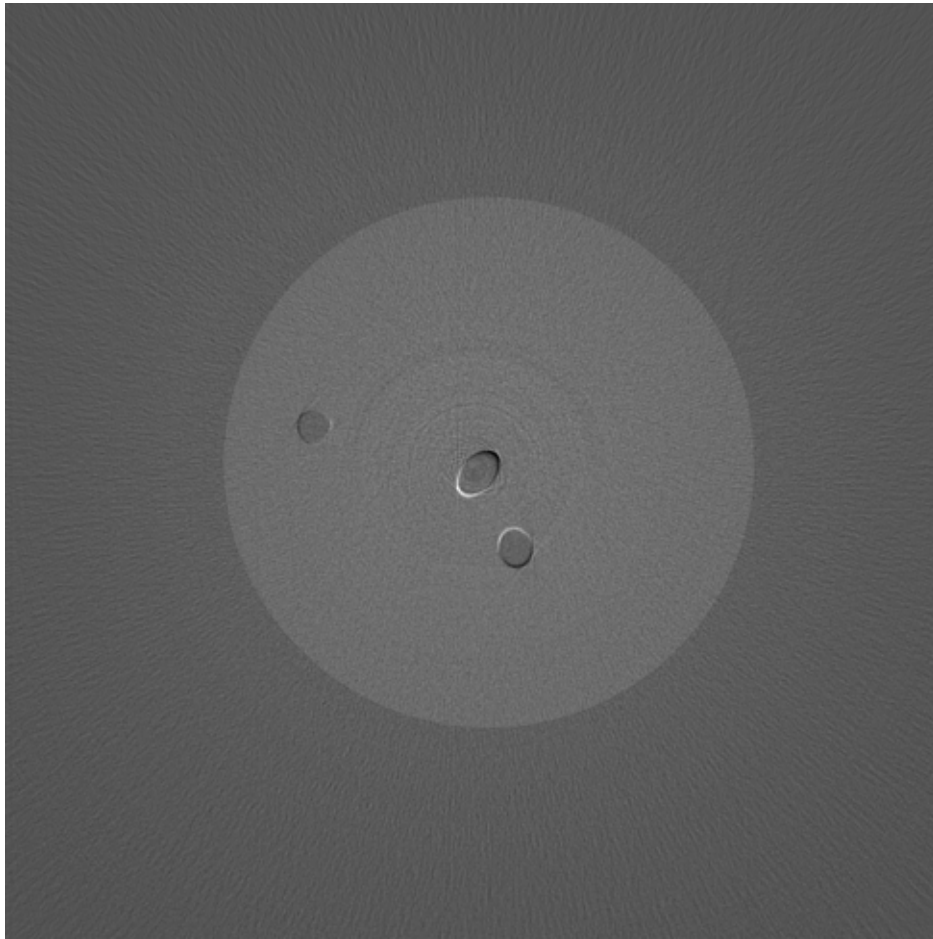
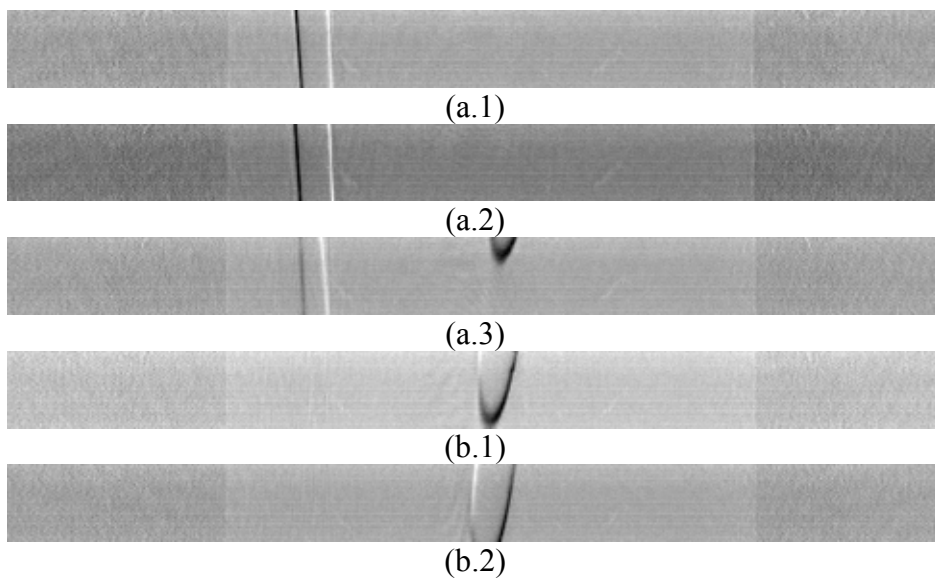


Fig. R.3.2 The apparent absorption image of $z=0$ slice in the radial(x-y) plane



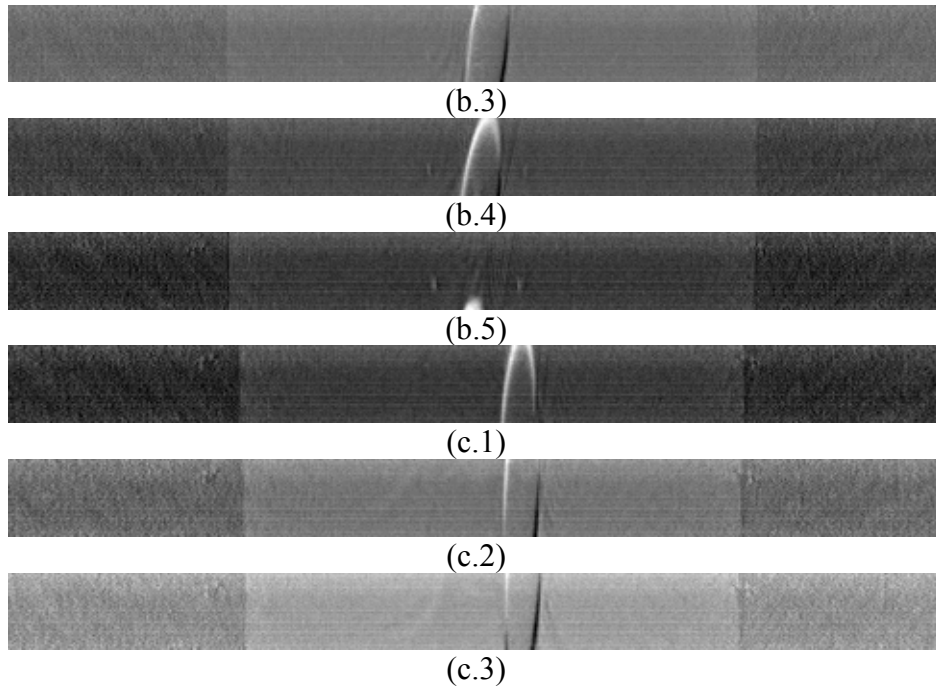
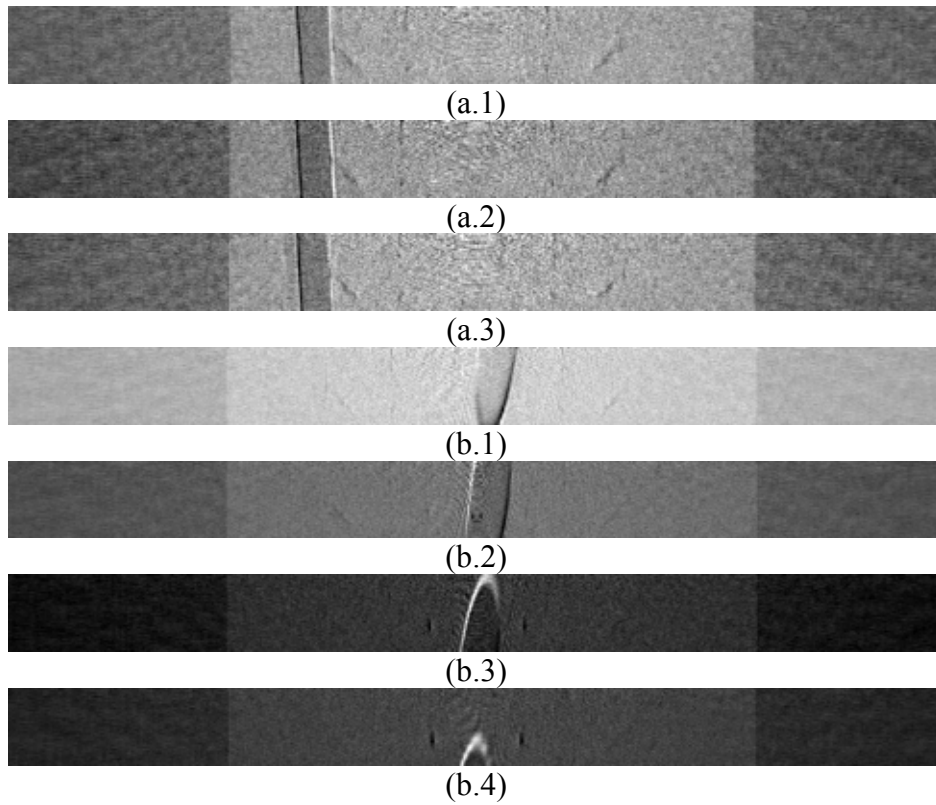


Fig R.3.3 Transversal slices of the refraction image; where (a),(b) and (c) are images of from the channel 1,2, and 3 respectively



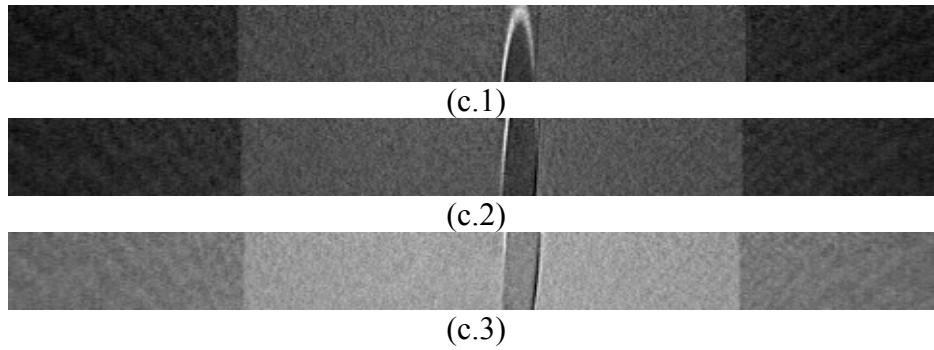


Fig R.3.4 Transversal slices of the apparent absorption image; where (a),(b) and (c) are images of from the channel 1,2, and 3 respectively. The lower number means higher y position.

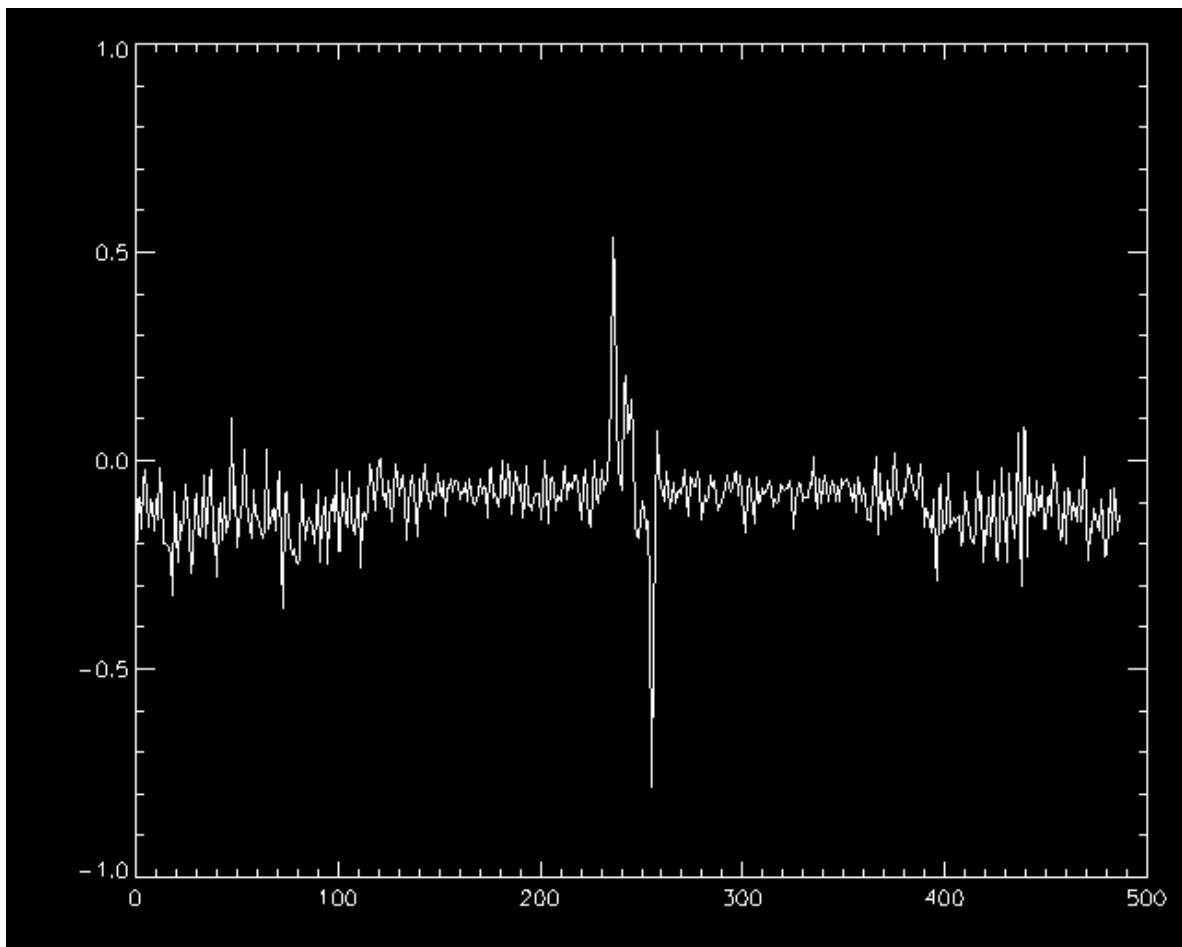


Fig R.3.5 The line profile of the refraction image at $y=241, z=0$ showing the refraction signal from channel 2

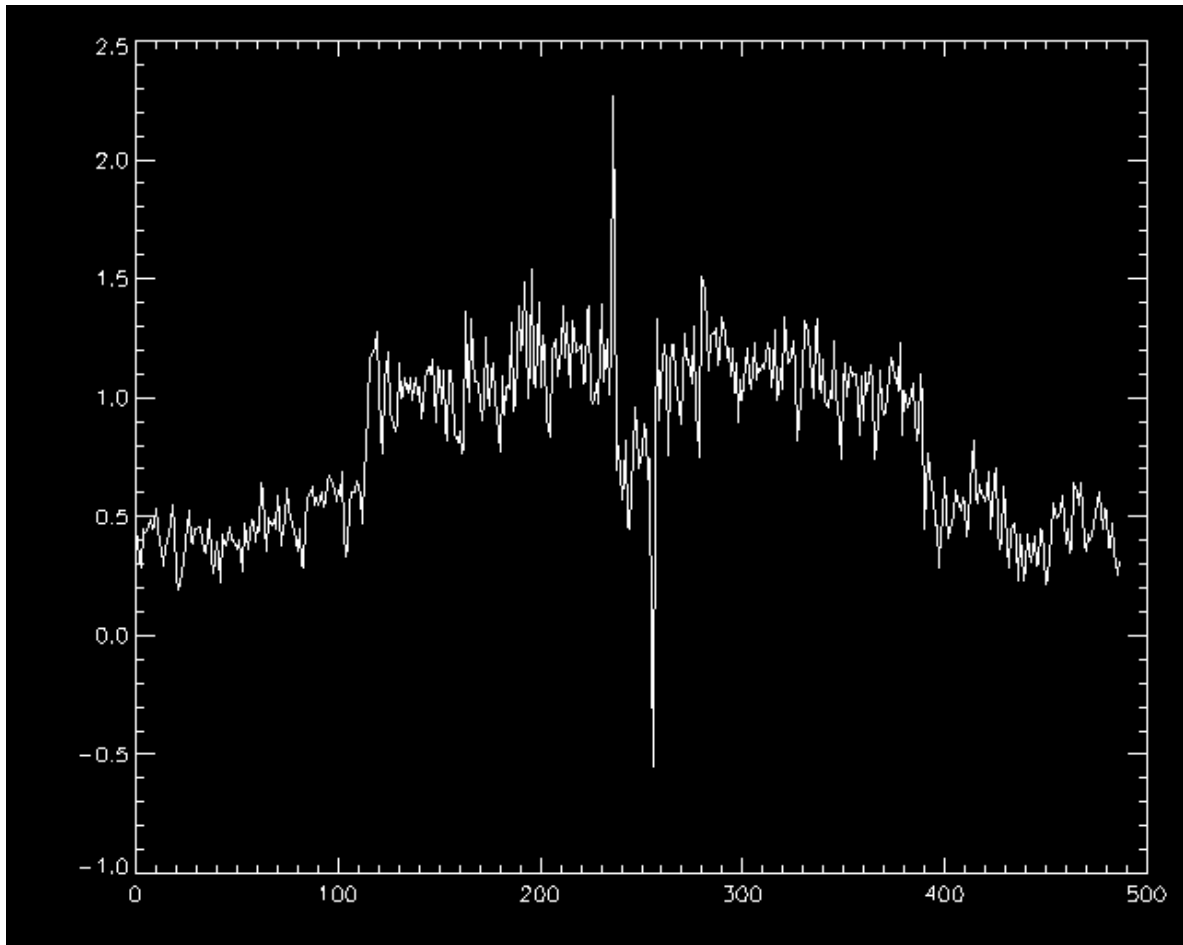


Fig R.3.6 The line profile of the absorption image at $y=246$, $z=1$ showing the absorption signal from channel 2

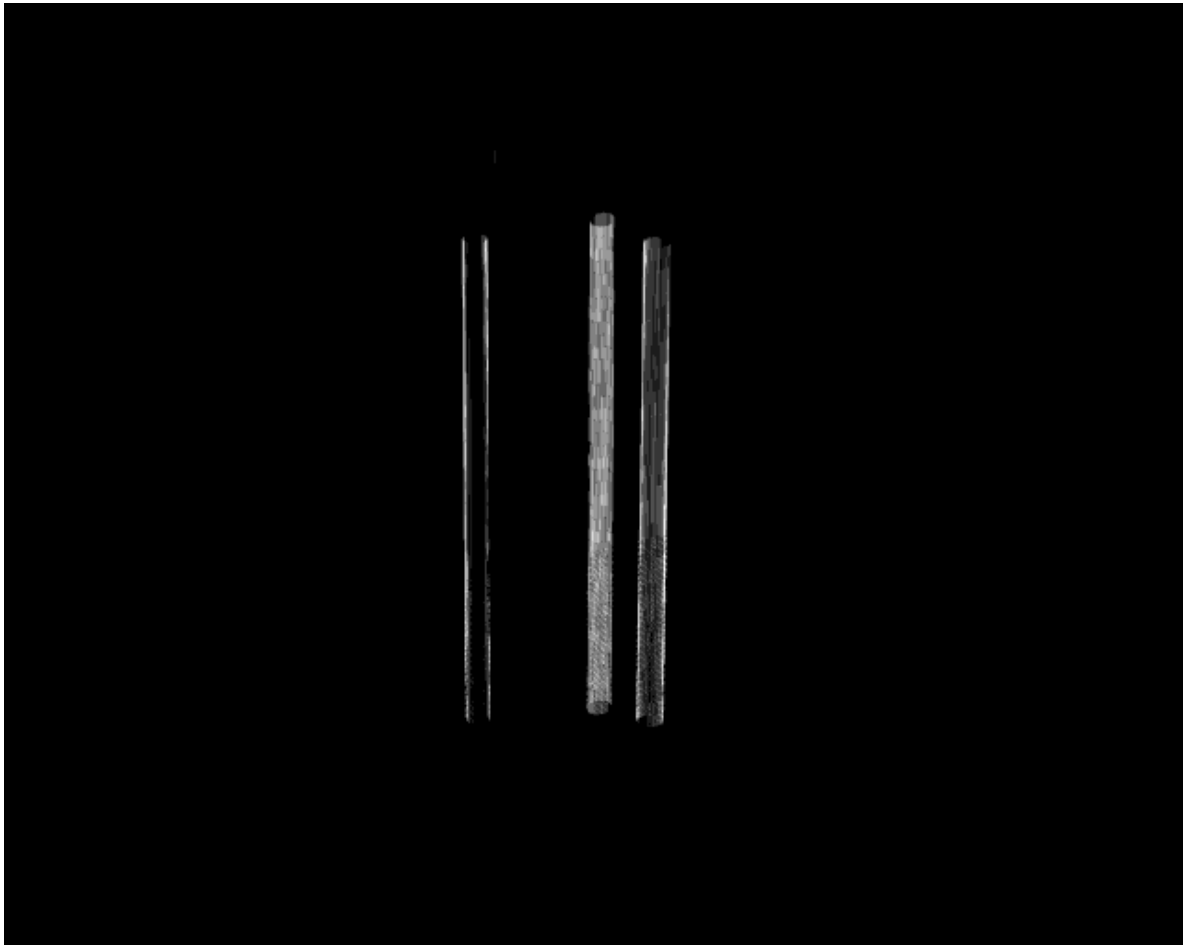


Fig R.3.7 The three-dimensional voxel projection of refraction image

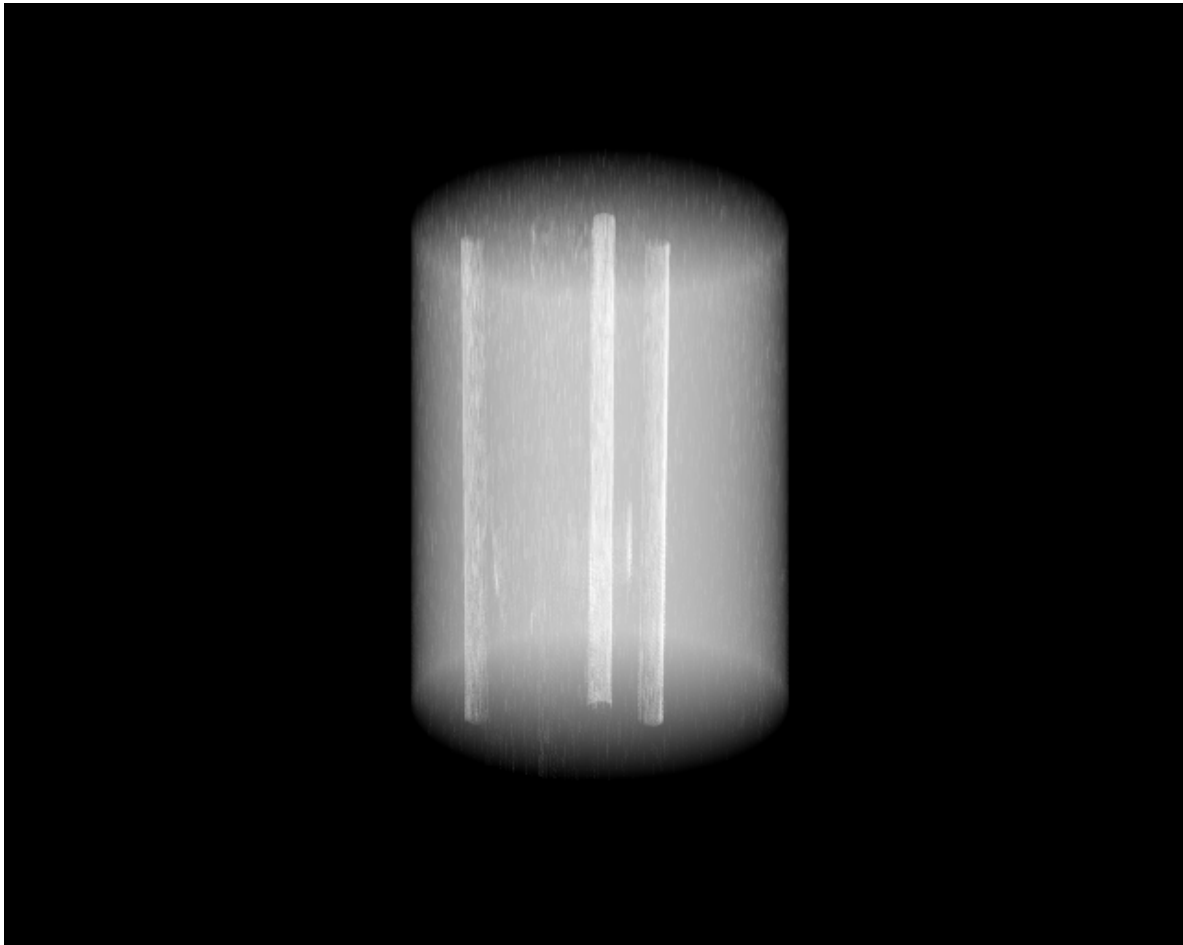


Fig 3.8 The three-dimensional voxel projection of absorption image